# THE JOURNAL OF ACOUSTICAL SOCIETY OF INDIA

ACOUSTICAL SOCIETY OF INDIA
1971
॥ नादाधी नमतोजयत् ॥

# The Journal of Acoustical Society of India

## The Refereed Journal of the Acoustical Society of India (JASI)

**The Journal of Acoustical Society of India** is a refereed journal of the Acoustical Society of India **(ASI)**. The **ASI** is a non-profit national society founded in 31st July, 1971. The primary objective of the society is to advance the science of acoustics by creating an organization that is responsive to the needs of scientists and engineers concerned with acoustics problems all around the world.

Manuscripts of articles, technical notes and letter to the editor should be submitted to the Chief Editor. Copies of articles on specific topics listed above should also be submitted to the respective Associate Scientific Editor. Manuscripts are refereed by at least two referees and are reviewed by Publication Committee (all editors) before acceptance. On acceptance, revised articles with the text and figures scanned as separate files on a diskette should be submitted to the Editor by express mail. Manuscripts of articles must be prepared in strict accordance with the author instructions.

All information concerning subscription, new books, journals, conferences, etc. should be submitted to Chief Editor:

*B. Chakraborty, CSIR - National Institute of Oceanography, Dona Paula, Goa-403 004,*
*Tel: +91.832.2450.318, Fax: +91.832.2450.602, e-mail: bishwajit@nio.org*

Annual subscription price including mail postage is Rs. 2500/= for institutions, companies and libraries and Rs. 2500/= for individuals who are not **ASI** members. The Journal of Acoustical Society of India will be sent to **ASI** members free of any extra charge. Requests for specimen copies and claims for missing issues as well as address changes should be sent to the Editorial Office:

*ASI Secretariat, C/o Acoustics and Vibration Metrology, CSIR-National Physical Laboratory, Dr. KS Krishnan Road, New Delhi 110 012, Tel: +91.11.4560.8317, Fax: +91.11.4560.9310, e-mail: asisecretariat.india@gmail.com*

# The Journal of Acoustical Society of India

A quarterly publication of the Acoustical Society of India

## Volume 48, Number 3, July 2021

| ARTICLES |
| --- |

**INFORMATION**

| | |
| --- | --- |
| **Information for Authors** | Inside back cover |

# FOREWORD

**Guest Editorial for JASI special issue**

In this special edition of JASI, we present a range of articles on sound and structure interaction. Being a fundamental topic, it has relevance to all aspects of life: science, art and engineering. Accordingly, there are six articles, one on the theory of sound and structure interaction, two covering musical acoustics and three on the effects of materials on sound propagation.

In the first article, that is a numerical study, Jaykumar Bhalodia and Abhijit Sarkar examine the fully coupled interaction of an infinite 1-D plate with an acoustic half space. The authors use a clever strategy to replace the analytical model of an infinite beam with that of a finite beam having suitable boundary conditions. This work opens up possibilities of conducting several more fundamental studies.

The next two articles focus on the acoustics of two Indian percussion instruments. The first is by Sooraj G. and Chandramouli Padmanabhan who present a detailed and meticulously made set of experiments on the mridangam, a south Indian drum. This drum is an invariable accompaniment in Karnatic music. Their objective is to understand the coupling between the cavity and the membrane. The second article by Ankit, Saptarshi, Vishal and Anurag presents a study of the acoustics of another south Indian drum. Known as the Mizhāvu, it is a primary accompaniment in the Sanskrit theatre forms of Kerala. Sounds from the Mizhāvu were recorded and the spectrum was subsequently used for modeling. Both the studies construct detailed FEM models to match the data and understand the acoustic signatures. It is encouraging to see such studies happening at Indian universities. India is an ancient culture, where many traditions are passed down without the written word from the teacher to the student. These scientific studies will help preserve the rich traditions.

Finally, the last three articles examine materials and their effect on sound. Investigations on special materials (metamaterials or bio-inspired materials) or designs that affect absorption or transmission of sound in very specific ways are on the rise in the scientific world. In this context, Sripriya Ramamoorthy and Shanker Krishnan study porous materials with a dual purpose of sound and thermal insulation. This has definite applications to the automobile and the building construction industry. The article has a very detailed literature survey and is comprehensive in examining the parameters influencing the dual objective. Following this, authors Hase, Mirza, Akiwate and Venkatesham present an experimental technique for conducting modal analysis of light and delicate structures such as straws. Non-contacting excitation and measuring systems are used. This could be useful in the future metamaterial designs for acoustics. Lastly, authors Mishra, Parida and Panigrahi present a detailed optimization study for acoustic lining of underwater vehicles. A conflict of objectives exists where echo should be low for stealth and transmission should be low for comfort and communication. The authors conduct a parametric study to achieve the objective over a wide frequency range.

Let me conclude this editorial by expressing my gratitude to Dr. Bishwajit Chakraborty for inviting me to put together this special issue. I am thankful to all the authors for their erudite and timely contributions. I also acknowledge the reviewers for their valuable suggestions. And finally, many thanks to my co-editor Prof. Abhijit Sarkar for conducting the entire process so smoothly.

**Prof. Venkata Sonti**
Guest Editor - JASI
Mechanical Engineering,
Indian Institute of Science, Bangalore

**Prof. Abhijit Sarkar**
Guest Co-Editor - JASI
Mechanical Engineering,
Indian Institute of Technology, Madras

# Coupled structural acoustics of a semi-infinite plate submerged in an infinite acoustic half space: Analytical & FEM solutions

**Jaykumar A. Bhalodia[1] and Abhijit Sarkar[2]**
*Department of Mechanical Engineering*
*Indian Institute of Technology Madras, Chennai-600 036*
*e-mail: asarkar@iitm.ac.in*

## ABSTRACT

In this work, we review the analytical solutions presented by Crighton [1, 2] on the structural response of a semi-infinite plate submerged in an acoustic half-space and excited by a line harmonic forcing. Despite its mathematical rigour, Crighton did not present any validation of the derived results using numerical or experimental methods. In this article, we propose a novel simulation methodology in a commercial FEM package (ANSYS) to simulate the same problem. Using beam elements mounted on appropriately tuned linear and torsional dampers the effect of infinite structural domain is simulated. The infinite acoustic half space is modeled using the inbuilt acoustic infinite elements in ANSYS. The results obtained using these two methods are shown to correlate well.

## 1. INTRODUCTION

Structural acoustics studies incorporate the effect of ambient acoustic pressure on the dynamics of the structure. The ambient acoustic fluid exerts an acoustic loading on the vibrating structure due to which the structural response gets modified from the *in vacuo* response. The structural response in turn modifies the acoustic field, thus constituting a two way coupled problem. The area of structural acoustics is of major importance in naval applications involving underwater structures.

Structural acoustics is a classical field of study. Different approaches have been adopted for the study of structural acoustic problems. These include numerical, experimental and analytical approaches. Numerical techniques are mainly based on Finite Element Method (FEM), Boundary Element Method (BEM), FE-BE Method. Experimental investigation includes structural velocity/acceleration measurement and acoustic pressure/intensity measurement. Despite its importance, there have been very few analytical studies reported in the literature. In this regard, the works of Crighton[1, 2] deserve a special mention. Employing the rigorous approach of complex analysis, he was able to present approximate analytical solutions for the structural acoustics of a fluid-loaded semi-infinite plate under the action of different harmonic loading conditions. The analytical approach of his works brought out illuminating insights

---

[1]*Presently at Lam Research, Bangalore India;* [2]*Corresponding Author: asarkar@iitm.ac.in*

regarding the nature of fluid-loading. For example, Crighton rigorously established conditions for light, moderate and significant fluid loading on the structure.

Unfortunately, the rigorous and sophisticated analytical treatment of Crighton's work has remained largely inaccessible for most practicing engineers. In fact, most results presented by Crighton are in the form of analytical formulae and deep physical insights associated with the derived formulae. He has very rarely presented his results in a graphical form which appeals to practicing engineers. Further, a major critique of his works has been that despite the correctness of his mathematical treatment, he has not presented any validation of his derived results.

The objective of this work is to present a validation of the analytical results presented by Crighton. Towards this end, an FEM-based simulation using a commercial package (ANSYS) is proposed. Although in-built acoustic infinite elements are available in ANSYS for simulating the infinite acoustic half space, the modeling of the infinite structural domain through FEM is challenging. A novel concept of using tuned linear and torsional dampers to emulate the anechoic condition in the structure is proposed. The results obtained using the analytical method are compared with the results obtained using FEM simulation.

## 2. *IN VACUO* STRUCTURAL ANALYSIS

We consider an infinite plate in the *x-z* plane excited by a uniform line harmonic force (along the *z*-direction) applied at *x* = 0 (refer Figure 1). Due to the above line harmonic loading along the *z*-direction, none of the physical quantities have any variation along the *z* direction *viz.* $\frac{\partial}{\partial z} = 0$. All harmonic quantities are denoted by a complex exponential of the form $e^{-i\omega t}$. In consonance with[2], we refer to this structure as the semi-infinite plate structure. Incorporating the condition $\frac{\partial}{\partial z} = 0$, the governing equations for the harmonic response of the plate excited by a line force is given by

$$\frac{E_p h^3}{12(1-v^2)} \frac{d^4 \eta_{F_o}(x)}{dx^4} - \rho_p h \omega^2 \eta_{F_o}(x) = F_o \delta(x)$$

(1)



(a) 3D view                    (b) 2D view
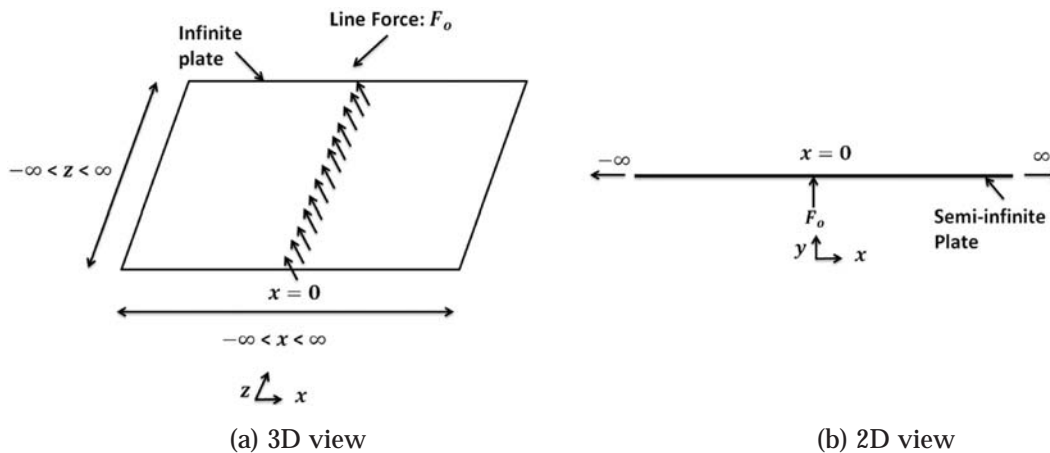
**Fig. 1.** Schematic illustration of an *in vacuo* semi-infinite plate under harmonic line force excitation.

Here, $E_p$ is the Young's modulus for the plate, $v$ is the Poisson's ratio, $h$ is the plate thickness, $\rho_p$ is the density of the plate material, $\omega$ is the angular frequency and $\eta_{F_o}(x)$ is the flexural displacement of the plate. The applied line harmonic force is given by $F_o \delta(x)$ where $F_o$ is the magnitude of applied force and $\delta(x)$ is the delta function centred at *x*=0. Note, $\frac{E_p h^3}{12(1-v^2)}$ is the flexural rigidity of a plate and $m = \rho_p h$ is the mass per unit area of the plate.

### 2.1 *Analytical Solution*

The solution of the above equations is available in the literature[4, 5]. Here, we present the results for completeness. In order to solve the above equation, a Fourier transformation from the spatial domain *(x)* to wave number domain *(k_x)* is applied. The forward and inverse wave number transforms of a function *f(x)* are given as

$$F(k_x) = \int_{-\infty}^{\infty} f(x)\, e^{-ik_x x}\, dx, \quad f(x) = \frac{1}{2\pi} \int_{-\infty}^{\infty} F(k_x)\, e^{ik_x x}\, dk_x \tag{2}$$

Using the properties of wave number transform pair, equations (1) is simplified as follows:

$$(k_x^4 - k_p^4)\eta_{F_o}(k_x) = \frac{F_o}{D} \tag{3}$$

In the above, $k_p = (m\omega^2/D)^{1/4}$ is the *in vacuo* flexural wave number. For obtaining the spatial domain response, inverse Fourier transform is applied on the above equation to give

$$\eta_{F_o}(x) = \frac{F_o}{2\pi D} \int_{-\infty}^{\infty} \frac{e^{ik_x x}}{k_x^4 - k_p^4}\, dk_x \tag{4}$$

Evaluation of the above improper integrals can be accomplished using complex analysis. We demonstrate this approach for $x > 0$ using the semi-circular contour as illustrated in Figure 2a. The poles of the integrand function occur at $k_x = \pm k_p, \pm i k_p$. The residues at these poles are given as

$$\text{Residue}\left(f(k_x)\right) = \begin{cases} \dfrac{ie^{ik_p x}}{4k_p^3} & \text{for the simple pole at } k_x = k_p, \\[2ex] \dfrac{-ie^{-ik_p x}}{4k_p^3} & \text{for the simple pole at } k_x = -k_p, \\[2ex] \dfrac{-e^{-k_p x}}{4\kappa_p^3} & \text{for the simple pole at } k_x = ik_p, \\[2ex] \dfrac{e^{k_p x}}{4k_p^3} & \text{for the simple pole at } k_x = ik_p, \end{cases} \tag{5}$$
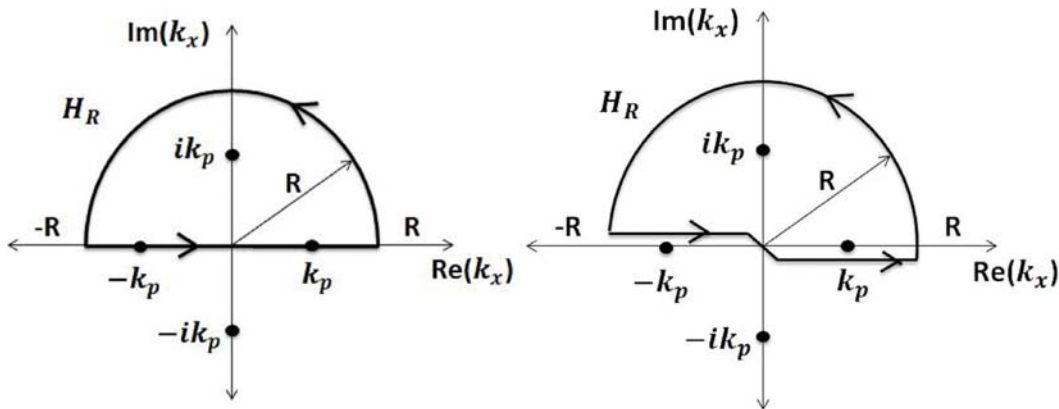


**Fig. 2.** (a) Closed semi-circular contour $C_0$ with interior pole at $ik_p$ and the poles $\pm k_p$ on the contour. Note, R→∞. (b) Modified contour $C_0$ for $x > 0$: poles $k_p$ and $ik_p$ lie interior to the contour.

In Figure 2a, the location of the poles in the complex $k_x$ plane is shown by dots. It is evident that the pole at $ik_p$ lies inside the contour whereas the pole at $-ik_p$ lies outside the contour. The poles on the real

axis $\pm k_p$ lie on the contour. Recall, the Cauchy integral theorem does not specify whether the residue contribution of the poles on the contour need to be accounted for. Thus, at this stage physical reasoning is invoked to resolve this ambiguity.

Note, that the residue corresponding to $k_x = k_p$ leads to a forward travelling wave (recall we use $e^{-i\omega t}$ convention). Similarly, a backward travelling wave is induced due to the residue corresponding to $k_x = -k_p$. Due to causality, we understand that for the present line loading at $x = 0$, only a forward travelling wave is expected in the region $x > 0$. A backward travelling wave in the region $x > 0$ is physically implausible. Thus, in the application of the Cauchy integral theorem, we need to account for the residue corresponding to the pole at $k_x = k_p$ but ignore the residue contribution corresponding to the pole at $k_x = -k_p$. Alternatively, we may implement the Cauchy integral theorem by perturbing the contour slightly in the form shown in Figure 2b. As illustrated in the figure, the pole at $k_p$ lies interior to the perturbed contour but the pole at $-k_p$ falls outside the perturbed contour. Cauchy integral theorem may thus be applied over this modified contour taking residue contributions of all poles lying interior to this modified contour.

Thus, using Cauchy residue theorem and Jordan's Lemma $\eta_{F_o}(x)$ is calculated as follows for $x > 0$

$$\eta_{F_o}(x) = \frac{F_o}{4Dk_p^3}\left[ ie^{ik_p x} - e^{-k_p x} \right] \tag{6}$$

The non-dimensional form of the above equation is formulated as

$$\dot{\eta}_{F_o}^*(\chi) = \frac{\eta_{F_o}(x)D}{F_o L^3} = \frac{1}{4(\kappa_p)^3}\left[ ie^{i\kappa_p \chi} - e^{-\kappa_p \chi} \right] \tag{7}$$

In the above equation, non-dimensional group of parameters are: $\kappa_p = k_p h$ and $\chi = x/h$ represents the non-dimensional *in vacuo* structural wave number and non-dimensional spatial variable, respectively. Further, $\kappa_p$ can be interpreted as the non-dimensional frequency. $\eta_{F_o}^*(\chi)$ is the non-dimensional deflection. For $x < 0$, similar formula for the non-dimensional deflection can be derived.

## 2.2 *Equivalent FEM model*

The governing equation of an Euler-Bernoulli beam under a point harmonic force $F_o$ acting at $x=0$ is given as[4]

$$E_b I_b \frac{d^4 \eta_{F_o}(x)}{dx^4} - \rho_b A \omega^2 \eta_{F_o}(x) = F_o \delta(x) \tag{8}$$

Here, $E_b$ is the Young's modulus, $I_b = \frac{bh_b^3}{12}$ is the area moment of inertia, $\rho_b$ is the material density, A is the cross-sectional area of the beam.

The above equation is similar in nature to equation (1), both being fourth order linear ordinary
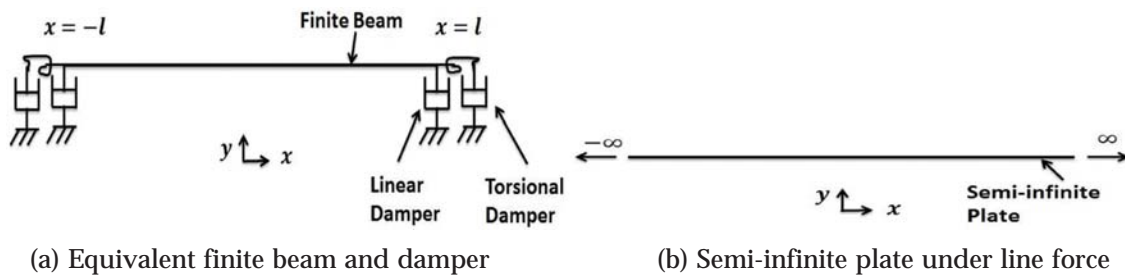


(a) Equivalent finite beam and damper      (b) Semi-infinite plate under line force

**Fig. 3.** Finite beam mounted on appropriately tuned linear and torsional dampers is equivalent to a semi-infinite plate.

differential equations. The constant terms in the equations though, have different physical meaning. Thus, the terms $\dfrac{E_p h^3}{12(1-v^2)}$ and $\rho_p h$ in the semi-infinite plate equation is analogous to the terms $E_b I_b$ and $\rho_b A$ in the beam equation, respectively. Thus, a beam with $E_b = \dfrac{E_p}{1-v^2}$ and $b = 1$ is equivalent to a semi-infinite plate.

The objective of the present study is to formulate an analogy between the finite beam response and the semi-infinite plate response. The analogy is clear from the similarity of the governing differential equations for these two cases as presented above. However, the semi-infinite plate considered in equation (1) is of infinite extent (*viz.* $\in (-\infty, \infty)$). To complete the analogy, we need to derive the appropriate boundary conditions on the finite length beam such that the response of the beam within the finite span $x \in (-l, l)$ is equivalent to the response of the semi-infinite plate within the region $x \in (-l, l)$. Note, an incident wave along $x$ for a semi-infinite plate does not lead to any reflected waves. Similar anechoic conditions in the equivalent finite length beam is achieved by mounting it on appropriately tuned linear and torsional dampers at its ends (refer Figure 3a).

Next, we proceed to evaluate the appropriate damping co-efficient of the linear and torsional dampers. As illustrated in Figure 4, consider a semi-infinite beam $x \in (-\infty, 0)$ having a free end at $x = 0$. A forward travelling incident wave in the beam is given by: $\eta_i(x) = A e^{ikx}$. A reflected wave is induced due to boundary conditions at $x = 0$. The reflected wave is given by: $\eta_r(x) = B e^{-ikx} + C e^{kx}$. The total response as a superimposition of the incident wave and the reflected waves is given by $\eta_t(x) = \eta_i(x) + \eta_r(x)$.

Linear and torsional dampers are placed at $x = 0$. The damping coefficients for the linear and torsional dampers are given by $c_l$ and $c_t$, respectively. Reaction force from the linear damper is $V_l = -i c_l \omega \eta_t(x)$ and the reaction moment from the torsional damper is $M_t = -i\omega c_t \dfrac{d\eta_t(x)}{dx}$. The shear force at any section of beam is given by $E_b I_b \dfrac{d^3 \eta_t}{dx^3}$ and the bending moment is given by $E_b I_b \dfrac{d^2 \eta_t}{dx^2}$. The force balance and moment balance at $x = 0$, is given by
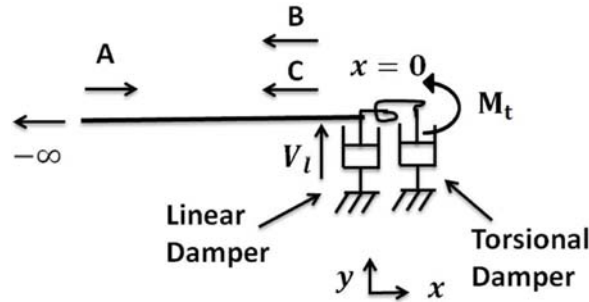


**Fig. 4.** Schematic illustration of flexural waves in semi-infinite beam (equivalent to beam mounted on tuned linear and torsional dampers). The reaction loads due to dampers are illustrated in the figure.

$$E_b I_b \left.\frac{d^3 \eta_t(x)}{dx^3}\right|_{x=0} = \left. V_l \right|_{x=0} \tag{9a}$$

$$-E_b I_b \left.\frac{d^2 \eta_t(x)}{dx^2}\right|_{x=0} = \left. M_t \right|_{x=0} \tag{9b}$$

The above equations are solved for $B$ and $C$ in terms of $E_b I_b$, $k$, $c_l$, $c_t$, $\omega$, $A$. For brevity, the functional form of the solutions are not presented here. For the subsequent discussions we assume $B = B(E_b, I_b, k, c_l, c_t, \omega, A)$ and $C \equiv C(E_b, I_b, k, c_l, c_t, \omega, A)$. As discussed earlier, for formulating the analogy we need to impose the non-reflecting condition which implies $B = C = 0$. Thus, we have

$$B(E_bI_b, k, c_l, c_t, \omega, A) = 0, C(E_bI_b, k, c_l, c_t, \omega, A) = 0 \tag{10}$$

Equation (10) is solved using the symbolic computation package in (Matlab). Using the above two relations, the damping coefficients $c_l$ and $c_t$ are obtained as

$$c_l = \frac{E_bI_bk^3}{\omega}, \quad c_t = \frac{E_bI_bk}{\omega} \tag{11}$$

Thus, a semi-infinite beam terminated by a linear and a torsional damper with damping coefficients as given by the above relation emulates the anechoic condition at the support location (refer Figure 3). These tuned dampers at both the ends act as anechoic termination points on either side. In this configuration, the finite beam does not have any reflecting wave from its ends $x = \pm l$. This resembles the condition of the semi-infinite plate. The displacement of the finite beam mounted on the above dampers at its ends is simulated using Finite Element Method (FEM) (refer Figure 3a). The FEM simulation is implemented using the commercial package ANSYS 16.0.

In ANSYS, we model a finite beam of length $2l$, and dampers are attached to its free ends ($x = \pm l$). In ANSYS, BEAM3 or BEAM23 element can be used with zero shear correction factor to model a beam element[9]. Using a zero shear correction factor effectively reduces the Timoshenko beam element to the Euler-Bernoulli beam element. Dampers are modelled with the COMBIN14 element in ANSYS[9]. Damping coefficients are calculated from equation (11). Harmonic excitation is applied at the mid-point of the beam structure ($x = 0$) and the response of the finite beam is obtained. As dictated by the equivalence condition discussed earlier, the width of the beam is chosen to be unity and the Young's modulus of the beam material is taken as $E_b = \dfrac{E_p}{1-v^2}$.

### 2.3 *Results and Discussion*

The non dimensional frequency response function (FRF) is evaluated at the excitation point using the analytical solution (refer equation (7)) and the ANSYS simulation. The result for the drive point FRF is shown in Figure 5. Such FRF results are insightful in presenting an equivalent lumped system model between the input excitation and the output response. The deformation at all points in the structure at non-dimensional frequency $k_p = 20.458$ is presented in Figure 6. As is evident from these results, the response calculated using the analytical solution procedure and the FEM simulation are in close agreement.
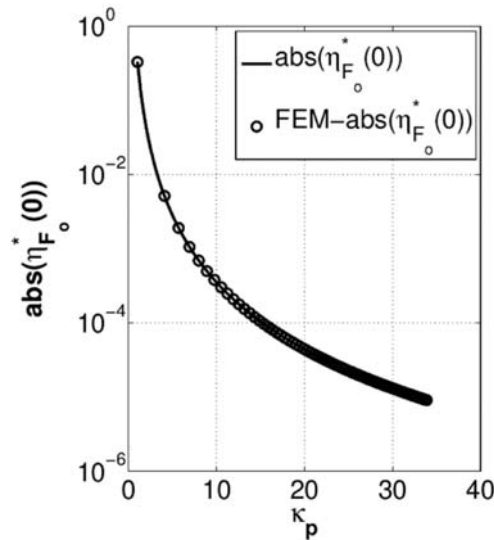


**Fig. 5.** Drive point FRF of a semi-infinite plate
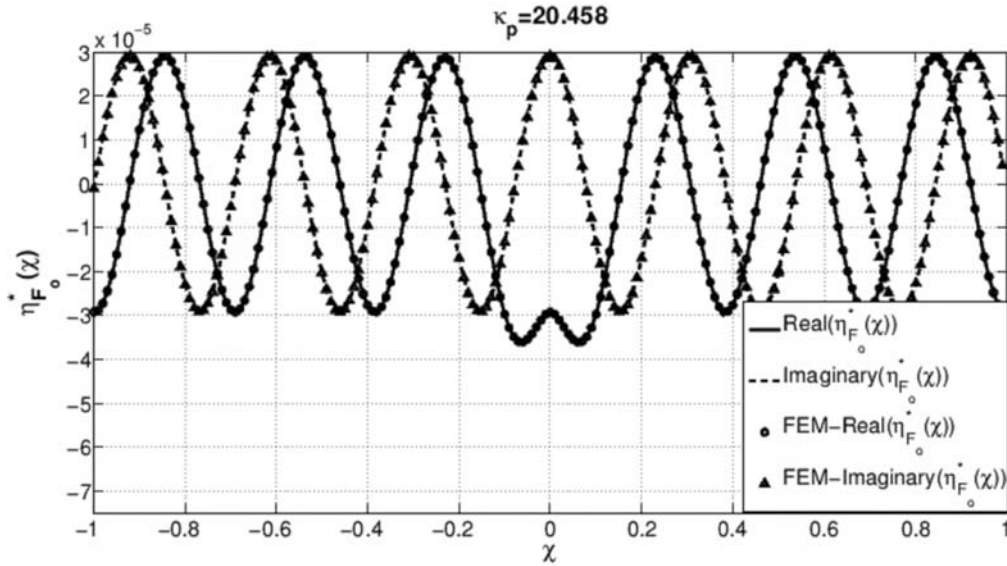
**Fig. 6.** *In vacuo* response of the semi-infinite plate

## 3. COUPLED STRUCTURAL ACOUSTICS

In this section, the *in vacuo* structural dynamics is generalized by considering an infinite acoustic half space on one side of the plate structure (refer Figure 7). Such a model is referred to as the fluid-loaded plate model. Both analytical formulation and the FEM solution procedure is discussed for this model.
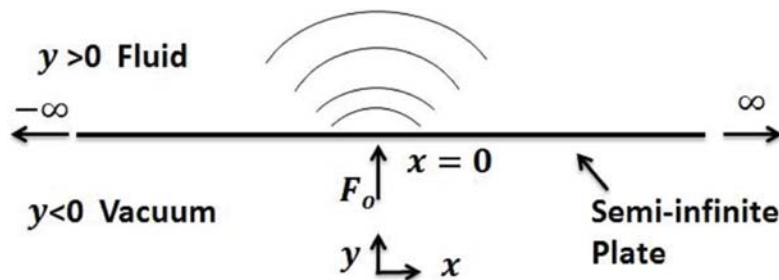


**Fig. 7.** Schematic illustration of fluid-loaded infinite plate subjected to a harmonic line forcing.

### 3.1 *Formulation*

As in the previous section, we consider an infinite plate in the $x - z$ plane. Harmonic line forcing is applied at $x = 0$ along the $z$-direction. In the region $y > 0$, an acoustic fluid of density $\rho_f$ is present while the region $y < 0$ is vacuum (refer Figure 7). The effect of acoustic fluid was neglected in the in vacuo analyses discussed in the previous section. Due to the acoustic loading on the plate, its response is not the same as the in vacuo response. Likewise, the coupled structural response changes the acoustic pressure distribution in comparison to an uncoupled acoustic pressure distribution. Crighton[1] studied the coupled response of a semi-infinite plate under harmonic line force excitation. In this section, we present these derivations for completeness.

The coupled structural acoustic equations for line harmonic force is given as[1]

$$\frac{Eh^3}{12(1-v^2)} \frac{d^4\eta_{F_o}(x)}{dx^4} - \rho_p h\omega^2 \eta(x) = F_o\delta(x) - p(x,0) \tag{12}$$

In above equation, acoustic pressure on the plate is given by $p(x, 0) = i\,\omega\,\rho_f\phi\,(x, 0)$, where $\phi\,(x, y)$ is the acoustic potential and $\rho_f$ is the fluid density. Helmholtz equation for acoustic fluid is given as[2]

$$\nabla^2\phi(x, y) + k_o^2\phi(x, y) = 0 \tag{13}$$

Velocity of the acoustic fluid along $y$ is given by $v_a(x, y) = \dfrac{\partial\phi}{\partial y}$ and the acoustic wavenumber is given by $k_o = \omega/c_f$ ($c_f$ is the sound speed in the acoustic medium). At the fluid structure interface, the structural velocity, $v_p(x) = -i\omega\eta_{F_0}(x)$ is equal to the acoustic velocity, $v_a(x, 0)$. Imposing this continuity condition at the interface, we get the following equation

$$v_p(x) = v_a(x, 0) \Rightarrow -i\omega\eta_{F_0}(x) = \frac{\partial\phi(x, 0)}{\partial y} \tag{14}$$

Applying spatial Fourier transform on equation (13) we get,

$$(-ik_x)^2\phi(k_x, y) + \frac{\partial^2\phi(k_x, y)}{\partial y^2} + k_o^2\phi(k_x, y) = 0$$

$$\Rightarrow \frac{\partial^2\phi(k_x, y)}{\partial y^2} - \gamma^2\phi(k_x, y) = 0 \text{ where, } \gamma^2 = k_x^2 - k_0^2$$

The solution of the above equation is given by $\phi(k_x, y) = Ae^{-\gamma y} + Be^{\gamma y}$, where $A$ and $B$ are undetermined constants.

Note, in the acoustic domain $y > 0$. Dictated by the requirements of physical plausibility, the valid solution of the Helmholtz equation is $\phi\,(k_x, y) = \phi\,(k_x, 0)\,e^{-\gamma y}$, where $\gamma$ is given as

$$\gamma = \begin{cases} \sqrt{k_x^2 - k_o^2} & \text{for } |k_x| > k_o \text{ and } k_x \text{ is real} \\ -i\sqrt{k_o^2 - k_x^2} & \text{for } |k_x| > k_o \text{ and } k_x \text{ is real} \end{cases} \tag{15}$$

Similarly, applying a spatial to a wavenumber domain transformation on equation (14) and substituting the relation $\phi\,(k_x, y) = \phi\,(k_x, 0)\,e^{-\gamma y}$ in it, we get the following equation

$$-i\omega\eta_{F_0}(k_x) = -\gamma\phi(k_x, 0) \Rightarrow \phi(k_x, 0) = \frac{i\omega\eta_{F_0}(k_x)}{\gamma} \tag{16}$$

Taking the wave number transform of equation (12) and using the above simplifications we get

$$\left((-ik_x)^4 - k_p^4\right)\eta_{F_0}(k_x) = \frac{F_o}{D} + \frac{\omega^2\rho_f\eta_{F_0}(k_x)}{D\gamma} \Rightarrow \eta_{F_0}(k_x) = \frac{F_o}{D\left[\left(k_x^4 - k_p^4\right) - \dfrac{\mu k_p^4}{\gamma}\right]} \text{ where } \mu = \frac{\rho_f}{\rho_p h} \tag{17}$$

In the above equation, $k_p = (m\omega^2/D)^{1/4}$ represents the *in vacuo* flexural wave number. Finally, $\eta_{F_0}(x)$ is obtained by taking the inverse Fourier transform of the above equation.

$$\eta_{F_0}(x) = \frac{F_o}{2\pi D}\int_{-\infty}^{\infty}\frac{e^{ik_x x}}{\left[(k_x^4 - k_p^4) - \dfrac{\mu k_p^4}{\gamma}\right]}dk_x \tag{18}$$

### 3.2 *Coupled Dispersion Equation*

The denominator of the integrand in the above equation equated to zero is referred to as the coupled dispersion equation. The coupled dispersion equation is given by

$$(k_x^4 - k_p^4)\gamma - \mu k_p^4 = 0 \tag{19}$$

Roots of this equation are called the coupled wavenumbers for the semi-infinite fluid-loaded plate. This dispersion equation and its roots are studied extensively in the literature. Dispersion equation in the non dimensional form is given as follows[2].

$$\left(\xi^4 - 1\right)\left(\xi^2 - M^2\right)^{1/2} - \frac{\epsilon}{M} = 0 \tag{20}$$

Here, $\xi = k_x/k_p$, $M = k_o/k_p = c_p/c_o$, and $\epsilon = \dfrac{\rho_f}{\rho_p c_f}\sqrt{\dfrac{E}{12\rho_p(1-v^2)}}$. $\epsilon$ is called the intrinsic fluid loading parameter which is independent of frequency and depends only on material properties of the fluid and the structural medium. $M$ is called the Mach number as it is the ratio of wave speed in the plate to the sound speed in fluid. At $M=1$, the uncoupled structural and the fluid wavenumber become identical. The corresponding frequency is called the critical or coincidence frequency $\omega_g = \sqrt{\dfrac{mc_f^4}{D}}$.

To evaluate the roots of equation (19), a fifth order polynomial in $\gamma$ is obtained from the dispersion equation[3, 6]. This equation is given as

$$\gamma^5 + 2k_o^2\gamma^3 + \left((k_o^4 - k_p^4)\gamma - \mu k_p^4\right) = 0 \tag{21}$$

In equation (21), each root of $\gamma$ gives two roots of $k_x = \pm\sqrt{\gamma^2 - k_0^2}$. Thus, we get 10 roots. Detailed discussion regarding acceptability of these roots are given in[3] and[6]. Crighton[7] gave asymptotic approximations for these roots.

Two root configurations corresponding to (a) frequency less than the coincidence frequency and (b) frequency greater than the coincidence frequency are shown in Figures 8 and 10, respectively. For the case (a), the roots are having following nature: One +$ve$ real root ($\gamma_1$), two -$ve$ real roots ($\gamma_4$ and $\gamma_5$) and a pair of complex conjugate roots ($\gamma_2$ and $\gamma_3$) (refer Figure 8). Conjugate roots lie in the first ($\gamma_2$) and fourth ($\gamma_3$) quadrant of the $\gamma$ plane. As argued by Crighton[3] and Strawderman[6], the negative real roots are not acceptable for the residue contribution for $x > 0$. Among the conjugate roots, only $\gamma_2$ is acceptable. Corresponding to the roots in the $\gamma$-plane shown in Figure 8, the $k_x$-plane roots are shown in Figure 9. In this figure, the roots $k_1$ and $k_2$ are obtained from the root $\gamma_1$, and the roots $k_3$ and $k_4$ are obtained from the
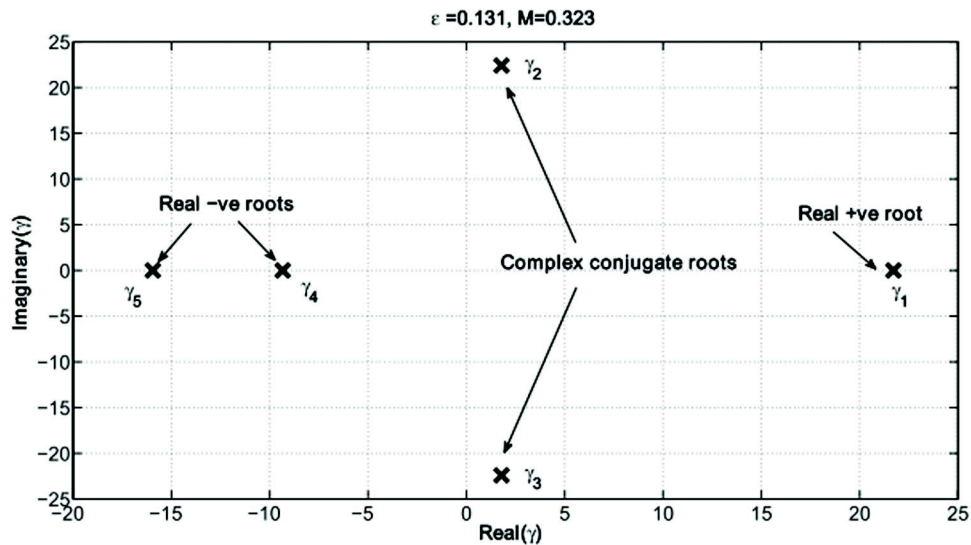


**Fig. 8.** $\gamma$-plane: Roots for $\epsilon$ = 0.131 and M = 0.323
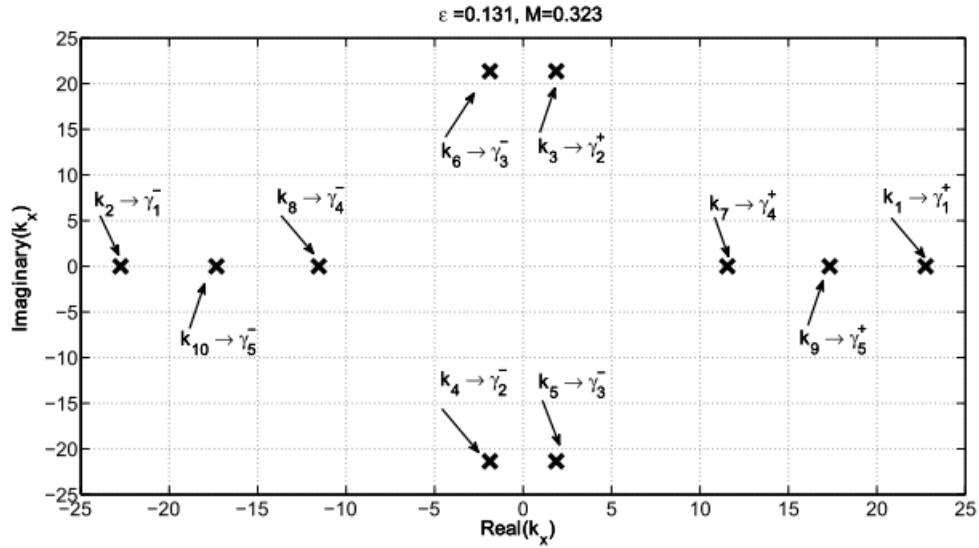
**Fig. 9.** $k_x$-plane: Roots for $\epsilon$ = 0.131 and M = 0.323

root $\gamma_2$. Thus, the acceptable roots for the residue contribution are $k_1$, $k_3$ (for *x*>0) and $k_2$, $k_4$ (for *x*<0) as shown in Figure 9.

Root configuration (b) is observed above the coincidence frequency which is shown in Figure 10. In this configuration, nature of the roots is as follows: One +*ve* real root ($\gamma_1$), two pairs of complex conjugate roots ($\gamma_2$, $\gamma_3$, $\gamma$ and $\gamma_4$, $\gamma_5$). $\gamma_2$ lies in first quadrant whereas $\gamma_3$ lies in the fourth quadrant. Likewise, $\gamma_4$ lies in the second quadrant while $\gamma_5$ lies in the third quadrant of the $\gamma$-plane (refer Figure 10). As argued by Crighton[3] and Strawderman[6], among the above roots the acceptable roots are $\gamma_1$ $\gamma_2$, and $\gamma_5$. The corresponding roots on the $k_x$-plane are shown in Figure 11. In this figure, the acceptable roots are $k_1$, $k_3$, $k_9$ (for *x*>0) and $k_2$, $k_4$, $k_{10}$ (for *x*<0). Roots $k_9$ and $k_{10}$ are called leaky waves and its contribution in the residue is accounted only if $|k_o| > |k_{leaky}|$ (refer[3] and [8]).
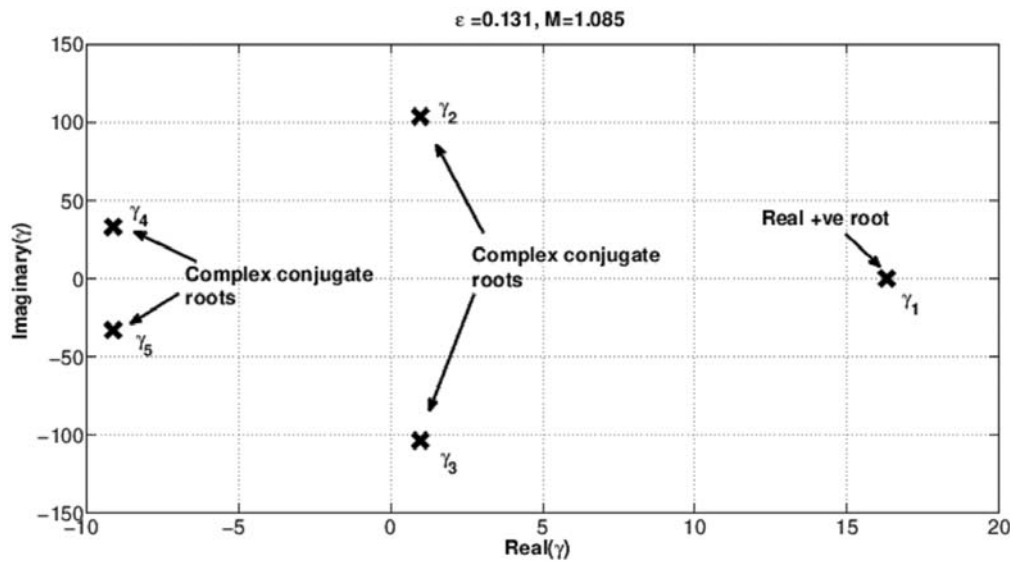


**Fig. 10.** $k_x$-plane: Roots for $\epsilon$ = 0.131 and M = 1.085
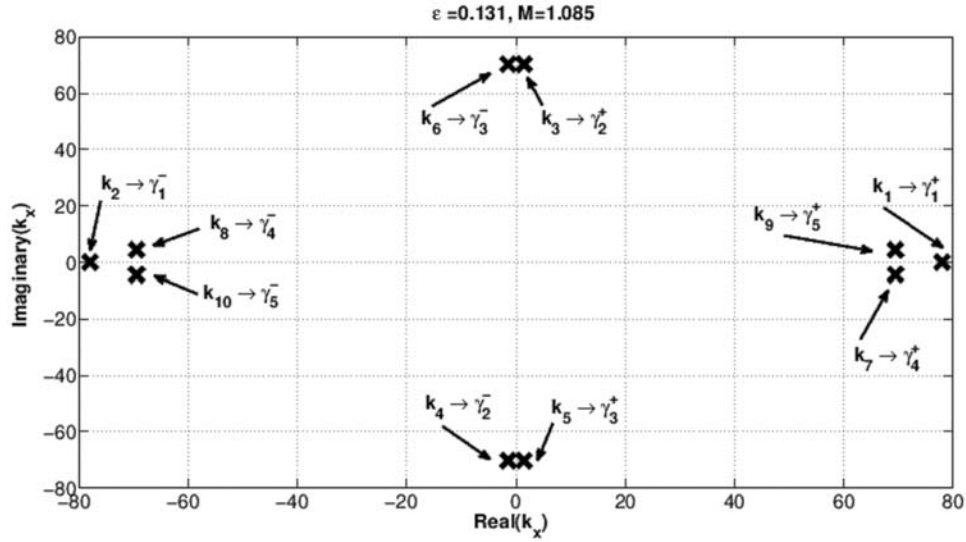
**Fig. 11.** $k_x$-plane: Roots for $\in$ = 0.131 and M = 1.085

### 3.3 *Contour Integration*

The integral in equation (18), is evaluated using contour integration. For $x>0$, Figures 12 and 13 illustrates the contours for frequencies below and above coincidence, respectively. In Figure 12, the contour encloses the poles $k_1$, $k_3$ and $k_6$. Among these three poles, only the poles $k_1$ and $k_3$ are valid. In Figure 13, the contour encloses poles $k_1$, $k_3$, $k_6$, $k_8$ and $k_9$. Among these five poles, only the poles $k_1$, $k_3$ and $k_9$ are valid for $x>0$.
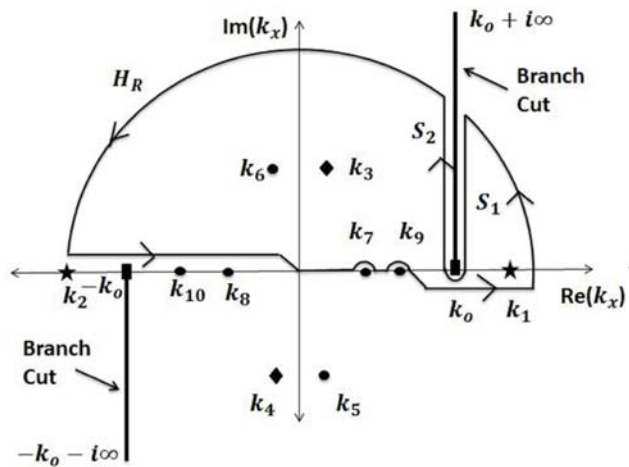


**Fig. 12.** Contour for frequencies below coincidence
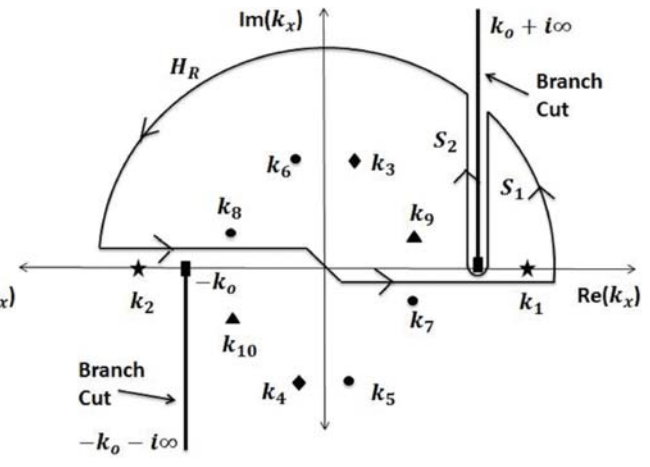


**Fig. 13.** Contour for frequencies above coincidence frequency

Here, the semi-circular contour portion $H_R$ will have zero contribution as per Jordan's lemma. Integral $S_1$ and $S_2$ are the branch cut integrals which need to be considered in the response calculation. Using the Cauchy integral theorem, contour integration can be evaluated in terms of residue. So, the improper integral is obtained as follows

$$\int_{-\infty}^{\infty} f(k_x) dk_x = Residue\left( f(k_n) \right) - \int_{S_1} f(k_x) dk_x - \int_{S_2} f(k_x) dk_x \tag{22}$$

The residue of $f(k_x)$ is given as follows:

$$Residue\ (f(k_x))|_{(k_x=k_n)} = \frac{(k_n^2 - k_o^2) e^{ik_n x}}{k_n((5k_n^4 - 4k_n^2 k_o^2 - k_p^4)} \tag{23}$$

The branch cut integral in the contour integral is given by

$$S(x) = S_1(x) + S_2(x) = \frac{F_o}{2\pi D} e^{ik_o x} \int_0^\infty \frac{-2i\sqrt{\left((k_o + iu)^2 - k_o^2\right)} \mu k_p^4 e^{-ux}}{\left[\left((k_o + iu)^4 - k_p^4\right)^2 \left((k_o + iu)^2 - k_o^2\right) - \mu^2 k_p^8\right]} du \tag{24}$$

Using these results, the non-dimensional form of the structural response of the plate is given by

$$\frac{\eta_{F_o}(x) D}{F_o h^3} = \eta_{F_o}^*(\chi) = \frac{1}{2\pi}\left[ \sum \frac{2\pi i (k_n^2 - k_o^2) e^{ik_n \chi}}{\kappa_n \left(5k_n^4 - 4k_n^2 k_o^2 - k_p^4\right)}\bigg|_{k_n = k_1, k_3 \, or \, k_1, k_3, k_9} - \int_0^\infty \frac{-2i\sqrt{(k_o + iU)^2 - k_o^2} \mu^* k_p^4 e^{(-U + ik_o)\chi}}{[(k_o + iU)^4 - k_p^4]^2 \left[(k_o + iU)^2 - k_o^2\right] - \mu^* k_p^8} dU \right] \tag{25}$$

In this work, the integral above is computed through numerical quadrature.

Here, the non-dimensional parameters are defined in the following manner: $k = kh$, $\chi = x/h$, $\mu^* = \mu h$. As discussed earlier, for frequencies below the coincidence frequency the residues corresponding to poles at $k_1$ and $k_3$ are accounted. Likewise, for frequencies above the coincidence frequency, the residues corresponding to poles $k_1$, $k_3$ and $k_9$.

### 3.4 *Finite Element Method*

In the previous section, we discussed the FE modelling procedure for the uncoupled analysis of the semi-infinite plate. In the coupled problem, we need to additionally model the unbounded acoustic domain for the region $y > 0$. Here, we explain the FEM model development in ANSYS for the coupled analysis of the semi-infinite plate.

As discussed in section 2.2, a semi-infinite plate is modelled as an equivalent beam placed on tuned linear and torsional dampers as shown in Figure 14. The acoustic domain is modelled as a semi-circular finite domain with radius l. The interior of this region is modelled with acoustic FLUID29 elements. In order to simulate an unbounded acoustic domain, we apply a layer of infinite elements FLUID129 as shown in Figure 14[9]. Infinite element incorporates an anechoic condition at the semi-circular boundary, thus simulating the effect of an unbounded acoustic domain. At the common nodes between the fluid and the structure, the kinematic continuity is enforced. Fluid elements in contact with the beam are modified as interacting elements with structure[9]. Coupled harmonic analysis is performed on this FE model.
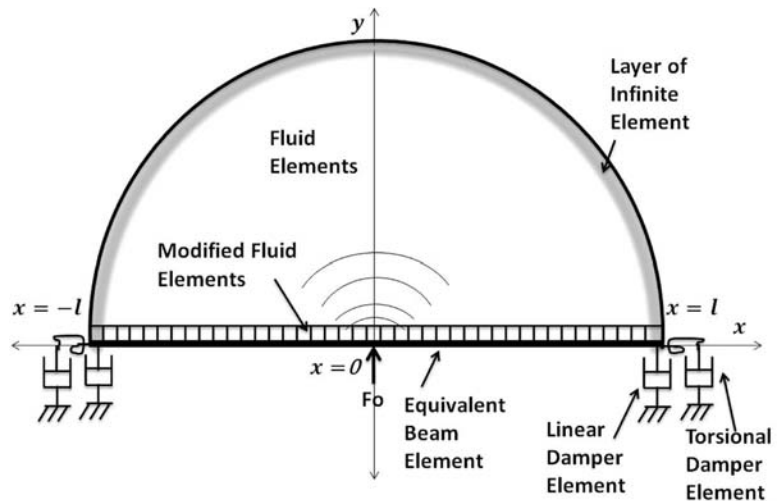


**Fig. 14.** FEM model for coupled semi-infinite plate

### 3.5 *Results and Discussion*

Analytically, the coupled structural response of a semi-infinite plate under line force is given by equation (25). The results obtained from these relations are plotted in Figure 15. The deformation plots at representative frequencies below and above the coincidence frequency are shown in Figures 15a and 15b, respectively. The drive point frequency response function (direct FRF) is plotted in Figure 16 Also, overlaid in these figures are the corresponding results obtained through FE simulations. The non-dimensional parameters used for these results are tabulated in Table 1. The table also presents the complex poles $\kappa_1$, $\kappa_3$, $\kappa_9$ used in the computation of the response. Note, $\kappa_9$ is not used in the computation of the response for frequencies below the coincidence frequency. Excellent correlation of the results obtained using the two methods is noted.
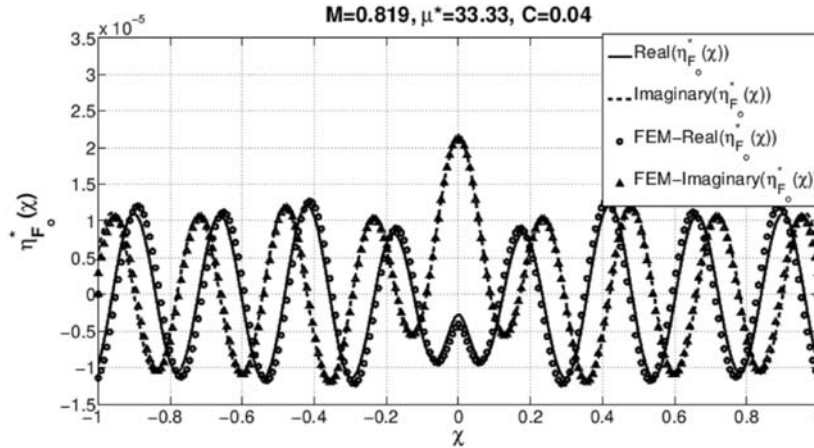


(a) Deformation plot for below coincidence frequency
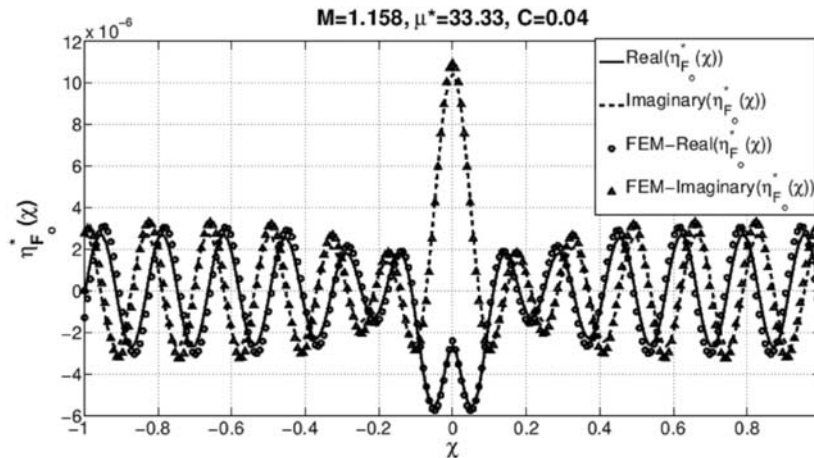


(b) Deformation plot for above coincidence frequency

**Fig. 15.** Coupled structural response of a semi-infinite fluid loaded plate under line force excitation

**Table 1.** Values of the non-dimensional parameters used for the results shown in Figures 15 and 16.

| M | $\kappa_p$ | $\kappa_0$ | $\kappa_1$ | $\kappa_3$ | $\kappa_9$ |
|---|---|---|---|---|---|
| 0.819 | 20.458 | 16.755 | 26.132 | 4.551+22.700 i | undefined |
| 1.158 | 28.932 | 33.510 | 37.786 | 4.678+30.433i | 28.952+9.290i |
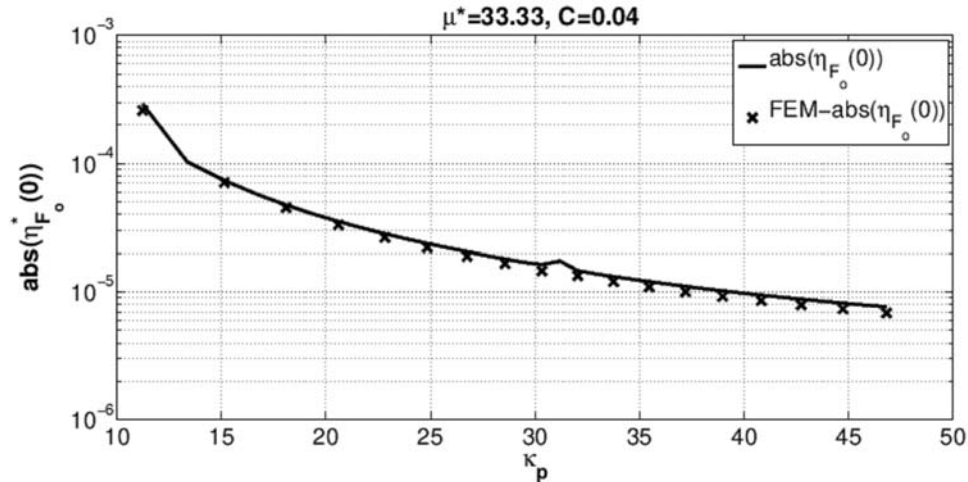
**Fig. 16.** Drive point FRF for the coupled structural response of a semi-infinite fluid loaded plate under line force excitation

## 4. CONCLUSION

In this article, we have reviewed a classical solution in structural acoustics, namely that of a semi-infinite plate submerged in an acoustic half space and excited by a harmonic line forcing. The analytical solution of this problem was given by Crighton[1, 2]. However, in Crighton's works no validation of the results were presented. In the present study, we rework the solution using FEM simulation in a commercial package (ANSYS). The FEM simulation is accomplished by using the analogy between the semi-infinite plate and the beam equations. Further, the infinite structural domain is modeled by placing the ends of the beam structure on appropriately tuned linear and torsional dampers. The damping coefficients of these dampers have been suitably chosen such that the anechoic end conditions are incorporated by the structure. The in-built infinite acoustics elements in ANSYS are used to simulate the infinite acoustic domain. To the best of our knowledge, this simulation methodology has not been reported in the literature. The solutions obtained using the above simulation methodology correlates well with the analytical solutions presented by Crighton. For brevity, in the present work, we have reported results only for the structural response. A more complete analysis with the inclusion of the acoustic results is given in[10]. It is envisioned that the present review of Crighton's work together with its validation employing FEM based simulation will make his works more accessible to practicing engineers and young researchers in the field of structural acoustics.

## 5. REFERENCES

[1]   D.G. Crighton, 1989. The 1988 rayleigh medal lecture: fluid loading the interaction between sound and vibration. *Journal of Sound and Vibration,* **133**(1), 1-27.

[2]   D.G. Crighton, 2012. Fluid loading interaction with vibrating surfaces. In DG Crighton, Ann P Dowling, JE Ffowcs Williams, MA Heckl, and FA Leppington, editors, Modern Methods in Analytical Acoustics: Lecture Notes, chapter 17, *Springer Science & Business Media,* 510-521.

[3]   D.G. Crighton, 1979. The free and forced waves on a fluid-loaded elastic plate. *Journal of Sound and Vibration,* **63**(2), 225-235.

[4]   D.J. Mead, 1999. Passive Vibration Control. *John Wiley & Sons Inc.*

[5]   F.J. Fahy and P. Gardonio, 2007. *Sound and Structural Vibration: Radiation, Transmission and Response.* Academic press.

[6]     W.A. Strawderman, Sung-Hwan Ko and A.H. Nuttall, 1979. The real roots of the fluid-loaded plate. *The Journal of the Acoustical Society of America,* **66**(2), 579-585.

[7]     D.G. Crighton, 1980. Approximations to the admittances and free wavenumbers of fluid-loaded panels. *Journal of Sound and Vibration,* **68**(1), 15-33.

[8]     D.J. Rothwell and M. Purshouse, 1988. The transfer admittance of a point-excited, fluid-loaded plate. *Journal of Sound and Vibration,* **120**(3), 431-443.

[9]     ANSYS Mechanical APDL Acoustic Analysis Guide v16.0. www.ansys.com, 2013.

[10]    Jaykumar A. Balodia, 2017. Structural acoustics of a constrained semi-infinite plate in an acoustic half-space: a wave propagation approach. MS Thesis, Department of Mechanical Engineering, *Indian Institute of Technology Madras.*

# Vibro-acoustics of the South Indian Drum *Mridangam*

**Sooraj G.[1] and Chandramouli Padmanabhan[2]**
*[1]Currently Edison Engineer (EEDP), GE India Industrial Pvt. Ltd., Bengaluru*
*[2]Department of Mechanical Engineering*
*Indian Institute of Technology Madras, Chennai-600 036*
*e-mail: mouli@iitm.ac.in*

## ABSTRACT

The *mridangam*, a south Indian drum, produces harmonic musical notes. This is believed to be due to the central mass loading of the right side membrane, called *Karanai*. This paper investigates whether this is due to the fact that the first few in-vacuo modes are integer multiples or this happens due to the vibro-acoustic interactions of the *Karanai* and possibly the membrane on the left side (called *Thoppi*) with the enclosed acoustic cavity. To achieve this objective, initially, finite element models of the membranes, as well as the enclosed acoustic cavity, are generated. These models are validated by carrying out carefully conducted experiments on the individual components. From these models, it is established that the in-vacuo natural frequencies of the *Karanai* are already integer multiples, while those of the *Thoppi* is not so. Following this, the acoustic and membrane finite element models are coupled together; the coupled system response to standard finger stroke excitation is obtained. The results clearly demonstrate that vibro-acoustic coupling happens only between the axi-symmetric membrane modes and axial acoustic modes. However, the coupling has no significant effect in changing the response of the *Karanai* membrane. For the *Thoppi* the only significant effect is around the first coupled-mode frequency. Hence, one can conclude that the acoustic cavity has no major role in the musical notes' generation.

## 1. INTRODUCTION

In the past century, only a few investigations, on the vibro-acoustic characteristics of *mridangam* and similar Indian drums, have been reported. Most of these have been experimental investigations on fully assembled instruments, while a few have focused on building analytical models primarily for the vibration of the centrally loaded membrane, called *Karanai*. Raman and Kumar[1] were the first to observe the sustained intensity of the first three harmonics of tuned Indian drums. They had also commented on the importance of the heterogeneous composite membranes and the central mass loading. A decade later, Raman[2] took a significant step towards understanding of such drums . It is the first modern day article to elaborate on the characteristics and construction of a *mridangam*. However, the experimental results and images shown seems to be from the *Syahi* of a *Tabla*; it must be noted that the *Karanai* of a *mridangam* and the *Syahi* of a *Tabla* are closely related. He showed that the natural frequencies, were integer multiples due to the presence of the central mass loading and some of these involved degenerate modes of the composite membrane. Rossing[3] provided more details about these degenerate modes and their superposition.

An analytical model for the centrally loaded membranes *(Karanai/Syahi)*, proposed by Ramakrishna and Sondhi[4], showed very good correlation with the experimental observations by Raman[2]. This model was far more physically accurate and realizable compared to the earliest model by Ghosh[5] or later by Malu and Siddharthan[6]. The natural frequencies and mode shapes were obtained using Bessel's functions, with compatibility enforced at the interface between the loaded and unloaded regions. The density and diameter ratios between the loaded and unloaded regions are the key parameters governing the design. Bridge and Keshavan[7] used several trigonometric functions in a Galerkin formulation to obtain the approximate natural frequencies and mode shapes of the bi-density membrane; they validated their results with those of Ramakrishna and Sondhi[4]. Sathej and Adhikari[8] proposed analytical models for the membranes of a Tabla, which were solved using a high resolution Fourier- Chebyshev collocation method, while Sarojini and Rahman[9] proposed variational methods to model both the membranes of a Tabla. All these authors implicitly assumed that the in-vacuo modes of the membrane were already integer multiples; the influence of the enclosed acoustic cavity towards determining the instrument's harmonic notes was never considered.

Gottlieb[10] investigated the effect of the air cavity behind a drum membrane. It was found that there was only a slight increase in the fundamental frequency, with no significant change for other modes; the analytical method considered only axi-symmetric modes of the membrane. Christian *et al.*[11] studied the effect of the air cavity below the membrane on the acoustics of a kettledrum. The key observation was that the air cavity makes the instrument with a simple membrane (uniform density, circular membrane) harmonic. But, the frequency shifts were found to be more sensitive to the total kettle volume than its geometry details. A similar observation was made with respect to the Tabla in a more recent paper[12], where the cavity influenced the left-hand instrument more than the right hand one.

Bhat[13] investigated the effect of air-cavity on the vibration of the *mridangam* membrane (*Karanai*) by considering only the axi-symmetric membrane modes. This is due to the assumption that with the kettledrum effect of the cavity only these vibrations can be sustained. He concludes that the lowest axi-symmetric mode is influenced significantly by the acoustic pressure. Only when a certain non-dimensional parameter, involving the speed of sound in air, the radius of the drum, volume of air in the cavity and tension, becomes large do the frequencies become harmonic. It is stated in the paperthat the in-vacuo modes are not harmonic (which corresponds to the non-dimensional parameter being zero). This is the only research paper (to the best of the authors' knowledge) where at least a limited form of vibro-acoustic coupling has been considered in the study of *mridangam*. A recent conference paper, by Gupta *et al.*[14], studies the vibro-acoustic coupling in the context of the dholak, a similar bi-facial drum as the *mridangam*.

As can be seen from the review, only limited research on *mridangam* and related Indian percussion instruments has been carried out. The only paper dealing with the vibro-acoustics of the *mridangam* used simplifying assumptions about the effect of the acoustic cavity to arrive at the conclusion that the in-vacuo modes of the *Karanai* membrane are not harmonic. Further, almost no one has investigated the dynamics of the *Thoppi* and its interaction with the air cavity as well as the *Karanai*, if any. The broad objective of this paper is to use a finite element framework, to help understand the true nature of the coupling between the membranes and the acoustic cavity in between them. The framework helps minimize the assumptions to be made about the vibro-acoustic interactions, as well as help model the actual geometry. To accomplish this finite element (FE) models are generated independently for the *Karanai*, *Thoppi* and acoustic cavity. Each of these models are validated by carrying out well designed experiments; the wooden shell has been neglected as it is found to play an insignificant role. Following this the coupled vibro-acoustic model is generated from the individual component models. The response of the membranes to standard finger stroke excitation is studied using this coupled model.

## 2. COMPONENT MODELING AND EXPERIMENTS

### 2.1 *Karanai*

The *Karanai*, a membrane with a central black region, usually on the right side, is a common feature

that *mridangam* has with its cousin Tabla. Both membranes share very similar traits owing to the presence of a black patch. They have two distinct regions - the central region with an additional mass loading (special solid material) and the rest comprising only of stacked leather layers.

First, in-vacuo vibration experiments were done on the *Karanai* as a stand-alone component. The experiments were designed towards extracting the natural frequencies, and identifying corresponding modes of vibration. The method adopted uses fine sand to visualize the nodal regions (Chladni patterns) of a resonating membrane.

A custom made open fixture, shown in Figure 1, has a 25.4 mm deep wooden ring, with other dimensions being the same as that of the *mridangam* shell rim on the *Karanai* side. The membrane is stretched against this ring using 16 bolts, replicating the tightening setup on the original *mridangam*. Through hole button-type load cells are fixed to every alternative bolt, to measure the tension exerted on the hooks (see Figure 1). A point force excitation using an electro-dynamic shaker is applied on the membrane. A single microphone measurement using a free- field microphone (kept at a distance of 100 mm from the plane of the membrane, along the *Karanai* central axis) is used to identify the resonance frequencies. Several rounds of sine sweeps were used to spot the frequencies causing vigorous movement of sand particles. Each of these resonances were recreated using pure sine wave excitation at that frequency, and the corresponding sand patterns were photographed.



(a)  (b)
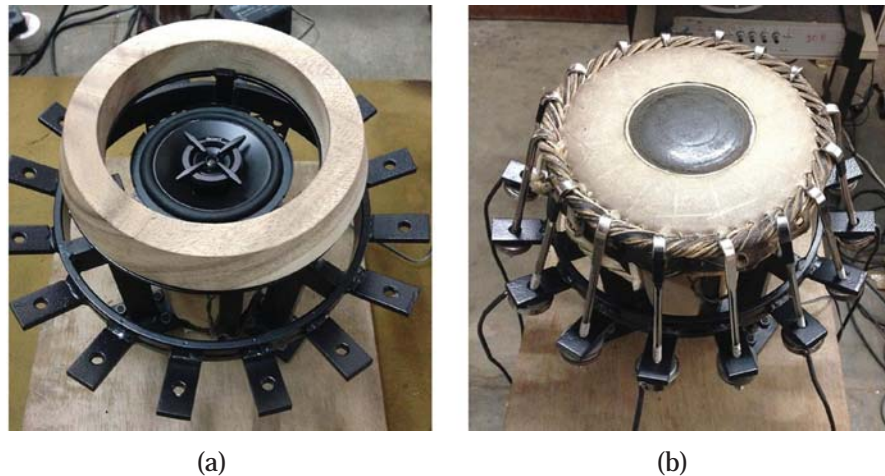
**Fig. 1.** In-vacuo experiments on Karanai, (a).  support structure and (b). final assembly.

The *moottu* (an assembly composed of buffalo braided ropes passing through the composite membrane as seen at the periphery in Figure 1b), while ensuring that the tension is evenly distributed, has limitations. The pulling force, that the hooks exert, is primarily used to expand the buffalo leather braids against the shell, which expand to such an extent that the bottom layer of the *moottu* fits perfectly over the shell rim. Thus, the membranes receive only a portion of the load and one has to tune this in the analytical/numerical model to match the experimentally obtained results.

The *Karanai* numerical model is an adaptation of the analytical model by Ramakrishna and Sondhi[4]. There are three layers making the *Karanai*, with the central black patch supported on the middle goat leather layer; the top and bottom are from cow leather. For modeling purposes, the 3 layers are assumed to act as a single membrane. The density of the black patch and leather layers are calculated from mass and volume measurements. The density of black patch is found out by submerging granules of dried black patch in liquid hexane, as it is insoluble and non-reacting in it. The goat and cow leather densi*TIE*s of 792 and 883 kg/m³  are calculated by weighing rectangular strips of the leather (known volume). The region with the black patch has a thickness of 3 mm, out of which 0.4 mm is goat leather. Thus, its effective

density is 2178 kg/m$^3$. In the numerical model, however, the thickness of all the layers is assumed to be 0.8 mm uniformly across both regions and hence the black patch has an effective density of 8168 kg/m$^3$, while the leather region has an effective density of 836 kg/m$^3$.

The membrane was modeled using S4R (4-noded shell) finite elements in the commercial software Abaqus. The analysis is carried out with hourglass control on. The choice of shell elements rather than membrane elements is particularly due to the inability of the M3D4 membrane elements to automate edge loads assigned to the geometry. It is observed that the shell effects vanish when the thickness of the *Karanai* model is brought down to 0.1 mm; Thus, an effective thickness of 0.1 mm is used in the final model and the density values are scaled appropriately. The modulus of elasticity was also increased by 10 times (to 100 MPa) to avoid large deformations arising due to a thinner cross section. The natural frequencies compare well with experimental data, as seen in Table 1. The second mode shape is compared in Figure 2. It can be seen from Figure 3 that the two closely spaced modes seen in the numerical analysis (for the third and fourth modes), appear as a combination mode in experiment; this was pointed out by Rossing[3]. These experiments clearly establish the fact that the first four in-vacuo natural frequencies, including the degenerate modes, are integer multiples of the fundamental mode. This clearly contradicts the conclusions of Bhat[13], who asserted that the kettledrum effect of the cavity was instrumental in making the frequencies to be harmonic.

**Table 1.** Experimental vs. numerically computed natural frequencies of *Karanai* (in Hz).

| Experiment | Numerical | Ratio |
|---|---|---|
| 168 | 165 | – |
| 327 | 325 | 1.97 |
| 495 | 486/504 | 2.95/3.05 |
| 684 | 655/677 | 3.97/4.10 |

### 2.2 *Thoppi*

The *Thoppi* on the left side, is again a 3-layered membrane, with the bottom membrane made from goat hide and two annular stiff layers from buffalo leather on top of it. During a concert, a central mass loading (wet synthetic clay or *rava*) is used on the goat hide. No research has been published on its vibration characteristics or its interactions with the acoustic cavity. This has been investigated possibly for the first time.
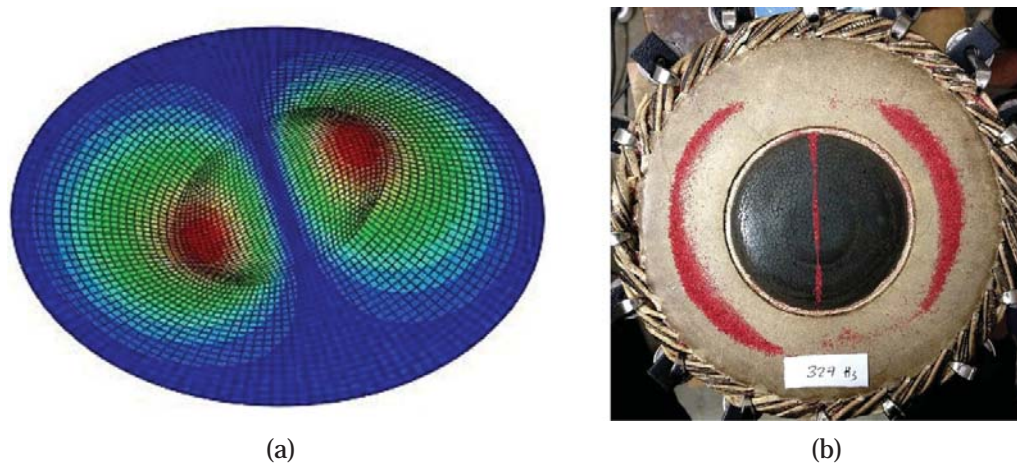


(a)                                    (b)

**Fig. 2.** Comparison of mode shapes for the Karanai second mode, (a). Numerical and (b). Experimental.

(a)                                                    (b)
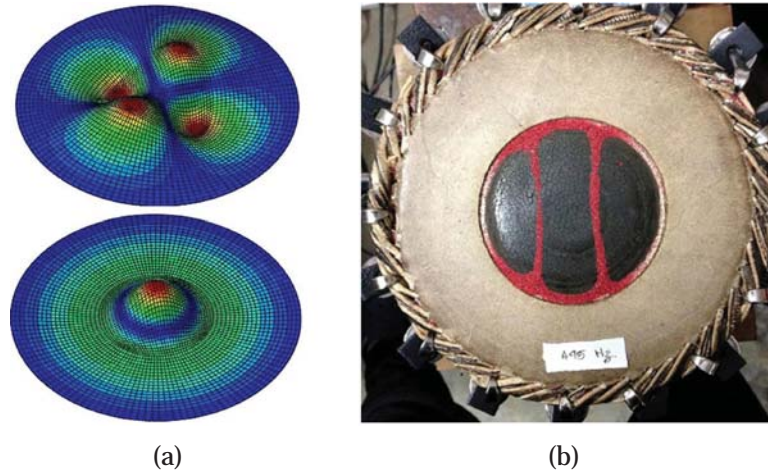
**Fig. 3.** (a). Two close modes corresponding to third natural frequency (Numerical) and
(b). single combination mode (Experimental).

The experiments on *Thoppi* are similar to the ones carried out on *Karanai*. The support structure compatible to the dimensions of the membrane is the only difference between the two setups. The vibration response is extracted for both with and without the synthetic clay loading at the middle. The resonant frequencies are found as done earlier and photographs of Chladni sand patterns are taken. Beyond the fundamental frequency, the resonances of the *Thoppi* (under point force excitation) are not strong enough and the excitation needed to be increased to achieve reasonable membrane motion; the presence of two stiff buffalo hide annular rings is the reason for this.

The *Thoppi* membrane finite element model is simplified by neglecting the contact between the two buffalo layers and the soft goat skin below. It is assumed to be a linear model with three distinct sections of different densi*TIE*s and stiffness. A dry *Thoppi* membrane is modeled to represent the results from experiments adequately and later the wet *Thoppi* is modelled by tweaking existing proper*TIE*s. The stiffness of the buffalo leather region and its possible shell like behaviour can make an analytical membrane model inaccurate.

During recital, the goat skin and *rava* are moistened with water; the experiments were done in a dry state. Hence, two different models with appropriate changes to the material proper*TIE*s to reflect the two states was constructed. The Young's modulus of the clay and goat hide regions were reduced for the wet state to about 15% of the original values. The density of dry clay was assumed to be 525 kg/m$^3$ (and increased to 550 kg/m$^3$ when wet) with the other layer densi*TIE*s as before (wet goat layer density was increased from 790 to 850 kg/m$^3$).

The comparison between the experimental and numerical natural frequencies of the dry *Thoppi* is shown in Table 2. The values from simulation for the first two modes are quite close but there is a split in the 3$^{rd}$/4$^{th}$ mode in simulation while the experiment (like the *Karanai*) shows a combination mode at a slightly higher frequency; see Figures 4 and 5 for a comparison of the first two modes. From these results it is clear that the natural frequencies of the *Thoppi* are not integer multiples.

**Table 2.** Comparison between experimental and numerical (dry clay) natural frequencies of *Thoppi* (in Hz).

| Experiment | Numerical | Ratio |
|------------|-----------|----------|
| 146 | 180 | – |
| 242 | 296 | 1.65 |
| 399 | 334/395 | 1.85/2.2 |

(a)                                                    (b)
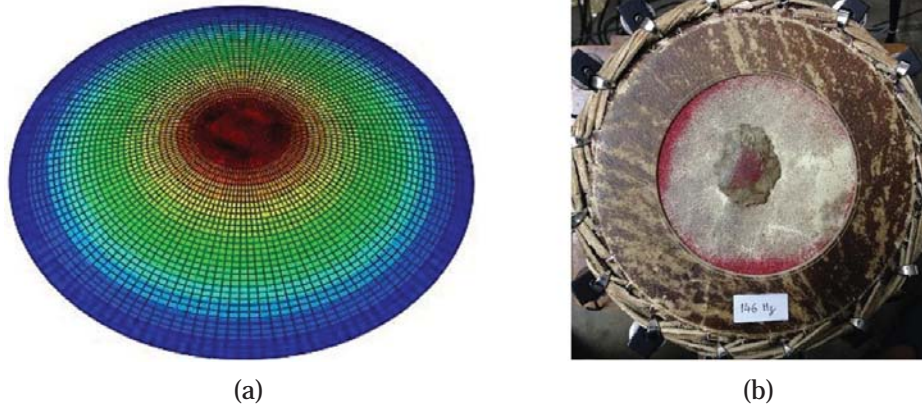
**Fig. 4.** Comparison of first mode of *Thoppi*, (a). Simulation and (b). Experiment



(a)                                                    (b)
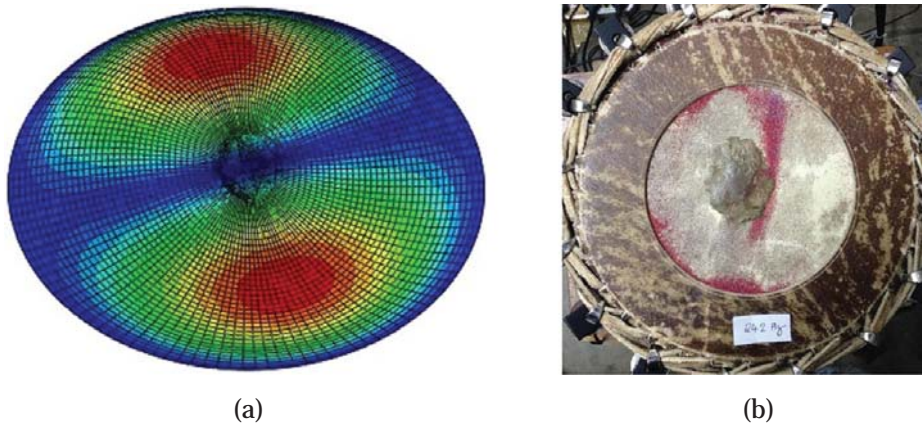
**Fig. 5.** Comparison of second mode of *Thoppi*, (a). Simulation and (b). Experiment.

### 2.3 *Mridangam* Acoustic Cavity

Membranophones like *mridangam*, tabla, kettledrum, *Wadaiko* drum, have enclosed air cavi*TIE*s that interact with the vibrating membranes. The function of the air cavity in a kettledrum, for instance, is to make it harmonic. In a *mridangam*, it has been established in Section 2.1 that an in-vacuo *Karanai* has natural frequencies which are integer multiples. This then raises an important question regarding the role played by the acoustic cavity in a *mridangam*. An experimental study was first done to understand the behaviour of the enclosed air cavity; a numerical model is developed following the experimental study.

The enclosed air cavity of a *mridangam* consists of three different sections. Two cylindrical regions near to the membranes and a barrel shaped region. An experiment is carried out to find out the cavity natural frequencies. The experiments and numerical analysis were carried out assuming that the cavity boundaries are rigid. On the lateral surface, the wooden shell, which is relatively thick and heavy, provides such a boundary. At the ends, a rigid boundary is achieved by using 16 mm thick plexiglass caps. However, at the *Karanai* side of the shell, there is a 4 inch (101.6 mm) circular hole at center of the cap to house a loudspeaker. This loudspeaker serves as the acoustic excitation during sound measurements. The excitation signal from the data acquisition system (DAQ) is amplified using a commercial amplifier and fed to the loudspeaker. On the *Thoppi* side, the plate has a 3/4 inch hole at the center to hold a steel pipe. The steel pipe houses a microphone at its end, as shown in Figure 6.

A numerical model is developed using Simulia Abaqus[15]. An acoustic solid region of the measured geometry, assigned with AC3D8 elements (3D and 8-noded), is used for analysis. Ihlenburg[14] has suggested that one should use quadratic elements for acoustics. However, since the use of a linear element simplifies the coupling of the cavity with the membranes (4-noded shell elements), it was preferred. The physical proper*TIE*s of air, such as density and bulk



**Fig. 6.** Mridangam Acoustic Cavity Experiment Setup.

modulus are assumed to be 1.2 kg/m$^3$ and 142 kPa respectively. The entire boundary of the cavity is assumed to be perfectly rigid and smooth. A standard convergence study was carried out to ensure accuracy of the first 15 modes.

The natural frequencies from the numerical analysis are in good agreement with the experimental values and the errors are within acceptable limits (see Table 3). It is important to note that the experiment successfully captured all the axi-symmetric modes (see Figure 7) but missed the non- axi-symmetric (fourth

**Table 3.** Comparison of cavity frequencies (in Hz) between experiments and FE simulations.

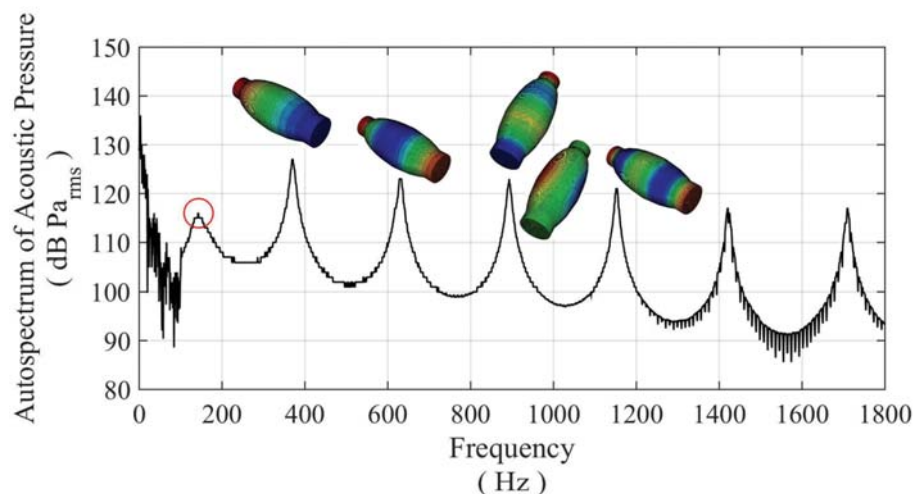| Experiment | Numerical | Ratio |
|:---:|:---:|:---:|
| 370 | 361 | Axial |
| 628 | 611 | Axial |
| 893 | 856 | Axial |
| – | 896 | Transverse |
| – | 1092 | Transverse |
| 1152 | 1114 | Axial |



**Fig. 7.** Comparison of cavity mode frequencies between experiment and simulation with mode shapes from FE simulation; 4th mode shown is a non-axial mode and not captured in experiment due to the microphone traversing along the axis of the cavity.

mode at 896 Hz shown and fifth mode at 1092 Hz) ones. All the modes with a nodal line along the axis of the cavity could not be captured, as the placement of the microphone was along the nodal axis. However, the comparison of the axi-symmetric modes is deemed sufficient to ensure the accuracy of the numerical model. There is also a peak shown by the red circle which is possibly due to the support structure but is not present in the numerical models.

## 3. COUPLED VIBRO-ACOUSTIC MODEL

### 3.1 Modal Analysis

The numerical models of the components discussed in Section 2 are imported and assembled to create the coupled model. The coupling between the membranes and the cavity was modeled using the surface-based acoustic-structural interaction (ASI) option in Abaqus[15], which is accessible through surface based *TIE* constraints option. In this model, the membrane surfaces are chosen as the master surfaces and the adjacent cavity surfaces are the slaves. To check that the results from the numerical model are consistent, the master- slave surfaces were flipped. However, the former configuration is important to apply loads on the external surface (the ones facing outside) of the membrane later. For such a choice of master and slave elements, the *TIE* function assigns three displacement degrees-of-freedom (DOF) to the nodes on the slave surface which previously had only one DOF (acoustic pressure). The introduction of ASI elements tweaks the mass and stiffness matrices to account for the coupled system. The Lanczos eigen value solver is used to calculate the natural frequencies and mode shapes of this model.

The analysis is carried out in four steps, similar to the in-vacuo numerical analyses. In the initial step, the translational and rotational DOF of the center point of both the membranes are arrested. In the second step, the membranes are subjected to tension- which is modelled as a shell edge load. It is to be noted that the *Karanai* tension is increased to 3200 N/m from 3091 N/m (shell edge load that produce a fundamental frequency of 164.8 Hz in the in-vacuo *Karanai*) to obtain the desired frequency of 164.8 Hz in the coupled model. The tension on the *Thoppi* side remains unchanged. Since the adaptive mesh option is switched off in this static analysis step, the cavity elements coupled to the membranes are not affected by the stretching of the membranes. Later, the nodes on the slave surface are *TIE*d to the membrane surfaces which are already in the stretched state. In the third step, the translation DOF at the boundaries of the membranes are arrested. The boundary conditions on the central nodes of both membranes are made inactive in this step.

The effect of these loads and boundary conditions are built- in to the system prior to the fourth step, which is a natural frequency analysis using Lanczos solver with strong structural-acoustic coupling option enabled; the *Thoppi* was assumed to be in wet state (as in a concert).

Despite a full (strong) coupling of the models, the membrane natural frequencies have been lowered only by a small margin (typically by about 4 to 6 Hz), as seen from Table 4. An exception to this is exhibited by the first mode of *Thoppi* which shows an increase from an in-vacuo fundamental frequency of 84 Hz

**Table 4.** Natural frequencies of a few well coupled modes.

| Major Contribution from | Uncoupled (Hz) | Coupled (Hz) |
|---|---|---|
| *Thoppi;* first mode | 84 | 94 |
| *Karanai;* first mode | 168 | 165 |
| *Thoppi ;* third mode | 177 | 173 |
| *Thoppi;* eleventhmode | 350 | 345 |
| *Cavity;* first mode | 361 | 381 |
| *Thoppi* | 495 | 488 |
| *Karanai;* third mode | 514 | 510 |

to 94 Hz, when coupled. Such an increase has been observed earlier by Gottlieb[10]. The well coupled modes till the third harmonic of the instrument tuning frequency (about 500 Hz) are listed in Table 4.

The axi-symmetric modes of the membranes couple well with the axial cavity modes as seen in Figures 8 and 9; the first one shows the *Thoppi* mode whose natural frequency when coupled increased to 94 Hz, while the second shows the first *Karanai* mode with the frequency reducing marginally from 168 to 164 Hz on coupling. This is in tune with the assumption made by Bhat that only axi-symmetric modes of the membrane couple with the acoustic pressure. However, there is almost no change in the integer ratios of the coupled *Karanai*-acoustic cavity natural frequencies when compared to the in-vacuo frequencies of the *Karanai*. Hence one can conclude that in the case of the *mridangam* there is really no kettledrum effect; this is in contrast to the conclusion arrived at by Bhat[13].



(a)  (b)
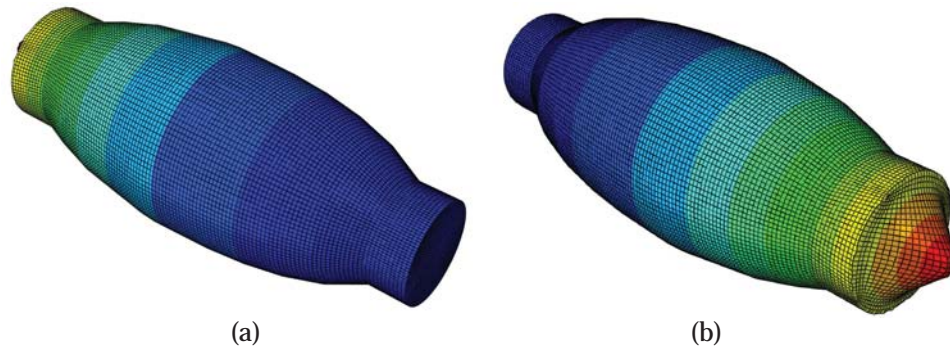
**Fig. 8.** First coupled mode showing dominant *Thoppi* motion;
(a). view from *Karanai* side and (b). from *Thoppi* side.



(a)  (b)
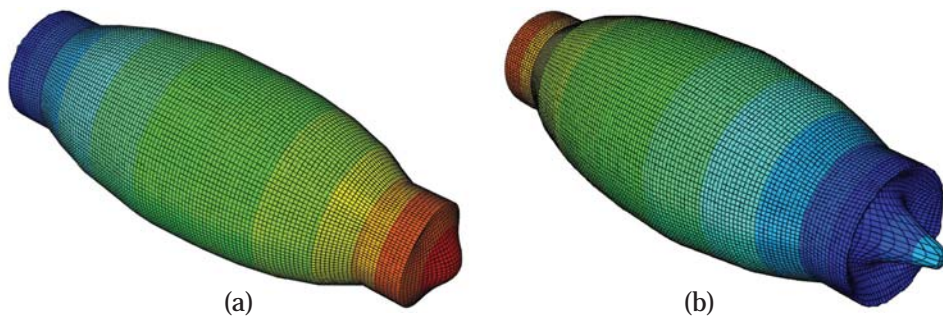
**Fig. 9.** Another coupled mode showing dominant *Karanai* motion;
(a). view from *Karanai* side and (b). from *Thoppi* side.

The non axi-symmetric modes of the membranes are capable of producing only local pressure changes as shown in Figure 10. For both the membranes, the natural frequencies of non axi-symmetric modes are close to their corresponding in-vacuo modes. These non axi-symmetric modes occur in degenerate and orthogonal pairs. It is also clear that the *Karanai* modes create more significant motion on the *Thoppi* side, for the strongly coupled modes.

The first dominant acoustic mode of the cavity, which has a natural frequency of 360 Hz in the uncoupled model, appears at 380 Hz in the coupled model. The second acoustic mode of the cavity is increased from 610 Hz (cavity alone) to 626 Hz in the coupled case. Thus, within the fourth harmonic of the instrument (about 660 Hz) there are 9 well-coupled modes influenced by axi-symmetric membrane modes and the cavity. This does not mean that the non axi-symmetric modes do not contribute in the

**Fig. 10.** A non-axisymmetric *Thoppi* mode showing weak vibro-acoustic coupling;
(a). view from *Karanai* side and (b). from *Thoppi* side.

dynamics. They definitely set the membranes in vibration, but they are not capable of interacting with the other membrane through the cavity. In general, it is observed that the more complicated the in-vacuo cavity and membrane mode shape patterns, the less the change in their natural frequencies and mode shapes after coupling.

## 3.2 Transient Vibration Response

The nature of excitation on a system determines the mode shapes participating in the response. The excitation on a *mridangam* are the *chaapu* and *thom* strokes played on the *Karanai* and *Thoppi* sides (see Figure 11).



**Fig. 11.** Typical mridangam finger strokes, (a). chaapu on the *karanai* and
(b). thom on the *thoppi* side; photos taken in the lab when played by the *mridangam* maker.

A *chaapu* stroke is played by a combination of two fingers; the little or ring finger lightly taps the boundary of black patch at the beginning of the stroke followed by the tapping of the index finger on the annular region. There are slight variations in the technique based on different schools of *mridangam* recital. The stroke is expected to produce a sound with a strong sense of the tuning frequency (165 Hz in this model) and some additional harmonics to add richness. The *thom* stroke, played on the *Thoppi* side, is an open or ringing tap at the centre of the *Thoppi*, with a closed palm. The impulse on the *Karanai* consists of two regions, both modelled as pressure forces on the surface. For the *Karanai*, the magnitude of the impulse on the black patch region is 0.025 Ns over 3 ms and on the annular region is 0.075 Ns over 3 ms (see the regions marked by thick boundaries in the time response plot in Figure 12). The shape of the impulse has been chosen from the literature, where measurements have been made on a *rototom* drum[16].

The magnitudes have been adjusted to obtain realistic vibration response amplitudes. It is to be noted that the second pulse on the annular region has a time lag of 0.5 ms from the first one on the black patch,

to mimic an actual *chaapu* stroke. For the *Thoppi*, the *thom* stroke is modelled as a pressure force on the *rava* region, with a total force magnitude of 0.005 Ns over 3 ms. The response is calculated for a total duration of 0.3 s, which is more or less the duration of decay for the sound response from these strokes.

Modal superposition based dynamic analyses are carried out with a constant 3% direct modal damping assumed for all modes of the coupled system. The choice of the first 150 modes (which spans 850 Hz) is more than sufficient since all the major modes of interest lie within 600 Hz. Moreover, the impulse duration of 0.3 ms is expected to strongly excite modes below 330 Hz; hence, the choice of 850 Hz as upper cut-off frequency is adequate. The vibration time response of the membranes are obtained; a Fast Fourier Transform (FFT) of the time response is used to identify the dominant frequencies in the response. The response at two different points (center and off-center) are compared with the in-vacuo response of the same membrane; modal damping of all modes remains at 3% for the uncoupled case too. In all the following figures, the region of excitation is marked by a white region with a thick boundary and the response point is marked with a thick black dot.



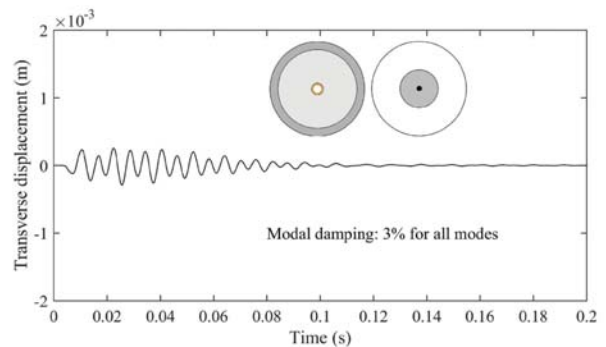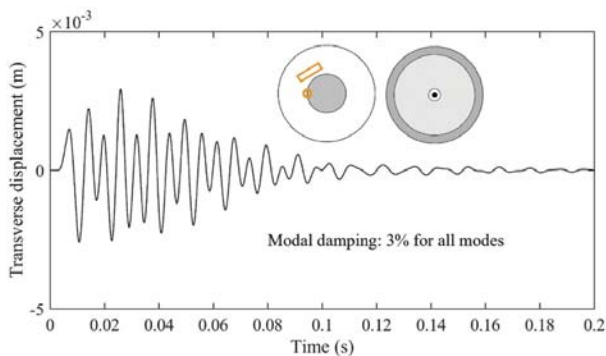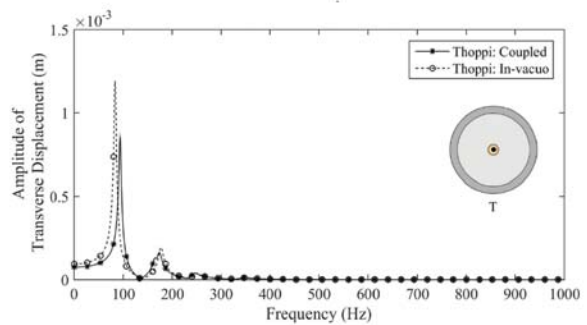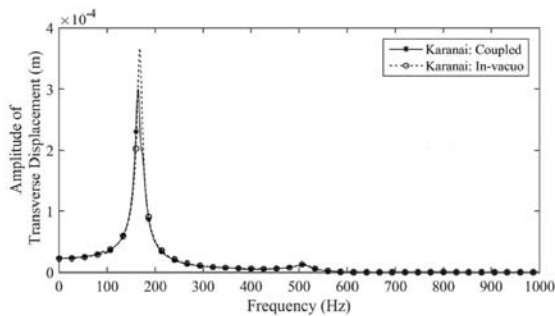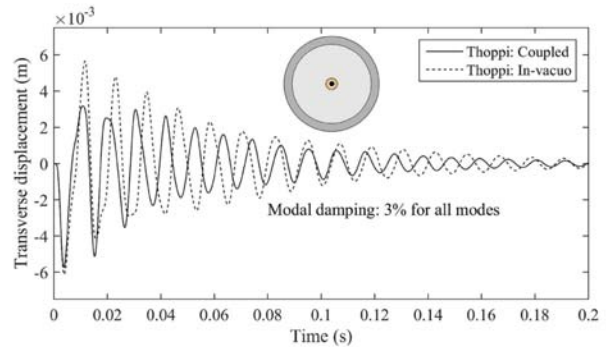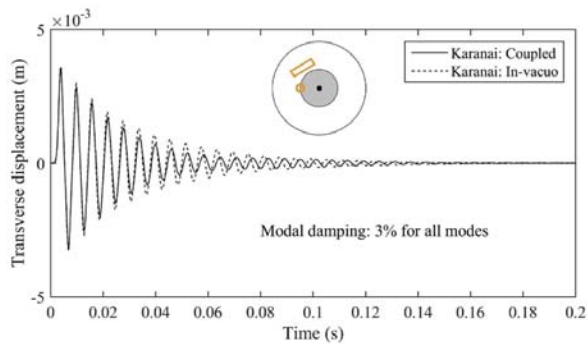**Fig. 12.** Vibration response to chaapu excitation, (a). Karanai centre (b). FFT of the time signal in (a), and (c). Thoppi centre time response.

**Fig. 13.** Vibration response for thom excitation, (a). thoppi centre , (b). FFT of thoppi response in (a), and (c). karanai centre.

Figure 12 shows the time response of the center points of *Karanai* and *Thoppi* to a simulated *Chaapu* stroke. In the first few cycles there is virtually no difference between the in-vacuo and coupled response; the coupled vibration response is marginally lower than the in-vacuo past the initial few cycles. An examination of the FFT (see Figure 12b) demonstrated that the dominant frequency is that of the first *Karanai* mode while the first mode of the *Thoppi* (around 84 Hz) is not present in the response. The FFT also showed a peak around 510 Hz for both coupled and uncoupled responses with the amplitudes being equal. The *Thoppi* responds to the excitation on the *Karanai*, as the energy is transferred through the air cavity; the first two modes are dominant. When the *Karanai* response at an off-center location is examined, the non-axisymmetric mode around 320 Hz has a significant contribution; again this observation is in contrast to the findings of Bhat[13], who claimed that in the transient response the non-axisymmetric modes will not occur. Once again there is not much difference in the amplitudes between the in-vacuo and coupled vibration responses, reinforcing the fact that the is no kettledrum effect of the cavity on the *Karanai* response.

Figure 13 shows the vibration response at the center of the *Thoppi* for a *Thom* stroke. There is a difference in the response amplitudes/characteristics between the in-vacuo and coupled models. The presence of the *Karanai* first mode frequency close to the *Thoppi* second mode changes the coupled model response characteristics; from a music stand point whether this is desirable needs to be addressed. The *Karanai* response to *Thoppi* excitation is much smaller in amplitude and exhibits mostly the fundamental mode; the effect of the *Karanai* excitation on the *Thoppi* response is more than the other way around.

In summary, the coupling has virtually no effect on the *Karanai* response but does have some impact on the *Thoppi* response (mostly for the first mode of vibration as seen from the FFT). This would suggest that the cavity only plays a minor role on the generation of harmonic musical notes.

## 4. CONCLUSION

From the investigations carried out using detailed finite element models, which minimizes the assumptions made regarding the vibro-acoustic coupling, it can be clearly stated that the *Karanai* harmonicity can be attributed to its own construction rather than to any contribution from the cavity due to a kettledrum effect. From the transient response simulations of the coupled acoustic-membranes system, it is clear that the cavity plays a minor role in the musical notes from the *Karanai* of the *mridangam*. Future work is focused on the prediction of the sound generated from both the uncoupled and coupled models.

## 5. REFERENCES

[1]     C. V. Raman and S. Kumar, 1920. Musical Drums with Harmonic Overtones, *Nature,* **104**, 500.

[2]     C. V. Raman, 1934. The Indian Musical Drums, Proc. *Indian Acad. Sci.-Sec. A,* **1**, 179-188. doi: 10.1007/BF03035705.

[3]     T. D. Rossing, 1992. Acoustics of Drums, *Phys. Today,* **45**, 40-47. doi: 10.1063/1.881333.

[4]     B. S. Ramakrishna and M. M. Sondhi, 1954. Vibrations of Indian Musical Drums Regarded as Composite Membranes, *J. Acoust. Soc. Am.,* **26**, 523-529. doi: 10.1121/1.1907369.

[5]     R. Ghosh, 1922. Note on Musical Drums, *Phys. Rev.,* **20**, 526-527.

[6]     S. S. Malu and A. Siddharthan, 2000. Acoustics of the Indian Drum, ArXiv e-prints, URL: https://arxiv.org/abs/math-ph/0001030.

[7]     J. Bridge and S. Keshavan, 2007. Vibration characteristics of a bi-density drumhead, *Mech. Res. Commun.,* **34**, 267-274.

[8]     G. Sathej, R. Adhikari, 2009. The Eigenspectra of Indian musical drums, *J. Acous. Soc. Am.,* **125**, 831-838.

[9]     T. Sarojini and A. Rahman, 1958. Variational Method for the Vibrations of the Indian Drums, *J. Acous. Soc. Am.,* **30**, 191-196.

[10]  H. P. W. Gottlieb, 1982. Effect of Air Cavity on the Annular Drum, *J. Acous. Soc. Am.,* **71**, 1025-1027.

[11]  R. S. Christian, R. E. Davis, A. Tubis, C. A. Anderson, R. I. Mills and T. D. Rossing, 1984. Effects of Air Loading on Timpani Membrane Vibrations, *J. Acous. Soc. Am.,* **76**, 1336-1345.

[12]  S. Tiwari and A. Gupta, 2017. Effects of Air Loading on the Acoustics of an Indian Musical Drum, *J. Acous. Soc. Am.,* **141**, 2611-2621.

[13]  R. B. Bhat, Acoustics of a Cavity Backed Membrane: The Indian Musical Drum, *J. Acous. Soc. Am.,* **90**, 1469-1474.

[14]  A. Gupta, V. Sharma and S. S. Gupta, 2019. Acoustics of bifacial Indian musical drums with composite membrane, *Proc. Int. Symp. Mus. Acous.,* Detmold, Germany, pp. 336-343.

[15]  F. Ihlenburg, 1998. Finite Element Analysis of Acoustic Scattering, *Springer-Verlag:* New York.

[16]  Simulia Abaqus, 2012. http://abaqus.software.polimi.it/v6.12/index.html.

[17]  S. Dahl, M. Grossbach and E. Altenmuller, 2011. Effect of dynamic level in drumming: Measurements of Striking Velocity, Force, and Sound level, *Forum Acusticum 2011,* Aalborg- Denmark, pp. 621-624.

# Acoustics of Mizhāvu

**Ankit Biswas, Saptarshi Paul, Vishal Sharma and Anurag Gupta**
*Department of Mechanical Engineering,*
*Indian Institute of Technology Kanpur, Kanpur-208 016, U.P.*
*e-mail: ag@iitk.ac.in*

## ABSTRACT

The vibro-acoustical nature of mizhāvu, a large pitcher-shaped monofacial membranophone with an indefinite pitch, is studied. A coupled structure-acoustics, Finite Element Method (FEM) based, methodology is developed and used for conducting the modal analysis of the drum consisting of a clamped membrane backed by an acoustic air cavity. The results of the FEM simulation are interpreted keeping in mind the recorded sound of the drum and the strokes that are used for playing the drum. The distinctive acoustical signature of mizhāvu is identified through a coupling of axisymmetric membrane modes with longitudinal pressure modes resulting in a rather rich spectrum of overtones. The effect of varying parametric values on the frequency spectrum of the drum is discussed and the acoustics of mizhāvu is compared with two large drums, the Indian nagāḍā and the western timpani.

## 1. INTRODUCTION

Mizhāvu[a] is a big-bellied pitcher-shaped monofacial membranophone[1,2]. It has a short narrow cylindrical neck over which a parchment is stretched and tied tightly using a rope. The pitcher is made of thin copper sheet which thickens towards the neck. The parchment is developed out of the outer calf skin and is noticeably thicker than the ones used in tablā, for instance. A tiny hole, also called the ear of the drum, is drilled through one side of the vessel at around halfway height



**Fig. 1.** Mizhāvu (notice the hole) with a closeup of the neck portion.

from the bottom, purposefully so as to improve the resonance[1]. A full mizhāvu, as well as a closeup of the neck region, is shown in Fig. 1. The drum is placed in front of the player within a cage (piñjara) of wooden slats such that its bottom remains away from the ground. Mizhāvu is played with hands and yields a loud metallic tone often described as thunderous. Unlike some other Indian drums, such as tablā, pakhāwaja, mradangam, and idakkā,[3-6] mizhāvu sound has no definite pitch.

---

[a] Mizhāvu is phonetically written as [mɪ.(a:v)]. The retroflex approximant [ɻ] is a trademark of Malayalam language. The *virama* at the end cancels the inherent vowel after the consonant *'v'* as per the schwa deletion rule.

---

Traditionally, mizhāvu has been used exclusively in the ritualistic Sanskrit theatre forms of Kerala such as kuṭiyaṭṭam, cākyarkuttu, and nāṅgyār kuttu[7,8]. kuṭiyaṭṭam is the most prominent survivor of the ancient Indian theatrical culture with several links to nātyaśastra. The theatre is performed within a highly formalized rectangular structure called kuṭṭambalam which has a square-shaped stage in addition to an auditorium. The stage is connected to the dressing room (nepathya), located behind it, with two narrow doors (one for entrance and the other for exit). Two mizhāvus are placed between these two doors in the backside of the stage, see Fig. 2. Besides mizhāvu, idakkā (hour-glass shaped drum), kuzhittāla (cymbal), śankha (conch), and two wind instruments (kompa and kuchal) are also present on stage (altogether constituting a pancavādya ensemble).



**Fig. 2.** Mizhāvu in performance during the kuṭiyaṭṭam festival at the
Natanakairali institute in Irinjala kuda, Kerala in the first week of January 2020.

Mizhāvu is played with an open palm using two basic strokes: thā, by hitting the middle of the membrane, and thom (or thu), by hittingnear the edge of the membrane[1]. These strokes are played with varying intensities to produce a structure of rhythmic beats ortālas. There are seven tālas: chempaṭa, tripuṭa, jhampa, dhruva, aṭanta, eka, and lakṣmī; these are used according to the situation, character, *etc.* (for instance, lakṣmī tāla is used to enact the jatāyudance piece from Rāmāyana).

The purpose of this article is to study and characterize the vibro-acoustical nature of mizhāvu. In Section 2, we report a brief analysis of the recording of mizhāvu sound. The recordings were conducted by one of the authors (SP) on the sidelines of the kuṭiyaṭṭam festival at the Natanakairali Institute in Irinjalakuda, Kerala, in early January 2020. These field studies provide us with the motivation for pursuing the simulation work in the following sections. In Section 3, we present an idealized mathematical model, and the associated variational formulation, for the finite element implementation of the structure-acoustic coupled problem. The results of the developed numerical methodology are presented and discussed in Section 4. The results are first justified in the light of frequency spectrums collected from the sound recordings and then studied under a variation in the parametric values of mouth diameter and membrane tension values. Subsequently, a simplified analytical model of the drum is discussed in order to understand the coupling between an axisymmetric membrane mode with the longitudinal acoustical modes. Towards the end, we briefly discuss the acoustics of nagāḍā and timpani and contrast them to that of mizhāvu. This is to emphasize the distinctiveness of mizhāvu in comparison to other big-bellied drums which also

---

[b] The phonemic representation of thā and thom strokes are /ṭ a:/ and /ṭ o:m/, respectively.

have a much larger mouth diameter than that of mizhāvu. Finally, we present some results which justify our assumption of ignoring the neck of the drum. The article is concluded in Section 5.

## 2. THE AUDIO RECORDINGS

The recordings were done using a mizhāvu which was 76 cm high, had a mouth with inner and outer diameter of 14 cm and 16 cm, respectively. The rim of the neck, which provided the boundary for the vibrating membrane, was therefore 1 cm thick.

The membrane was clamped at the outer edge of the rim. The maximum diameter of the pitcher was 52 cm. The hole on the side had a diameter of 9 mm and was located 48 cm above the bottom of the drum. The drum overall had an axisymmetric shape (modulo the hole on the side). The audio recordings were conducted using the Audio-Technica AT2020 USB cardioid condenser microphone. Several recordings were made (different drummers playing with different intensity) for each of the following cases: (i) basic strokes thā and thom with hole open, (ii) basic strokes thā and thom with hole closed, (iii) lakṣmī tāla on one drum, and (iv) free style playing using two mizhāvus. The recorded data is processed to generate spectrograms and frequency spectrum plots. The modal frequencies are identified from the dominant peaks appearing in the latter. Out of the several recordings for each of the case, mentioned above, we present results for one representative sample after noting little variation among all the available candidates. The dominant modal frequencies are summarized in Table 1. The spectrograms corresponding to thā and thom strokes, with hole open, are given in Fig. 3. The associated frequency spectrum plots are given in Fig. 4. The spectrum plots for the remaining four cases are collected in Figs. 5 and 6. The spectrograms for thā and thom strokes showed no perceptible difference when the hole was closed.

**Table 1.** Dominant natural frequencies (in Hz) for various playing styles.

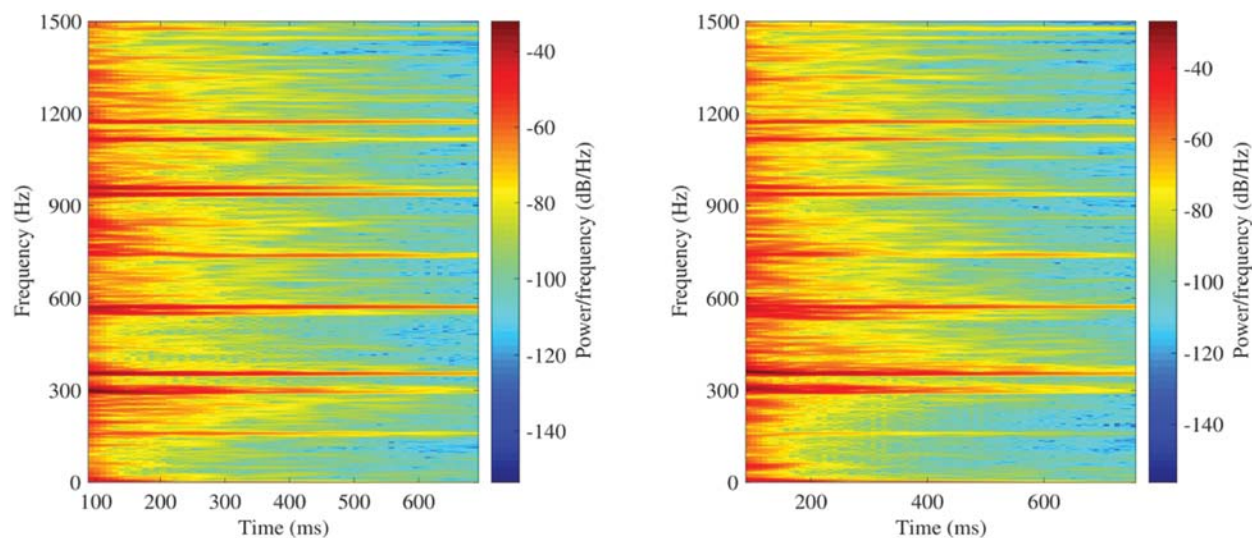| | |
|---|---|
| thā (with hole) | 293.9, 354.7, 571.3, 741, 834.7, 936.1, 957.6, 1116, 1173 |
| thom (with hole) | 305.6, 355.2, 572.3, 738.6, 935.7, 959.3, 1115, 1173 |
| thā (hole closed) | 296.2, 355, 571.6, 741.3, 844.4, 935.7, 959.2, 1116, 1173 |
| thom (hole closed) | 306.3, 361.3, 571.8, 936.7, 959.4, 1116 |
| lakṣmī tāla | 306.5, 358.5, 571.6, 743.8, 862.7, 938.5, 960.6, 1118, 1175 |
| two mizhāvus | 305.5, 359.7, 575.2, 617.8, 746.7, 853.1, 940, 961.6, 1118, 1175 |



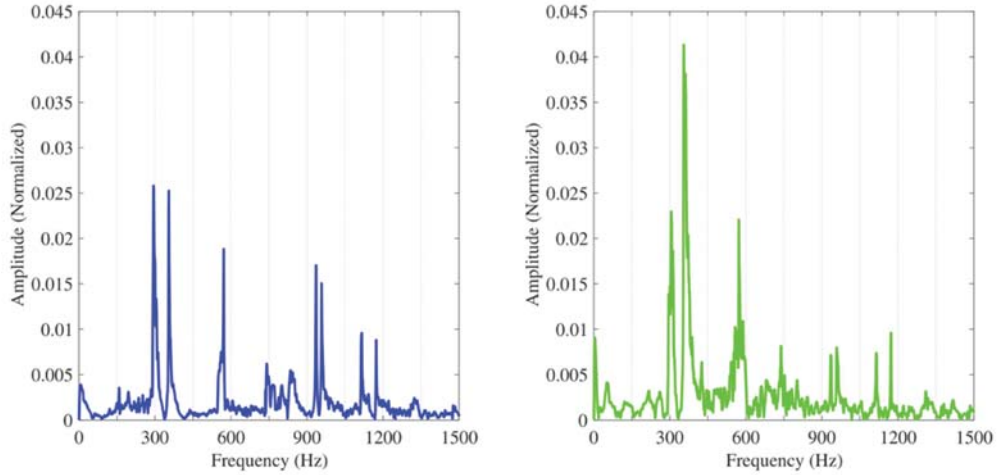**Fig. 3.** Spectrograms for thā and thom strokes with hole open.

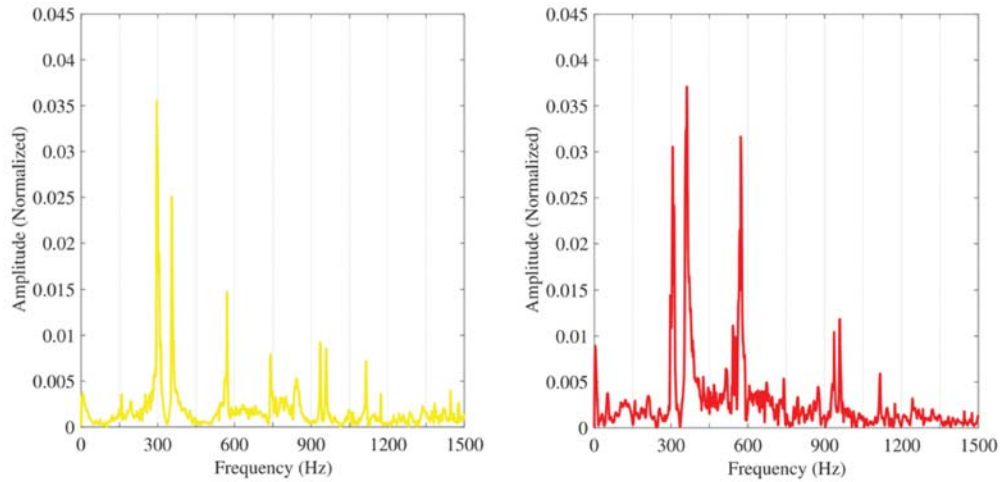**Fig. 4.** Frequency spectrum plots for thā and thom strokes with hole open.



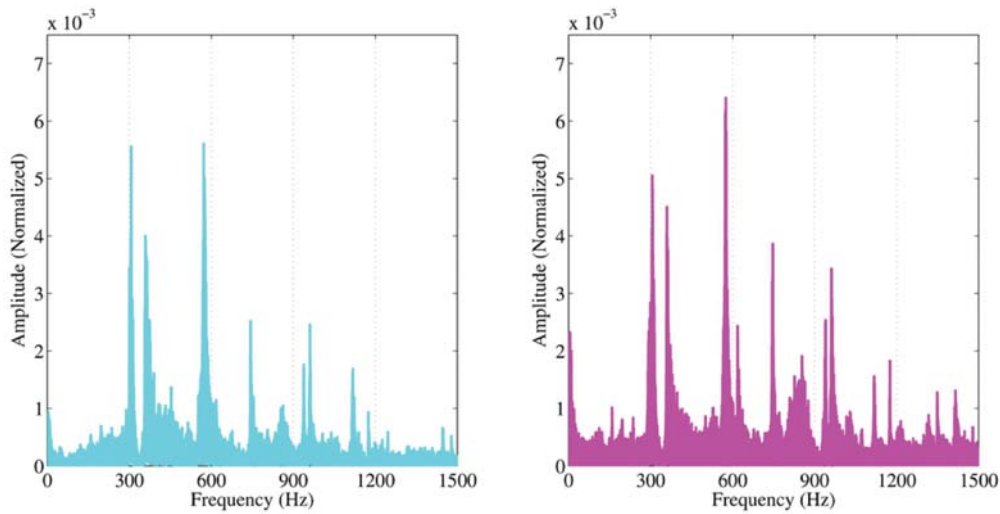**Fig. 5.** Frequency spectrum plots for thā and thom strokes with hole closed.



**Fig. 6.** Frequency spectrum plots for lakṣmī tāla and a pair of mizhāvus

Several observations are in order concerning these plots. First, recall that with the thā and thom strokes, the membrane is struck at the centre and close to the edge, respectively (both with an open palm). Therefore, we expect the spectrum of thā stroke to be dominated by the membrane modes with antinodes at the centre; all the 0m modes satisfy this. Here, and elsewhere, the mode shapes of circular membranes are denoted through the convention nm, where n indicates the number of nodal diameters and m the number of nodal circles[9]. The spectrum for the thom stroke will also include the other modes (the nm modes). This is evident from the spectrograms in Fig. 3, although the modes which sustain are identical in both the cases. Given that the strikes are made with an open palm (*i.e.*, a finite area over the small membrane), it is expected that the vibration modes are dominated by modes with 01 and 02 membrane modes (assuming that the higher membrane modes will be more damped). Even then, certain modes can dominate overall due to the resonance of specific membrane modes with the air cavity modes. Second, the hole in the drum shell appears to be in consequential as far as spectrograms and frequency spectrums are concerned. Its acoustical importance therefore remains inconclusive. Finally, there is a consistent pattern in peaks which can be noticed from all the spectrum plots. There are clear peaks close to 300 Hz, 600 Hz, 750 Hz, 900 Hz, and 1200 Hz, indicating semblance of a definite pitch with a fundamental of 150 Hz (the fundamental is discernible in the spectrograms). The peaks at 300 Hz, 900 Hz, and 1200 Hz always appear in pair. The difference in the frequencies of the pair are around 50 Hz, 20 Hz, and 50 Hz, respectively. The presence of these nearby peaks indicate a beat-like phenomena in mizhāvu sound. The splitting of frequencies can be a consequence of asymmetric tuning of the membrane, or due to asymmetry in the membrane density distribution, or asymmetry in the construction of the instrument; we do not explore any of these possibilities in this work. To summarize, the presence of air cavity in mizhāvu yields several dominant natural frequencies in close harmonic relationships in addition to appearance of beats due to pairs of nearby frequency values.

## 3. THE VIBRO-ACOUSTIC MODEL

The vibro-acoustic problem of monofacial drums can be described in terms of a system of coupled partial differential equations. These include the membrane vibration equation and the acoustic wave equation, the latter governing the internal pressure field of the cavity. The differential equations are supplemented with an appropriate set of initial and boundary conditions. We neglect both acoustic and structural damping and assume the walls of the cavity to be perfectly rigid. We also neglect the acoustic environment external to the drum. The cavity of the drum is closed in such a manner that the air inside the cavity is confined and the motion of the membrane changes the volume of the air in the cavity. This changes the pressure of the air confined in the cavity. The pressure of the confined air in turn generates a force on the membrane.

We consider an idealized model of mizhāvu, whose geometry is illustrated in Fig. 7. We assume the neck height (and width) of mizhāvu to be vanishingly small and the hole to be absent. The validity of the former assumption is discussed in Section 4.5 whereas the latter is justified in the preceding section on the basis of audio recordings. The membrane is clamped at the edge of the open face of the curved shell. The latter is assumed to be elastically rigid. In general, due to thickness of
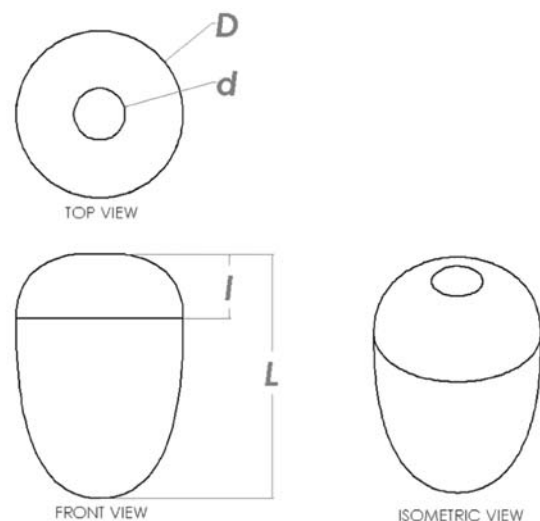


**Fig. 7.** An idealized model of mizhāvu shell used for FEM simulations; *d* represents diameter of the mouth, *D* the maximum diameter of the shell, *L* the height of the drum, and *l* the position (from top) of the maximum diameter.

the neck region, the membrane will wrap and unwrap over the finite rim, somewhat analogous to the behaviour of a vibrating string over the bridge in several Indian string instruments such as tānpurā and sitār[10]. The feature of a finite rim is also present in a large variety of Indian drums (*e.g.,* tablā, pakhāwaja, and idakkā) and it will be important to study its role in the vibro-acoustical behavior of these drums. However, in our idealized model, the rim is assumed to be sharp without any finite width. The density of the membrane is assumed to be uniform.

In formal terms, the cavity domain Λ is bounded by a rigid axisymmetric shell surface C and a circular membrane Σ of diameter d. The membrane, with a fixed edge S, is subjected to uniform tension *T* per unit length such that its transverse motion ū *(x, y, t)* is governed by the differential equation

$$\sigma \frac{\partial^2 \overline{u}}{\partial t^2} - T\Delta \overline{u} = \overline{p}, \tag{1}$$

where $\sigma$ is the uniform density (per unit area) of the membrane and the operator $\Delta$ represents the two-dimensional Laplacian. The acoustic pressure field $\overline{p}$ *(x, y, z, t)* is also an unknown variable. At radius $r = d/2$, $\overline{u} = 0$. The acoustic air cavity domain Λ is assumed to be filled with an inviscid fluid (air) whose pressure field is governed by the acoustic wave equation

$$\frac{\partial^2 \overline{p}}{\partial t^2} - c_p^2 \tilde{\Delta} \overline{p} = 0, \tag{2}$$

where $c_p$ is the speed of sound in the medium (air) and $\tilde{\Delta}$ is the three-dimensional Laplacian. The boundary conditions at the rigid wall surface *C* and at the membrane are given by $\partial \overline{p} / \partial n = 0$ and $\partial \overline{p} / \partial z = -\rho_a \overline{u}$, respectively, where $\rho_a$ is the density of air and *n* is the outward normal to the surface. The modal solutions

$$\overline{u} = u(x,y)e^{-i\omega t} \, and \, \overline{p} = p(x,y,z)e^{-i\omega t}, \tag{3}$$

where ω is the frequency, when substituted into Eqs. (1) and (2), respectively, yield

$$\omega^2 \sigma u + T\Delta u + p = 0 \tag{4}$$

for the membrane Σ, such that *u* = 0 at edge *S*, and

$$\omega^2 p + c_p^2 \tilde{\Delta} p = 0 \tag{5}$$

for the internal pressure field in the cavity Λ, such that $\partial \overline{p} / \partial n = 0$ on C and $\partial \overline{p} / \partial z = \omega^2 \rho_a u$ on Σ.

The preceding boundary-value-problem can be recast in terms of a variational principle. The solution of the problem, given in terms of smooth functions *u (x, y)* and *p(x, y, z)*, extremizes the variational functional $I(u, p) = I_1 + I_2$, where

$$I_1 = \int_\Sigma \frac{1}{2} T(\nabla u \bullet \nabla u)dA - \omega^2 \int_\Sigma \frac{1}{2} \sigma u^2 dA - \int_\Sigma pudA \, and \tag{6}$$

$$I_2 = \frac{1}{2\omega^2 \rho_a} \int_\Lambda \tilde{\nabla} p \bullet \tilde{\nabla} p dV - \frac{1}{2\rho_a c_p^2} \int_\Lambda p^2 dV \tag{7}$$

subjected to $\delta u = 0$ on S; the operators $\nabla$ and $\tilde{\nabla}$ represent the two-dimensional and the three-dimensional gradient; and · denotes the dot product. This variational principle forms the basis for our finite element procedure (implemented using Matlab) for the determination of modal frequencies and modal shapes. We choose four-node quadrilateral finite elements for discretizing the membrane and the rigid boundary *C* and eight-node hexahedral finite elements for discretizing the acoustic domain while ensuring that the membrane elements match well with acoustics domain elements at the nodes. The basis functions used for the former are {1, *x, y, xy*} whereas the basis functions used for the latter are {1, *x, y, z, xy, xz, yz, xyz*}.

The integration over domains is evaluated using the standard Gauss quadrature rule for polynomials. The efficacy of our code is tested by using it to verify the existing results for timpani and tablā as reported in the earlier literature[4,11,12]. The details, including those related to convergence and mesh refinement, are available elsewhere[13].

## 4. RESULTS AND DISCUSSION

The idealized shape of mizhāvu for simulation purposes is considered as given in Fig. 7. The curve generating the axisymmetric shape of the drum is drawn using a three-point spline interpolation. This is done in two parts, one from the mouth to the maximum diameter and the other from the maximum diameter to the bottom. The curves are chosen so as to mimic the shape of the actual drum. We fix the height of the drum as $L = 76$ cm, the maximum diameter of the shell as $D = 52$ cm, and the distance of the maximum diameter circle from top as $l = 28$ cm, all in accordance with the mizhāvu used for the audio recordings. The diameter d of the mouth however will be allowed to vary (between 14 cm and 16 cm). Besides $d$, we will also allow the membrane tension $T$ to take different values. The material parameters $\sigma = 0.5445$ kg/m$^2$ (areal density of the membrane), $\rho_a = 1.21$ kg/m$^3$ (volume density of air), and $c_p = 344$ m/s (speed of sound in air) will be fixed throughout. The areal density of the mizhāvu membrane is calculated from the samples collected during the field work. It should be noted that the density value is almost twice as much as that of tablā and timpani membranes.

### 4.1 The eigen-spectrum and mode shapes of the drum

In order to understand the frequency spectrum, as obtained from the audio recordings, we begin by fixing $d = 16$ cm and $T = 3500$ N/m. The effect of varying $d$ and $T$ values on the frequency spectrum will

**Table 2.** Mode shapes and natural frequencies of an ideal membrane (without air cavity) with $T = 3500$ N/m, $d = 16$ cm; the membrane displacements shown are in m.



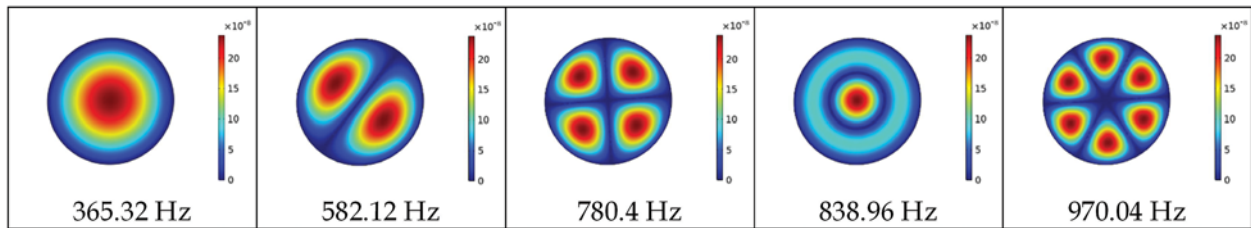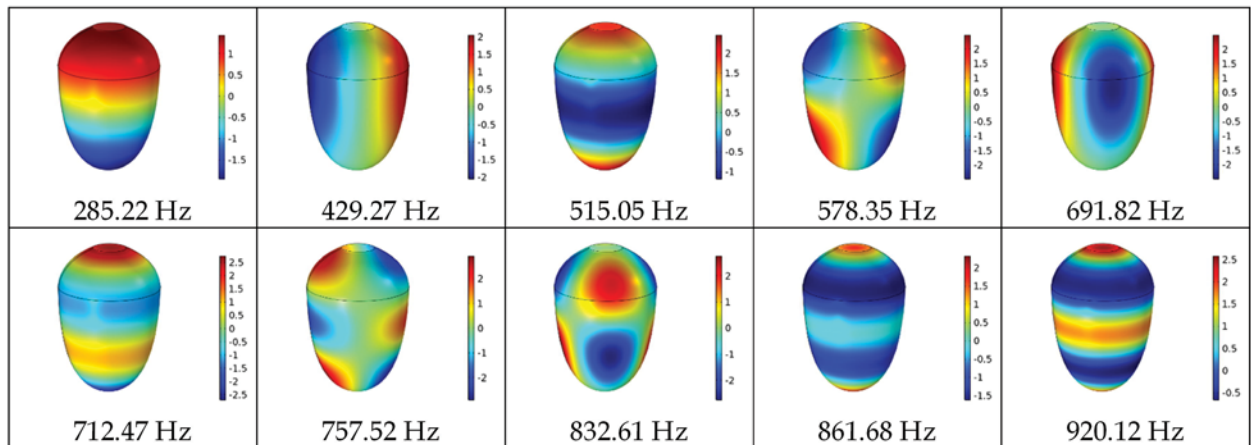| 365.32 Hz | 582.12 Hz | 780.4 Hz | 838.96 Hz | 970.04 Hz |

**Table 3.** Mode shapes and natural frequencies of the air cavity without a membrane closing the facing with $d = 16$ cm; the pressure values shown are in Pa.



| 285.22 Hz | 429.27 Hz | 515.05 Hz | 578.35 Hz | 691.82 Hz |
| 712.47 Hz | 757.52 Hz | 832.61 Hz | 861.68 Hz | 920.12 Hz |

be discussed in Section 4.2. To set the background, we look at the natural frequencies and mode shapes of the two building blocks of our drum taken separately, *i.e.*, an ideal membrane clamped at its edge, on one hand, and an air cavity in the shape of the drum but with a face not covered by the membrane, on the other. In the latter case, the air cavity is assumed to be surrounded by an acoustically hard boundary (*i.e.*, $\partial \overline{p} / \partial n = 0$ every where on the boundary). The pertinent results are collected in Tables 2 and 3, respectively. We recall from Section 2 that the strokes of mizhāvu playing will predominantly activate the 01 and 02 membrane modes (the axisymmetric modes) and consequently the longitudinal pressure modes (again axisymmetric) in the air cavity. With the considered parameters, these modes appear, respectively, at 365.32 Hz and 838.96 Hz for an isolated membrane, and at 285.22 Hz, 515.05 Hz, 712.47 Hz, 861.68 Hz, and 920.12 Hz for an isolated air cavity. The frequency values are close to the peaks observed in the spectrums from audio recordings.

A more complete picture is obtained when the frequency spectrum of the full drum (membrane and cavity coupled) is obtained. The results are given in Table 4. The relevant frequencies are those corresponding to the axisymmetric membrane modes. These are 279.46 Hz, 350.6 Hz, 520.42 Hz, 716 Hz, corresponding to the 01 membrane mode, and 829.39 Hz, 865.09 Hz, 926.23 Hz, corresponding to the 02 membrane mode. The acoustic mode shapes which accompany these frequencies are all longitudinal and axisymmetric, see Table 4. These frequency values are in reasonable agreement with the frequency spectrum obtained from the audio recordings of the thā stroke where the first seven frequency peaks were observed at 293.9 Hz, 354.7 Hz, 571.3 Hz, 741 Hz, 834.7 Hz, 936.1 Hz, 957.6 Hz, see Table 1, first row. While comparing these values we should remember that we have ignored the effect of the acoustic environment external to the drum and have neglected the finiteness of the rim, among other idealizations in terms of geometry and material properties.

The acoustical nature of mizhāvu is distinct from that of both tablā and timpani. The tablā acoustics is dominated by the vibrations of the non-uniform membrane (which yields a definite pitch) with the air cavity playing a leading role in dampening out the unwanted modes. In timpani acoustics, the acoustic cavity exerts a sufficient pressure load on the membrane so as to bring slight (but important) changes in the membrane frequency values. The mizhāvu acoustics is dominated by the longitudinal (axisymmetric) pressure modes multitude of which are coupled with the axisymmetric membrane modes. In fact, in all but a few cases, the pressure modes generate the vibration pattern in the membrane (as if it is a forced vibration of the membrane due to acoustic pressure). Unlike both tablā and timpani, several distinct modes appear each with 01 and 02 membrane modes (see also Section 4.4). Consequently, even the sound generated by exciting only the first one or two axisymmetric membrane modes (by striking the drum membrane at the center, as in the thā stroke) yields rich overtones with a somewhat distinctive pitch.

## 4.2 Effect of varying membrane diameter and tension

We now investigate how the spectrum changes when we change the mouth diameter and tension in the membrane, while keeping other parameters fixed (as mentioned above). The natural frequency values, appended with the corresponding membrane mode shape identifiers, are collected in Table 5. The acoustic modes are not mentioned for the sake of brevity and because they are of the kind plotted in Table 4. The membrane modes can be identified with the numbers written in the nm format in a smaller font next to the frequency values. For instance, $277_{01}$ indicates that the frequency 277 Hz (rounded off to the nearest integer) is associated with a mode shape having 01 membrane mode (in addition to some pressure mode). Wherever the mode shape was unclear, it is indicated with a $U$ next to the frequency value. Some columns are shorter than others because the membrane mode shapes are no longer discernible. We first note the trend in the frequency spectrum change as we modify the diameter of the mouth from $d = 14$ cm to 15 cm and then 16 cm, all for a fixed tension value. The frequencies are, in general, seen to decrease with increasing $d$, sometime staying more or less constant but sometimes changing drastically. Frequently, particularly for higher frequencies, the order of mode shapes is modified and, in some cases, new membrane modes replace existing ones. These observations remain invariant for all the seven membrane tension values between 2000 N/m and 5000 N/m considered in Table 5. We also note the change in the

**Table 4.** Mode shapes and natural frequencies (in Hz) of an idealized mizhāvu with $T = 3500$ N/m and $d = 16$ cm. The membrane and air cavity modes shapes are shown separately for clarity. The membrane displacements are in m and pressure in Pa.

| Natural Frequency (Hz) | Membrane Mode | Air Cavity Mode | Natural Frequency (Hz) | Membrane Mode | Air Cavity Mode |
|---|---|---|---|---|---|
| 279.46 | | | 768.38 | | |
| 350.6 | | | 829.39 | | |
| 429.3 | | | 832.72 | | |
| 520.42 | | | 865.09 | | |
| 561.8 | | | 926.23 | | |
| 581.46 | | | 935.01 | | |
| 691.78 | | | 937.39 | | |
| 716.23 | | | 967.88 | | |
| 758.21 | | | 997.69 | | |

**Table 5.** Natural frequencies (in Hz, rounded to closest integers) for various mouth diameters ($d$ in cm) and tension values. Each frequency value is appended (in a smaller font) with the associated membrane mode designation. For instance, $277_{01}$ indicates that the frequency 277 Hz is associated with a mode shape having 01 membrane mode (in addition to some pressure mode). The notation $U$ appearing next to some values indicate that the corresponding mode shape was unclear.

| T=2000 d=14 | T=2000 d=15 | T=2000 d=16 | T=2500 d=14 | T=2500 d=15 | T=2500 d=16 | T=3000 d=14 | T=3000 d=15 | T=3000 d=16 | T=3500 d=14 | T=3500 d=15 | T=3500 d=16 | T=4000 d=14 | T=4000 d=15 | T=4000 d=16 | T=4500 d=14 | T=4500 d=15 | T=4500 d=16 | T=5000 d=14 | T=5000 d=15 | T=5000 d=16 |
|---|---|---|---|---|---|---|---|---|---|---|---|---|---|---|---|---|---|---|---|---|
| $277_{01}$ | $269_{01}$ | $251_{01}$ | $281_{01}$ | $277_{01}$ | $269_{01}$ | $282_{01}$ | $278_{01}$ | $276_{01}$ | $282_{01}$ | $279_{01}$ | $279_{01}$ | $283_{01}$ | $280_{01}$ | $281_{01}$ | $283_{01}$ | $280_{01}$ | $281_{01}$ | $283_{01}$ | $281_{01}$ | $282_{01}$ |
| $323_{01}$ | $307_{01}$ | $298_{01}$ | $356_{01}$ | $335_{01}$ | $310_{01}$ | $387_{01}$ | $362_{01}$ | $329_{01}$ | $415_{01}$ | $389_{01}$ | $350_{01}$ | $419_{11}$ | $413_{01}$ | $371_{01}$ | $419_{11}$ | $417_{11}$ | $391_{01}$ | $419_{11}$ | $417_{11}$ | $410_{01}$ |
| $419_{11}$ | $418_{11}$ | $423_{11}$ | $419_{11}$ | $418_{11}$ | $429_{11}$ | $419_{11}$ | $417_{11}$ | $429_{11}$ | $419_{11}$ | $417_{11}$ | $429_{11}$ | $441_{01}$ | $417_{11}$ | $429_{11}$ | $464_{01}$ | $436_{01}$ | $429_{11}$ | $482_{01}$ | $456_{01}$ | $429_{11}$ |
| $515_{11}$ | $480_{11}$ | $433_{11}$ | $519_{01}$ | $516_{01}$ | $478_{11}$ | $519_{01}$ | $517_{01}$ | $519_{01}$ | $521_{01}$ | $517_{01}$ | $520_{01}$ | $523_{01}$ | $519_{01}$ | $521_{01}$ | $526_{01}$ | $520_{01}$ | $522_{01}$ | $532_{01}$ | $523_{01}$ | $523_{01}$ |
| $518_{01}$ | $516_{01}$ | $518_{01}$ | $559_{11}$ | $535_{11}$ | $519_{01}$ | $560_{11}$ | $555_{11}$ | $522_{11}$ | $560_{11}$ | $555_{11}$ | $561_{11}$ | $560_{11}$ | $556_{11}$ | $576_{11}$ | $560_{11}$ | $556_{11}$ | $577_{11}$ | $560_{11}$ | $556_{11}$ | $577_{11}$ |
| $561_{11}$ | $555_{11}$ | $579_{11}$ | $578_{11}$ | $558_{11}$ | $579_{11}$ | $630_{11}$ | $588_{11}$ | $576_{11}$ | $677_{21}$ | $634_{11}$ | $581_{11}$ | $677_{21}$ | $675_{21}$ | $605_{11}$ | $677_{21}$ | $675_{21}$ | $640_{11}$ | $677_{21}$ | $675_{21}$ | $673_{11}$ |
| $677_{21}$ | $653_{21}$ | $581_{21}$ | $678_{21}$ | $676_{21}$ | $650_{21}$ | $677_{21}$ | $675_{21}$ | $691_{21}$ | $680_{11}$ | $675_{11}$ | $691_{21}$ | $720_{01}$ | $677_{11}$ | $691_{21}$ | $720_{01}$ | $719_{01}$ | $691_{21}$ | $721_{01}$ | $719_{01}$ | $691_{21}$ |
| $699_{21}$ | $676_{21}$ | $626_{02}$ | $718_{01}$ | $715_{02}$ | $692_{02}$ | $680_{11}$ | $717U$ | $711_{21}$ | $719_{01}$ | $717_{01}$ | $716_{01}$ | $724_{11}$ | $718_{01}$ | $717_{01}$ | $739_{11}$ | $738_{11}$ | $718_{01}$ | $740_{11}$ | $732_{11}$ | $718_{01}$ |
| $714_{02}$ | $694_{02}$ | $692_{21}$ | $741_{11}$ | $729_{21}$ | $728_{02}$ | $741_{11}$ | $735_{11}$ | $758_{11}$ | $742_{11}$ | $735_{11}$ | $758_{11}$ | $744_{11}$ | $736_{11}$ | $758_{11}$ | $774_{11}$ | $801_{21}$ | $758_{11}$ | $806_{21}$ | $760_{11}$ | $759_{11}$ |
| $741_{11}$ | $728_{02}$ | $720U$ | $782_{21}$ | $735_{11}$ | $757_{11}$ | $806_{21}$ | $798_{21}$ | $773_{02}$ | $806_{21}$ | $801_{21}$ | $768_{21}$ | $806_{21}$ | $801_{21}$ | $802_{11}$ | $806_{21}$ | $845_{01}$ | $832_{21}$ | $814_{11}$ | $801_{21}$ | $832_{21}$ |
| $760_{02}$ | $735_{11}$ | $732_{31}$ | $806_{21}$ | $788_{02}$ | $818_{31}$ | $848_{02}$ | $802_{21}$ | $832_{21}$ | $848_{01}$ | $845_{01}$ | $829_{02}$ | $849_{01}$ | $845_{01}$ | $833_{21}$ | $849_{01}$ | $908_{01}$ | $862_{01}$ | $849_{01}$ | $845_{01}$ | $862_{01}$ |
| $806_{21}$ | $801_{21}$ | $757_{12}$ | $839_{02}$ | $801_{21}$ | $832_{21}$ | $856_{21}$ | $843U$ | $863U$ | $909_{02}$ | $862_{21}$ | $832_{21}$ | $911_{01}$ | $907_{02}$ | $860_{02}$ | $911_{01}$ | $917_{31}$ | $871_{21}$ | $912_{01}$ | $909_{01}$ | $917_{21}$ |
| $849_{02}$ | $822_{31}$ | $808_{12}$ | $852_{02}$ | $846_{02}$ | $863U$ | $903_{02}$ | $862_{02}$ | $896_{31}$ | $919_{31}$ | $902_{02}$ | $865_{02}$ | $919_{31}$ | $917_{31}$ | $886_{02}$ | $919_{31}$ | $919_{11}$ | $915_{02}$ | $919_{31}$ | $917_{31}$ | $920U$ |
| $880_{31}$ | $845U$ | $832_{21}$ | $915U$ | $911U$ | $900_{12}$ | $919U$ | $914_{02}$ | $925U$ | $925_{31}$ | $917_{31}$ | $926_{02}$ | $925_{11}$ | $919_{11}$ | $929_{02}$ | $925_{11}$ | $960_{02}$ | $935_{11}$ | $926_{11}$ | $920_{11}$ | $935_{11}$ |
| $913_{02}$ | $903_{12}$ |  | $919_{31}$ | $917_{31}$ |  | $925_{11}$ | $917U$ | $934_{12}$ | $968_{21}$ | $919_{11}$ | $935_{11}$ | $968_{21}$ | $922_{21}$ | $935_{11}$ | $968_{21}$ | $978_{21}$ | $937_{31}$ | $968_{21}$ | $961_{21}$ | $937_{31}$ |
| $920_{31}$ | $910U$ |  | $925_{11}$ | $919_{12}$ |  | $935_{02}$ | $919_{11}$ | $937_{31}$ | $1000_{02}$ | $940_{02}$ | $937_{31}$ | $989_{21}$ | $961_{21}$ | $937_{31}$ |  | $995_{02}$ | $951_{02}$ | $1002_{02}$ | $995_{02}$ | $995_{02}$ |
| $924_{12}$ | $917_{31}$ |  | $968_{21}$ | $961_{21}$ |  | $968_{21}$ | $961_{21}$ | $989_{12}$ | $1003_{02}$ | $961_{21}$ | $967_{31}$ | $1002_{02}$ | $995_{02}$ | $997_{21}$ |  |  |  |  |  |  |
|  |  |  |  |  |  | $1002_{02}$ | $995U$ | $1030_{01}$ | $1042_{31}$ | $995_{02}$ | $1030_{01}$ |  | $998_{02}$ | $1030_{01}$ |  |  |  |  |  |  |

spectrum for a fixed diameter but varying tension in the membrane. The frequency values generally increase with an increasing tension, but there are multiple instances when they remain invariant. The latter will clearly occur whenever the mode is dominated by the acoustic cavity and the membrane vibration has little overall influence. The axisymmetric modal frequencies, agreeable with mizhāvu, are obtained at higher tension values for lower mouth diameters and vice versa.

To see how one (axisymmetric) membrane mode can couple with several longitudinal acoustic cavity modes, we consider a simple model of the membrane acoustic interaction. We assume the membrane to vibrate only in its *01* mode and allow only one-dimensional longitudinal pressure variations in the cavity. As a result, we have a simple harmonic oscillator (mass m and stiffness $k$) coupled with a one-dimensional acoustic tube filled with air (piston-like arrangement), see Fig. 8. The length of the air column is taken as $H$, and we retain the values of the density of air $\rho_a$ and the speed of sound in air $c_p$ as before. The value of $k$ is obtain from the natural frequency of the 01 mode of an ideal (no cavity) circular membrane clamped at its edge. The mass $m$ is taken to be the mass of the membrane. The area of cross-section of the tube, $A$, is taken to be the area of the membrane (*i.e.*, $\pi d^2/4$). The displacement of mass m is denoted as *w(t)* and the pressure field in the tube as *q(z, t)*.



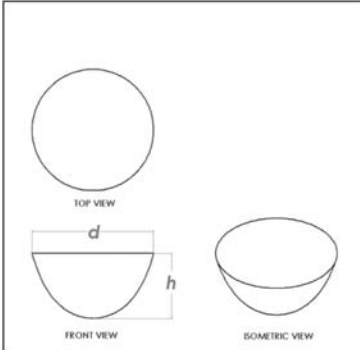**Fig. 8.** A simple model to illustrate coupling of one membrane mode with axisymmetric cavity modes.

The governing equations include $m\ddot{w} + kw = q(0,t)A$ for the motion of mass $m$, $\partial^2 q / \partial t^2 = c_p^2 \partial^2 q / \partial z^2$ for the cavity acoustics, and the boundary conditions $\partial q / \partial z = -\rho_a \ddot{w}$ at $z = 0$ and $\partial q / \partial z = 0$ at $z = H$. As usual, the solutions areassumed to be of the form $w(t) = w_0 e^{-i\omega t}$ and $q(z,t) = f(z) e^{-i\omega t}$. The simplified equations are solved by $f(z) = B_1 \sin(\omega z / c_p) + B_2 \cos(\omega z / c_p)$, where the constant coefficients $B_1$ and $B_2$ are such that $B_1 / B_2 = \tan(\omega H / c_p) = A \rho_a c_p \omega / (k - m\omega^2)$. The second equality in the last expression can be used to calculate the natural frequencies and the first for determining the corresponding mode shapes.

To obtain quantitative results, we fix $d$ = 0.16 m, hence A = 0.02 m², H = 0.76 m, and $T$ = 3500 N/m. We take $m = \sigma A$ and $k = m\omega_0^2$, where $\omega_0 = 2.405\sqrt{T/\sigma} / (d/2)$. The natural frequencies, of values less than 1000 Hz, are calculated as 251.5 Hz, 659.4 Hz, 893.3 Hz. These correspond to longitudinal pressure modes in the tube with one, three, and four nodes, respectively. Although it is not wise to draw a direct comparison with the numerical results of Section 4.1 (where we had considered a drum of same diameter, same height, and same tension), the present calculations lead to values which are comparable with a subset of those obtained for mizhāvu. The simplified model otherwise is limited in its scope and should be used with care.

### 4.4 Nagāḍā and timpani

It is relevant to compare mizhāvu acoustics with some other big-bellied drums such as the Indian nagāḍā and the western timpani. Both have a membrane stretched over the mouth of a kettle, see Table 6 for a representative shape and dimensions. The former is typically twice as big as the latter. Both of these however have a significantly larger mouth diameters when compared to mizhāvu. The acoustics of timpani has been well studied[9,11,12]. In Table 6, we report natural frequency values for these drums for two typical tension values. The density value $\sigma$ = 0.5445 kg/m² corresponds to that of mizhāvu and $\sigma$ = 0.2650 kg/m² to that of timpani membrane. The low frequency values of nagāḍā renders the drum useful to be heard over large distances, as has been historically the purpose of such drums. In any case, we note that unlike

**Table 6.** nagāḍā and timpani. The natural frequency (in Hz, rounded to closest integer) spectrum for various tension *(T)* and membrane density (σ, in kg/m²) values. The associated membrane modes are indicated in a smaller font. For instance, $55_{01}$ indicates that the frequency 55 Hz corresponds to a mode shape with 01 membrane mode (in addition to some pressure mode).
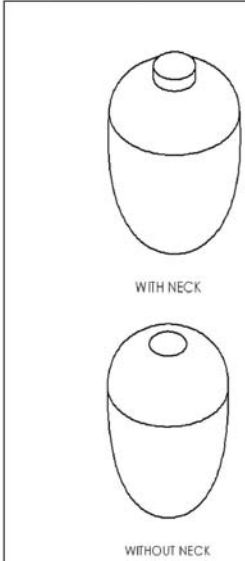
| | nagāḍā (d=1.4 m, h=0.75 m) | | | | timpani (d=0.656 m, h=0.414 m) | |
|---|---|---|---|---|---|---|
| | =3000 N/m | | =3500 N/m | | =3500 N/m | |
| | =0.2650 | =0.5445 | =0.2650 | =0.5445 | =0.2650 | =0.5445 |
| | $55_{11}$ | $47_{11}$ | $60_{11}$ | $51_{11}$ | $158_{11}$ | $127_{11}$ |
| | $87_{01}$ | $69_{01}$ | $92_{01}$ | $74_{01}$ | $184_{01}$ | $140_{01}$ |
| | $88_{21}$ | $71_{21}$ | $94_{21}$ | $77_{21}$ | $237_{21}$ | $181_{21}$ |
| | $118_{31}$ | $93_{31}$ | $127_{31}$ | $100_{31}$ | $272_{02}$ | $207_{02}$ |
| | $128_{02}$ | $101_{12}$ | $132_{02}$ | $106_{02}$ | $309_{31}$ | $231_{31}$ |
| | $129_{12}$ | $103_{02}$ | $138_{12}$ | $109_{12}$ | $330_{12}$ | $251_{12}$ |
| | $147_{41}$ | $114_{41}$ | $158_{41}$ | $123_{41}$ | $378_{41}$ | $279_{41}$ |
| | $164_{22}$ | $126_{22}$ | $177_{22}$ | $136_{22}$ | | |

mizhāvu, there are no repeated membrane modes in either of these drums. Therefore, if one is to activate only the axisymmetric membrane modes (by striking at the center of the drum), then only one frequency will be heard corresponding to each membrane mode. In this way, mizhāvu distinguishes itself from some other big-bellied drums. Consequently, we can conjecture that the uniqueness of mizhāvu sound is due to its large pot-like belly covered with a membrane over a small mouth. The authors were not able to locate any pitcher-type drums of this sort in other musical cultures.

## 4.5 The relevance of neck height

In our idealization of mizhāvu, in Section 3, we had ignored height of the neck altogether. We now justify our assumption by reporting natural frequency values for a mizhāvu, with and without neck, for

**Table 7.** Effect of mizhāvu neck. The natural frequency (in Hz, rounded to closest integer) spectrum for two tension *(T)* values with, and without, the neck. The associated membrane modes are indicated in a smaller font (*U* represents an unclear mode shape). For instance, $280_{01}$ indicates that the frequency 280 Hz corresponds to a mode shape with 01 membrane mode (in addition to some pressure mode). The mouth diameter is d=16 cm.

| | T = 3000 N/m | | T = 3500 N/m | |
|---|---|---|---|---|
| | *With Neck* | *Without Neck* | *With Neck* | *Without Neck* |
| | $280_{01}$ | $276_{01}$ | $286_{01}$ | $279_{01}$ |
| | $326_{01}$ | $329_{01}$ | $345_{01}$ | $350_{01}$ |
| | $414_{11}$ | $429_{11}$ | $414_{11}$ | $429_{11}$ |
| | $519_{11}$ | $519_{01}$ | $537_{01}$ | $520_{01}$ |
| | $536_{01}$ | $522_{11}$ | $557_{11}$ | $561_{11}$ |
| | $562_{11}$ | $579_{11}$ | $565_{11}$ | $581_{11}$ |
| | $669_{21}$ | $691_{21}$ | $669_{21}$ | $691_{21}$ |
| | $709_{21}$ | $711_{21}$ | $719_{01}$ | $716_{01}$ |
| | $711_{U}$ | $713_{U}$ | $755_{11}$ | $758_{11}$ |
| | $755_{11}$ | $758_{11}$ | $766_{21}$ | $768_{21}$ |
| | $774_{02}$ | $773_{02}$ | $800_{21}$ | $829_{02}$ |
| | $800_{21}$ | $832_{21}$ | $820_{02}$ | $832_{21}$ |
| | $840_{02}$ | $863_{02}$ | $843_{02}$ | $865_{02}$ |
| | $894_{31}$ | $896_{31}$ | $904_{02}$ | $926_{02}$ |
| | $900_{U}$ | $925_{U}$ | $909_{31}$ | $935_{11}$ |
| | $909_{31}$ | $933_{12}$ | | |

two tension values, see Table 7. The shape of the neck is illustrated there with. The height of the neck is taken as 5 cm. It is clear that inclusion of the neck has a limited, possibly negligible, influence on the frequency values. The neck, however, is essential for tying the membrane around the mouth using ropes, see Figure 1.

## 5.  CONCLUSION

We have discussed the vibro-acoustical character of mizhāvu, which is a big-bellied, but small mouthed, drum used extensively as a primary accompaniment in the Sanskrit theatre forms of Kerala. The drum is played with a limited number of distinct strokes, particularly those which excite the axisymmetric membrane modes 01 and 02. Each of these membrane modes appear with a large number of longitudinal pressure acoustic modes. Hence, even by striking the membrane at the center one can hear an overtone rich sound which has a near harmonic character. Such a drum is indeed unique and has no equal among other known drums in the world culture. We have argued our viewpoint by providing a brief comparison with two kettledrums but further comparisons should be taken up with respect to big-bellied monofacial drums from Africa and Japan. On the other hand, the simulation methodology is being presently extended to include external acoustic environment so that more realistic results can be obtained. Such a framework will also help us understand the reception of mizhāvu sound by the performers and the audience present in the formalized theatre environment within which it is usually performed.

## 6.  ACKNOWLEDGEMENTS

## 7.  REFERENCES

[1]   L. S. Rajagopalan, 1974. The Mizhavu, *J. Madras Music Acad.,* **XLV**, 109-117.

[2]   K. S. Kothari, 1968. Indian Folk Musical Instruments, *Sangeet Natak Akademi.*

[3]   C. V. Raman, 1934. The Indian musical drums, *Proc. Indian Acad. Sci.,* **A1**, 179-188.

[4]   S. Tiwari and A. Gupta, 2017. Effects of air loading on the acoustics of an Indian musical drum, *J. Acoust. Soc. Am.,* **141**, 2611-2621.

[5]   K. Jose, A. Chatterjee and A. Gupta, 2018. Acoustics of Idakkā: An Indian snaredrum with definite pitch, *J. Acoust. Soc. Am.,* **143**, 3184-3194.

[6]   A. Gupta, V. Sharma and S. S. Gupta, 2019. Acoustics of bifacial Indian musical drums with composite membrane, in *Proceedings of International Symposium on Music Acoustics, Detmold, Germany*, pp. 336-343.

[7]   K. Vatsyayan, 2005. Traditional Indian Theatre, *National Book Trust.*

[8]   K. Bindu and K. S. Vijayan, 2019. Contemporary Types of Ritualistic South Indian Mizhavu Percussion Ensembles in Kerala, In *Traditional Music and Dance in Contemporary Culture(s), J. Ambrózová and B. Garaj (Eds.), Nitra: Constantine the Philosopher University*, pp. 28-41.

[9]   N. H. Fletcher and T. D. Rossing, 1998.  The Physics of Musical Instruments, *Springer.*

[10]   R. Pisharody and A. Gupta, 2018. Experimental investigations of tānpurā acoustics, *Acta Acust. united Ac.,* **104**, 542-545.

[11]   R. S. Christian, R. E. Davis, A. Tubis, C. A. Anderson, R. I. Mills and T. D. Rossing, 1984. Effect of air loading on timpani membrane vibrations, *J. Acoust. Soc. Am.,* **76**, 1336-1345.

[12]  L. Rhaouti, A. Chaigne and P. Joly, 1999. Time-domain modeling and numerical simulation of a kettledrum, *J. Acoust. Soc. Am.,* **105**, 3545-3562.

[13]  V. Sharma, 2018. MS Thesis, IIT Kanpur, *Vibroacoustics of bifacial Indian musical drums.*

# Evaluation of porous materials for combined thermal and acoustic insulation

**Sripriya Ramamoorthy and Shankar Krishnan**

*Department of Mechanical Engineering,*
*Indian Institute of Technology Bombay, Powai, Mumbai-400 076, India*
*e-mail: ramamoor@iitb.ac.in, kshankar@iitb.ac.in*

## ABSTRACT

The necessity for thermal comfort of residents is typically considered upfront in building design by thermally insulating the interior of the building from the extremities in temperature in the external environment. With an increasing trend in industrialization, especially in developing countries, the necessity for noise isolation is also being recognized. For example, high-rise buildings in metropolitan cities utilize noise-isolating windows to reduce the nuisance from city noise bothering the building residents. This raises a new question whether it is possible to identify or design materials for combined thermal and acoustic insulation in buildings. Thermal-acoustic insulation requirements are also an essential consideration in isolating automobile engines from the passenger compartment. To address these concerns, a common platform to perform combined thermal and acoustic evaluation of porous and other materials is laid out in this study. In addition to existing materials, a designed periodic porous material for combined thermal-acoustic insulation is also explored. From the materials studied, it is observed that the combined thermal-acoustic insulation is better for porous materials with smaller pore-size and larger thickness, and with an optimum porosity owing to its contrasting effects on radiation vs. conduction contribution to the overall thermal conductivity.

## 1. INTRODUCTION

Although very thick materials with relatively low thermal conductivity may provide thermal and acoustic insulation, such materials may not practically fit many applications. Even in buildings, the thickness of the walls cannot be too high. Lightweight materials are sought-after in buildings because they aid in fast construction and less 'embodied energy' (Lee, Trcka, & Hensen, 2011). This restriction is more stringent in a car where a lightweight material is needed to separate the engine compartment and exhaust gases from the passenger compartment (Ohadi & Qi, 2005).

When lightweight materials with high strength to weight ratio and both thermal and acoustic insulation properties are required, porous materials could be employed. For example, polyurethane foam (PUF) and melamine foam are both currently used for combined thermal-acoustic insulation in automotive applications. Melamine is open-cell foam, whereas PUF is, in general, a closed-cell foam. PUF is also widely used for thermal-acoustic insulation in buildings. Although economical, PUF is extremely flammable and

hence cannot be used in public places where fire could be a risk. On the other hand, melamine is more expensive but has better fire safety.

Polymeric foams are also used for thermal insulation applications. The modest proportion of solid material in the foam and the consequent large volume fraction of gas results in an overall reduction in the polymeric foam's resultant thermal conductivity because of the much lower thermal conductivity of gas than the solid polymer. For buildings and automotive applications, air is the gas often used. The air thermal conductivity is at least an order-of-magnitude lower than the polymer thermal conductivity ($k_{polymer}$ ~ $0.3 \pm 0.1$ W/mK). Closed-cell polymeric foams filled with high molecular weight gases have the lowest conductivity of any conventional insulation, excluding those containing vacuums. However, this work focuses on open-cell polymeric foam insulations.

The general conviction is that thermal and acoustic insulation are correlated. This view was questioned in a recent article (Nurzyński, 2015), which shows that the two types of insulations may be partly correlated for some existing building insulation materials but not in others. This study aims to develop a method for evaluating the combined thermal and acoustic insulation performances of porous materials. Such a study will guide making design decisions based on quantitative rather than subjective evaluation. As an example of the proposed evaluation methodology, the current study considers two types of porous materials: open-cell melamine foam uncompressed as well as compressed and a designed periodic foam.

## 2. METHODS AND MATERIALS

### 2.1 *Identifying design requirements and arriving at specifications*

For the best acoustic insulation, the transmission loss (TL) should be as high as possible. The thermal resistance, defined as driving temperature difference divided by the heat transfer rate, should be as high as possible for the best thermal insulation. However, there could be other design limitations in an application, such as weight or cost. Suppose the engine noise in a car is 120 dBSPL, and that needs to be reduced to 60 dBSPL in the passenger compartment. Then, the TL required is 60 dB. Increasing TL beyond this requirement may not be useful because the background noise in the passenger compartment may be about 50-60 dB SPL from other sources. The insulation material itself should not deteriorate the engine performance by inflicting high back-pressure.The thermal requirement inside the passenger compartment is about 25°C, whereas in the car underhood near the internal combustion engine, the temperatures can be a few hundred degrees. Therefore, in this example, the specification could be as follows: 60 dB transmission loss and insulation of the surrounding exposed to this high temperature via heat loss prevention.

### 2.2 *Predicting the thermal resistance of porous materials*

Heat transfer in open-cell foams takes place by conduction through the solid cell struts, conduction through the air occupying the cell interior, and radiation throughout the foam. The apparent thermal conductivity of the foam material can be written as a superposition of each mechanism (Glicksman, 1994):

$$k_{eff} = k_{conduction,gas} + k_{conduction,solid} + k_{radiation} \tag{1}$$

It is assumed in Eq.(1) that the thermal radiation acts independently of the other heat transfer mechanisms. The effective stagnant thermal conductivity of solid and gas can be expressed as (Glicksman, 1994):

$$k_{eff,cond} = \phi k_{gas}(T) + \frac{(1-\phi)}{3} k_{solid} \tag{2}$$

In Eq. (2), $\phi$ is the porosity (or void fraction), $k_{gas}$ is gas thermal conductivity, and $k_{solid}$ is solid (polymer) thermal conductivity. Using the diffusion approximation, the radiative contribution to the foam conductivity (in optically thick media) is given by (Glicksman, 1994):

$$k_{radiation} = \frac{16}{3}\sigma\frac{T^3}{Kext} \tag{3}$$

Here, $\sigma$ = 5.67 × 10⁻⁸ W/m² K⁴ is the Stefan-Boltzmann constant, $T$ is the average temperature of the foam strut, and the extinction coefficient $K_{ext} = \frac{4.1\sqrt{1-\phi}}{2r}$ where $r$ is the pore radius.

For convenience, the thermal resistance is used to combine contributions from both conduction as well as radiation using the apparent thermal conductivity, and it is defined as

$$Rth = \frac{L_f}{k_{eff}A_f} \tag{4}$$

where $A_f$ is the cross-sectional area of the foam (same as that of the duct described in section 2.3). In this study, the foam samples have a square cross-section with 25 mm x 25 mm dimensions. The thickness of the foam $(L_f)$ is specified in the results section.

## 2.3 *Predicting the acoustic transmission loss of porous materials*

The foam is assumed to be 'rigid porous' in this study. Therefore, the softness of the foam due to the elasticity of the struts is neglected. The complex characteristic impedance $(\tilde{Z}c)$ and wave propagation constant $(\tilde{\gamma})$ for the foam material under consideration is determined using the phenomenological model of Dunn and Davern (Dunn & Davern, 1986) for rigid porous materials. This phenomenological model provides an empirical formula for $\tilde{Z}c$ and $\tilde{\gamma}$ based on flow-resistivity $(\sigma)$ and frequency *(f)*:

$$\tilde{Z}_c = \rho c\left\{\left(1 + 0.114\zeta^{0.369}\right) - j\left(0.0985\zeta^{0.758}\right)\right\} \tag{5}$$

$$\tilde{\gamma} = k_0\left\{\left(0.168\zeta^{0.715}\right) + j\left(1 + 0.136\zeta^{0.491}\right)\right\} \tag{6}$$

where $\zeta = \frac{\sigma}{\rho f}$ and $k_0 = \frac{2\pi f}{c}$, $\rho$ and $c$ are density and speed of sound in air, $\sigma$ is the flow resistivity of the foam. It is also possible to use a more refined model of the foam called the Johnson-Champoux-Allard or JCA model if the five microstructural parameters (porosity, flow-resistivity, tortuosity, viscous characteristic length, and thermal characteristic length) could be determined (Atalla, 2009).

For a given porous material, the flow resistivity $\sigma$ could be either measured or predicted if the unit cell configuration is designed (Deshmukh S., 2019). The transmission loss of a given foam is predicted assuming it is placed inside a plane-wave tube. Under the plane-wave assumption, which is valid until the cut-on of the first non-planar mode in the duct, the acoustic wave propagation inside the duct with the foam may be predicted as follows. Let us assume the duct is excited by velocity $u_0$ of a piston located at one end $(x=0)$ and has anechoic termination at the other end. Because the foam sample is placed at $x=L$ and has length $L_f$, a fraction of the power in the plane wave generated by the piston will be reflected at $x=L$, and the remaining power contained in the wave will be either absorbed inside the foam or transmitted downstream. The derivation for pressure field inside the duct is given in Ramamoorthy and Krishnan (Ramamoorthy & Krishnan, 2018). The final expressions are provided below.

The transmission loss across the foam is given by

$$TL = 20\,\log_{10}\left(\left|\frac{p_{inc}}{p_{trans}}\right|\right) \tag{7}$$

where $p_{inc}$ is pressure incident on the porous sample and $p_{trans}$ is pressure transmitted across the sample. The incident and transmitted pressures are given by

$$p_{inc} = \frac{\rho c u_0}{1 - R_L e^{-j2kL}}e^{-jkx} \tag{8}$$

$$p_{trans} = \rho c u_{Lb} e^{-jk(x-L-L_f)} \tag{9}$$

where $u_{Lb}$ is the velocity at $x = L + L_f$ given by

$$u_{Lb} = \frac{u_L e^{-jk_f L_f}}{1 - R_{Lb} e^{-j2k_f L_f}} (1 - R_{Lb}) \tag{10}$$

$u_L$ is the velocity at $x = L$ given by

$$u_L = \frac{u_0 e^{-jkL}}{1 - R_L e^{-j2kL}} (1 - R_L) \tag{11}$$

$R_L$ and $R_{Lb}$ are the complex reflection coefficients at the front and back surfaces of the foam sample, that is at $x = L$ and $x = L + L_f$ respectively:

$$R_L = \frac{\dfrac{Z_L}{\rho c} - 1}{\dfrac{Z_L}{\rho c} + 1} \tag{12}$$

$$R_{Lb} = \frac{\dfrac{Z_{Lb}}{\tilde{Z}_c} - 1}{\dfrac{Z_{Lb}}{\tilde{Z}_c} + 1} \tag{13}$$

Here, $Z_L$ is the surface impedance looking into the foam, $Z_{Lb}$ is the impedance behind the foam and its value is $\rho_c$ because anechoic termination is assumed at the end of the duct. The surface impedance of the foam is therefore given by

$$Z_L = \tilde{Z}_c \frac{Z_{Lb} \cosh\cosh\left(\tilde{\gamma}L_f\right) + \tilde{Z}_c \sinh\sinh\left(\tilde{\gamma}L_f\right)}{Z_{Lb} \sinh\sinh\left(\tilde{\gamma}L_f\right) + \tilde{Z}_c \cosh\cosh\left(\tilde{\gamma}L_f\right)} \tag{14}$$

where $\tilde{\gamma} = j\tilde{k}$ is the complex propagation constant in the foam given in Eq.(6).

The acoustic power transmitted fraction or APTF is defined as:

$$APTF = \frac{1}{10^{TL/10}} \tag{15}$$

APTF is sometimes also called the power transmission coefficient. It is used as the quantitative measure of acoustic insulation of the given foam material in this article. APTF is used for the combined thermal-acoustic evaluation because it is a ratio between 0 to 1, whereas TL is a logarithmic quantity. After determining APTF as a function of frequency, its average over the 1-4 kHz frequency range is obtained. A material with lower APTF gives better acoustic insulation.

**2.4** *Design a surface-based periodic foam of body-centered cubic (BCC) unit-cell configuration*

In addition to uncompressed and compressed melamine, this study also evaluates the thermal-acoustic insulation of a designed periodic porous material made of the BCC unit cell configuration. The method of designing this unit cell has been described elsewhere (Krishnan, Murthy, & Garimella, 2006), (Deshmukh S., 2019) and is briefly summarized here. To design a BCC unit cell, eight quarter-spheres from end vertices and one full-sphere from the centroid are subtracted from a cubic cell geometry, as shown in Figure 1. The unit cell is repeated periodically in all three dimensions to create a BCC periodic foam material. Its pore size is directly given by the radius of the sphere used in the design. The reason to use this kind of surface based unit cell in this study (instead of, say, truss-based or other unit cell geometries) is two-fold. Firstly, the BCC unit cell closely resembles the Kelvin unit cell geometry which is similar to the geometry
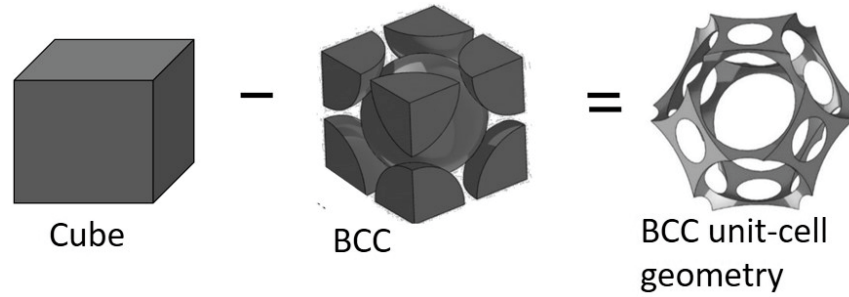
Cube − BCC = BCC unit-cell geometry

**Fig. 1.** Design of a body centered cubic (BCC) unit cell by subtracting eight quarter spheres from the end vertices and one full sphere from the centroid of a cubic unit cell.

observed in stochastic foams. Secondly, the 'sphere subtraction method' used to generate these unit cells provide easy manipulations to change the pore-size by varying $r$ and porosity using just the $r/a$ ratio (ratio of radius of the sphere to the length of the unit cell). The porosity of the BCC foam is determined by the sphere radius and the length of the unit-cell cube and is given by (Krishnan, Murthy, & Garimella, 2006), (Ramamoorthy & Krishnan, 2018).

$$\phi = \frac{V_f}{V} = \frac{2\left[\frac{4\pi}{3}r^3 - \frac{\pi}{3}(4r+s)(2r-s)^2 - 2\pi\left(r-\frac{a}{2}\right)^2\left(2r+\frac{a}{2}\right)\right]}{a^3} \tag{16}$$

where $V_f$ is the fluid or open volume, $V$ is the total volume, $r$ is the radius of the sphere representing the pore, $a$ is the length of the side of the unit cell and $s = \frac{\sqrt{3}}{2}a$ is the center-to-center distance along the diagonal. This expression for the porosity of the periodic module was obtained by accounting for the overlapping sphere volumes (Krishnan, Murthy, & Garimella, 2006).

## 3. RESULTS AND DISCUSSION

To evaluate stochastic porous materials for combined thermal-acoustic insulation, the two main parameters to choose are its porosity and pore-size. The measure 'pores per inch' or PPI is defined as the number of unit cells within one inch of the foam in a single dimension. A foam with larger PPI has smaller size pores. Compressing a foam decreases its thickness but increases its flow-resistivity. Therefore, the net effect it has on the transmission loss needs to be determined, and shown next for compressed melamine foam. Its effect on thermal insulation is also demonstrated in the following subsection.

### 3.1 Uncompressed and compressed melamine foam

In order to analyse the effect of compressing foams on their thermal and acoustic insulation properties, a type of melamine foam (Basotect® TG) which can be thermoformed to make customized components is considered. Kino *et al.* (*Kino*, 2009) report the non-acoustical microstructural parameters for this melamine foam compressed gradually up to a factor of about 10 and shown here in Table 1.

Using the melamine data from Kino **et al.** (*Kino*, 2009) shown in Table 1 and the method to determine APTF discussed in section 2.3, the APTF for Basotect® TG melamine for varying levels of compression is shown in Figure 2. For the best acoustic insulation, APTF should be as small as possible. As foam thickness decreases owing to a higher level of compression, the flow resistivity increases, as seen in Table 1, and concomitantly, the APTF also decreases. A foam cross-section of 25 mm × 25 mm is used in this study, and this does not affect the qualitative results. The APTF and *Rth* shown in Figure 2 are not obvious because there are two conflicting factors when melamine is compressed. On the one hand, the flow resistivity drastically increases, and the porosity mildly decreases. But, on the other hand, the thickness

**Table 1.** Properties of compressed Basotect® TG melamine from Kino *et al. (Kino, 2009).*
The first row of data is for the uncompressed sample.

| Sample Thickness $L_f$ (mm) | Porosity $\phi$ | Flow resistivity $\sigma$ (Pa s/m$^2$) | Density $\rho_f$ (kg/m$^3$) | Pore radius $r$ (μm) (taken from thermal characteristic length in Kino *et al. (Kino, 2009)* |
|---|---|---|---|---|
| 19.74 | 0.9944 | 6197 | 8.77 | 572 |
| 18.32 | 0.9939 | 7465 | 9.59 | 512 |
| 15.36 | 0.9931 | 9261 | 10.86 | 417 |
| 13.89 | 0.9918 | 12252 | 12.85 | 350 |
| 11.23 | 0.9900 | 17395 | 15.72 | 263 |
| 5.75 | 0.9822 | 36937 | 15.73 | 164 |
| 2.78 | 0.9628 | 122325 | 27.90 | 69 |
| 2.25 | 0.9544 | 160828 | 58.39 | 59 |
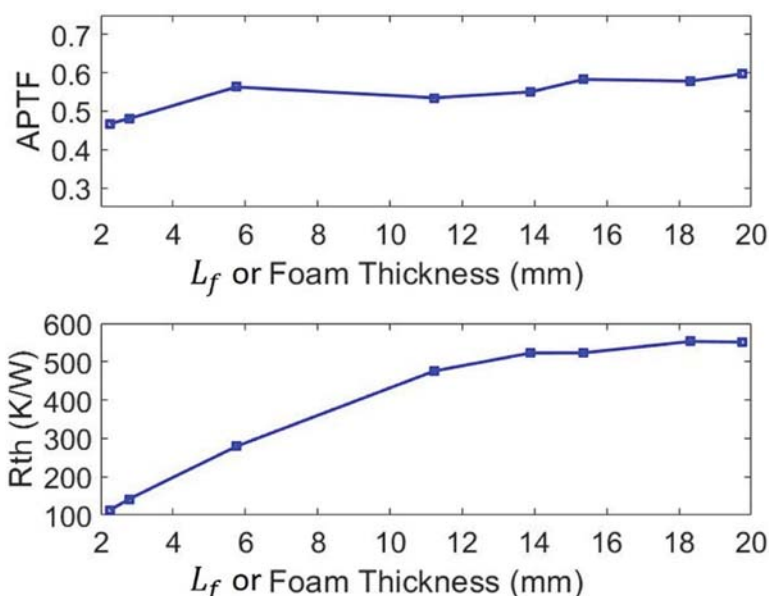


**Fig. 2.** APTF and Rth for compressed melamine foam. The x-axis is thickness of the melamine foam. Lower thickness represents larger compression.

is also significantly reduced. Despite these contrasting factors, compressed melamine provides lower *APTF*, that is, better acoustic insulation.

However, *Rth* becomes smaller with foam compression, as seen in the bottom panel of Figure 2. From Eq. (4), *Rth* is inversely proportional to the effective thermal conductivity $k_{eff}$. To see why *Rth* decreases with foam compression, the components of the effective thermal conductivity are plotted against porosity and against pore radius in Figure 3. As seen in the left panel in Figure 3, with an increase in the relative density or (1-$\phi$), the radiation component of thermal conductivity decreases significantly while the conduction component mildly increases. The variations with pore radius are shown in the right panel of Figure 3. As the pore radius increases, the radiation component of thermal conductivity increases, whereas the conduction component mildly decreases. From the parameters listed in Table 1, it can be seen that
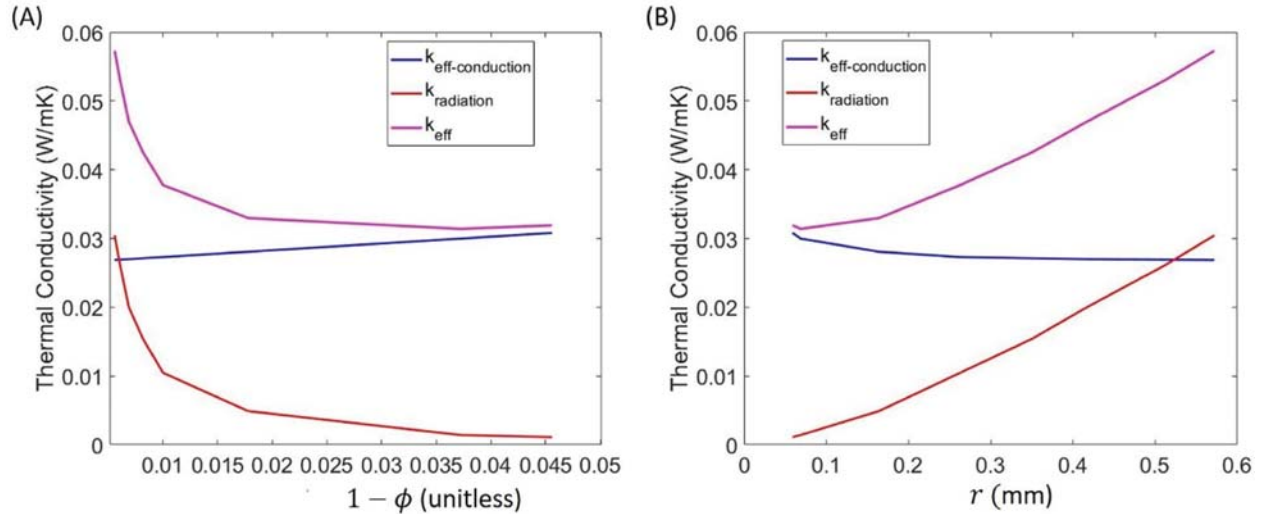
**Fig. 3.** Thermal conductivity of compressed Basotect® TG melamine using microstructural parameters from Kino *et al.* (*Kino,* 2009) shown in Table 1 and Eq. (1) - Eq. (3). (A) With increase in the relative density or (1-$\phi$), the radiation component of thermal conductivity decreases, whereas the conduction component increases. (B) With increase in the pore radius, the radiation component of thermal conductivity increases but the conduction component slightly decreases.

with compression of the melamine foam, its pore radius almost proportionately decreases along with a mild decrease in $\phi$ (or mild increase in 1-$\phi$). The combined effect of a decrease in $\phi$ and decrease in pore radius results in an overall decrease in the effective thermal conductivity $k_{eff}$ with compression of melamine. Therefore, when the melamine sample is compressed, *Lth* decreases but $k_{eff}$ decreases more drastically, and hence the overall effect is reduction of *Rth* as seen from Eq. (4). Note that the predicted thermal conductivity for uncompressed melamine foam from Figure 3 is about 0.05 W/mK which is approximately in agreement with 0.035 W/mK at 10°C as per Basotect® datasheet. For better thermal insulation, the thermal resistance should be higher. In short, compressing melamine foam improves acoustic insulation but worsens thermal insulation.

### 3.2 Periodic BCC foam

When a foam material is designed, it is possible to vary its porosity, poresize, as well as unit-cell configuration. This method could lead to designing material for an application. As of this article's date, it is possible to additively manufacture about 20 PPI foams, or equivalently, about 1 mm pore size and strand thickness of about 0.1 mm. However, the 3D printing technology is likely to improve and allow for the fabrication of even smaller pore sizes and complex geometries. The porosity and flow resistivity of the BCC foams included in this study are shown in Table 2.

As a possible material, consider BCC periodic foam designed as per the method described in section 2.4. The porosity is varied by choosing the ratio of *r/a* which is the ratio of the radius of the pore to the length of the cube. Porosity range of 0.94-0.99 is considered here. Lower porosities are not used because *Rth* reduces with a reduction in porosity. As with melamine foam, the same cross-section of 25 mm × 25 mm is used here, which impacts quantitative results but not the qualitative results. The pore sizes used are 0.25 mm to 2 mm. The thickness of the foam sample is $L_f$ = 50 mm. The material is assumed to be a polymer with solid thermal conductivity of 0.4.

For these designed BCC foams, the APTF and *Rth* predicted using the methods discussed in sections 2.2 and 2.3 are shown in Figure 4(B). APTF decreases (better) with decrease in pore radius *r*. *Rth* also increases (better) with decrease in pore radius r. Therefore, it is better to use a small pore size *r* for better

**Table 2.** Flow resistivity versus porosity forthe designed BCC foam. See *(Ramamoorthy & Krishnan, 2018)* for the method used to determine these flow-resistivity values. The values shown are for pore-size of 0.25 mm. The flow-resistivity for another pore-size r in meters can be determined by multiplying $(0.00025/r)^2$ to the value shown in the table.

| Porosity $\phi$ | Flow resistivity $\sigma$ (Pa s/m$^2$) |
|---|---|
| 0.9400 | 6836.8 |
| 0.9450 | 6511.4 |
| 0.9500 | 6203.1 |
| 0.9550 | 5910.9 |
| 0.9600 | 5633.8 |
| 0.9650 | 5371.1 |
| 0.9700 | 5122.0 |
| 0.9750 | 4885.5 |
| 0.9800 | 4661.1 |
| 0.9850 | 4448.1 |
| 0.9900 | 4245.8 |
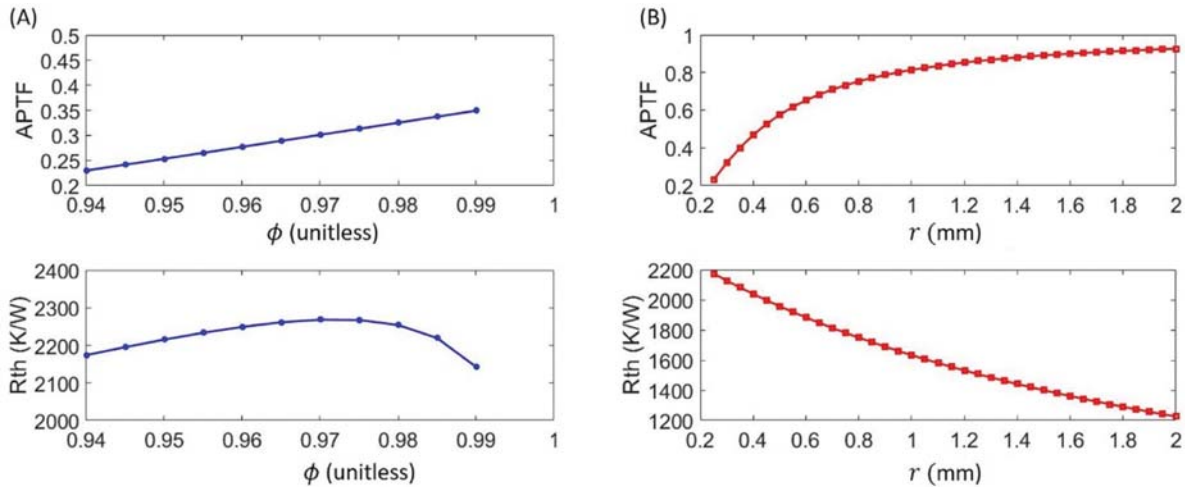


**Fig. 4.** *APTF* and *Rth* for BCC periodic foam (A) versus porosity for a pore-radius of 0.25 mm, and (B) versus pore-size for a porosity of 0.94. It is seen that the *APTF* is lower (better) at smaller porosity and smaller pore-radius. *APTF* increases monotonically with porosity as well as pore radius. Thermal resistance, on the other hand, is higher (better) at smaller pore-sizes, but could have a maximum versus porosity as seen in the lower panel in (A).

combined thermal-acoustic insulation. With decrease in *r*, the thermal conductivity due to radiation decreases linearly whereas the thermal conductivity due to conduction is nearly independent of *r* (Figure 5 (B)). Therefore, the overall *Rth* increases with decrease in *r* (see Eq. (4)).

With increase in porosity, APTF mildly increases as shown in Figure 4(A). Hence, lower porosity is better for acoustic insulation. Thermal conductivity due to radiation $k_{radiation}$ increases with porosity $\phi$, or equivalently, $k_{radiation}$ decreases with increase in relative density = $(1-\phi)$ as seen in Figure 5(A). On the other hand, $k_{(eff\text{-}conduction)}$ increases with increase in the relative density$(1-\phi)$. Owing to these conflicting trends, depending on their relative strengths, there is an optimum porosity for maximum thermal insulation. This optimum is manifested as peak in *Rth* vs $\phi$ shown in Figure 4(A).
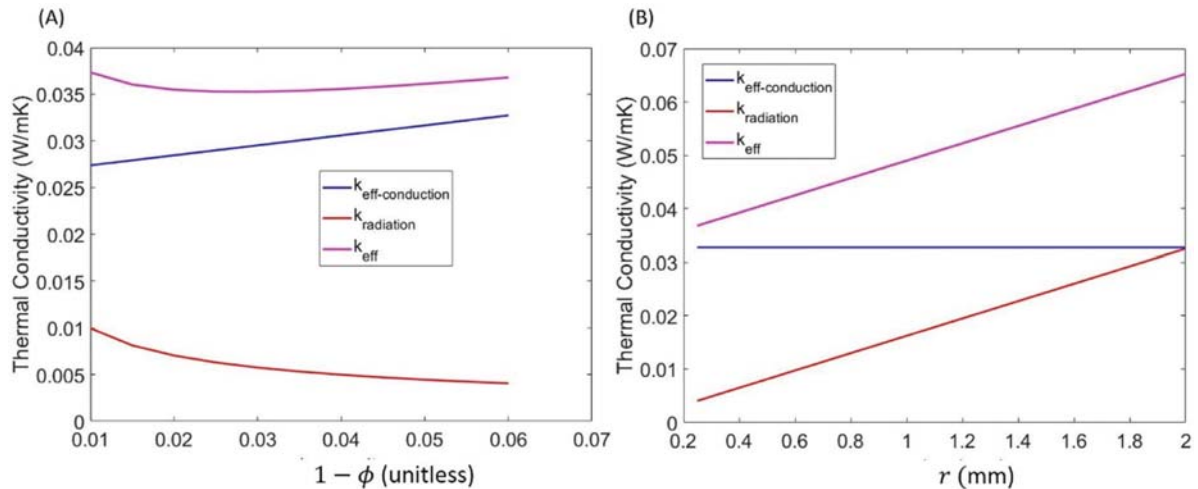
**Fig. 5.** Thermal conductivity of BCC foam (A) as a function of the relative density (1-$\phi$) for a pore radius of 0.25 mm and (B) as a function of pore radius at $\phi = 0.94$. The radiation component of thermal conductivity decreases with decrease in porosity, whereas the conduction component increases. From (B), with an increase in the pore radius, the radiation component of thermal conductivity increases whereas the conduction component stays nearly constant.

## 3.3 Combined view of thermal and acoustic insulation

For evaluating the combined thermal and acoustic insulation performances, a two-dimensional plot of *APTF* versus 1/*Rth* is considered. The plot of *APTF* vs 1/*Rth* with foam material as a parameter is shown in Figure 6. In this two-dimensional plot, the material with best-combined insulation would lie in the lower left corner where *APTF* and 1/*Rth* are both low. Hence this plot provides a guideline for material selection.
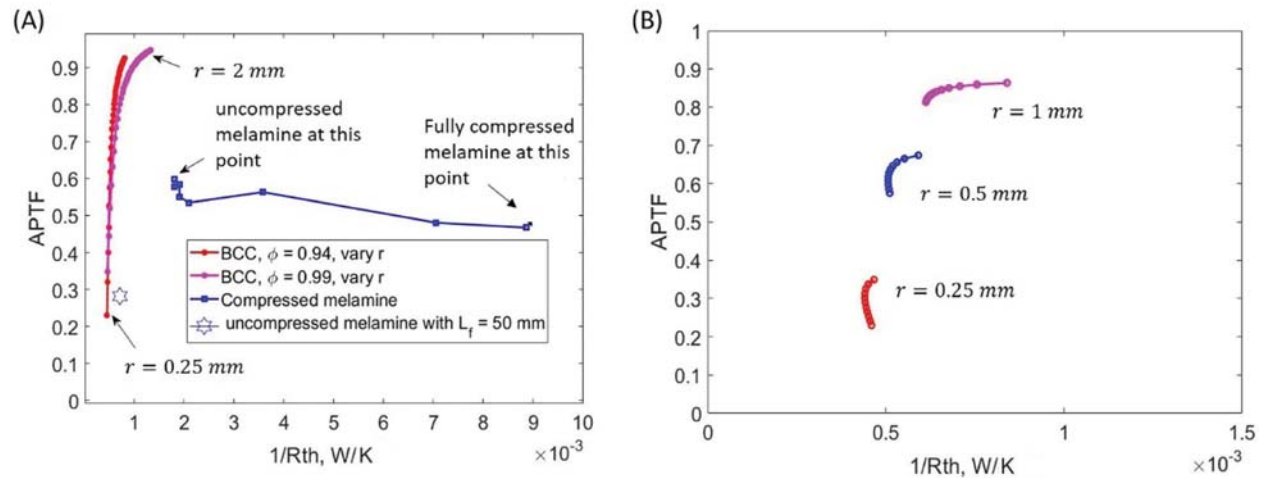


**Fig. 6.** *APTF* vs 1/*Rth* with foam material as the parameter is shown in this plot where lower left corner indicates a better material. (A) Compressed melamine with uncompressed thickness 19.74 mm, another uncompressed melamine with $L_f = 50$ mm (shown by a single marker-symbol), and BCC foam samples with $\phi = 0.94$, $\phi = 0.99$ with $L_f = 50$ mm. (B) BCC foam samples with pore radius $r = 0.25$ mm, 0.5 mm, 1 mm as indicated and each curve contains varying porosity from $\phi = 0.94$ to 0.99. This plot shows that the combined thermal-acoustic insulation is better for a foam with lower pore-size.

Among the two materials evaluated in sections 3.1 and 3.2, the uncompressed melamine foam has reasonable thermal insulation and moderate *APTF* as seen in Figure 6.

As seen in Figure 6 (A), compressing the melamine foam slightly improves its *APTF* but worsens thermal insulation by increasing 1∕*Rth*. The BCC periodic foam with porosity range 0.94-0.99 and pore radius 0.25 mm has better overall thermal-acoustic insulation than uncompressed melamine foam of the same 50 mm thickness (Figure 6 (A)). However, note that it may not be possible to fabricate periodic foam with 0.25 mm pore-size as of date, although this is expected to be possible with further advances in additive manufacturing. As mentioned earlier too, thermal-acoustic insulation also improves with thicker foam samples, which may be seen in Figure 6 (A) by comparing uncompressed melamine of thickness 19.74 mm vs 50 mm. Reduction in pore size is better for both acoustic insulation (lower *APTF*) and thermal insulation (lower 1∕*Rth*) as seen in Figure 6 (B).

## 4. CONCLUSION

The need for thermal and acoustic insulation materials exists in many applications, including but not limited to buildings, automotive, aviation, and others. When lightweight and higher strength-to-weight ratio are required, porous materials are chosen for the purpose. Compressed melamine is a thermosetting foam designed by Basotect that can be formed into complex shapes and could possibly fit into thin spaces and is widely used. A two-dimensional view of combined thermal and acoustic insulation performance is described in this article. Further, the possibility of designing porous material for combined thermal-acoustic insulation is explored. Using the example of a designed BCC foam, it is shown that combined thermal-acoustic insulation improves with decreasing the pore size (which may be limited by manufacturing feasibility), using an optimum porosity as discussed in the article, and by choosing the thickest sample that could fit into the available space in an application. The materials-by-design approach to thermal-acoustic insulation could be further extended beyond the examples discussed in this article.

## 5. ACKNOWLEDGMENT

## 6. REFERENCES

[1] Atalla, J. A., 2009. Propagation of sound in porous media: modelling sound absorbing materials. *John Wiley & Sons.*

[2] Deshmukh S., R. H. 2019. Design of periodic foam structures for acoustic applications: Concept, parametric study and experimental validation. *Materials and Design,* **175**, 107830.

[3] Dunn, I. P. and Davern, W. A. 1986. Calculation of acoustic impedance of multi-layer absorbers. *Applied Acoustics,* **19**(5), 321-334.

[4] Glicksman, L. R., 1994. Heat transfer in foams. In N. Hilyard and A. Cunningham, Low density cellular plastics. *Springer.*

[5] Kino, N. U., 2009. Investigation of non-acoustical parameters of compressed melamine foam materials. *Applied Acoustics,* **70**(4), 595-604.

[6] Krishnan, S., Murthy, J. Y. and Garimella, S. V., 2006. Direct simulation of transport in open-cell metal foam. *Journal of Heat Transfer,* pp. 793-799.

[7] Lee, B., Trcka, M. and Hensen J. L., 2011. Embodied energy of building materials and green building rating systems-a case study for industrial halls. *Sustainable Cities and Society,* **1**(2), 67-72.

[8] Nurzyński, J., 2015. Is thermal resistance correlated with sound insulation? *Energy Procedia,* **78**, 152-157.

[9]     Ohadi, M. and Qi, J. 2005. Thermal management of harsh-environment electronics. In Microscale Heat Transfer Fundamentals and Applications, *Springer.* pp. 479-498.

[10]    Ramamoorthy, S. and Krishnan, S. 2018. Towards thermal-acoustic co-design of noise-reducing heat sinks. *IEEE Transactions on Components, Packaging and Manufacturing Technology,* **8**(8), 1411-1419.

# Free vibration analysis of flexible narrow tubes using non-contact methods

**Aniket A. Hase[1], Manzoorahamad M. Mirza[1],**
**Deepak C. Akiwate[2] and B. Venkatesham[2*]**
*[1]Department of Mechanical Engineering, RIT Sakharale, Islampur, India*
*[2]Department of Mechanical and Aerospace Engineering, IIT Hyderabad, India*
*e-mail: venkatesham@mae.iith.ac.in*

## ABSTRACT

The flexible narrow tube structures have been the subject of several publications with applications in medical devices, mechanical structures, wire shields, and the food processing industry. Vibration analysis of such structures requires modal parameters, material properties and external load. The modal parameters can be measured by employing either contact or non-contact type excitation sources. For the thin, flexible structures, it seems quite challenging to use contact type excitation devices such as impact hammer or shaker. Also, other challenges arise for vibration measurement on thin walls using a contact-type sensor such as an accelerometer. Thus, this study engaged in the use of acoustic source as a non-contact vibration excitation and laser vibrometer as a non-contact vibration response measurement. An experimental test setup is developed to measure the natural frequencies using a modified acoustic Impedance tube that generates acoustic excitation in the desired frequency range. A laser vibrometer is used to measure the vibration response of the tube wall. In addition, a numerical model is developed based on finite element methods to estimate the natural frequencies and mode shape to support measured results. A systematic parametric study conducted to understand the effect of structural parameters such as diameter, length, and periodicity in the structure. Consequently, the results in the paper will assist in understanding the study of vibration response of the thin, flexible structures, where the conventional contact-type excitation source and contact-type sensors have limitations.

## 1. INTRODUCTION

Narrow flexible tubes are employed in medical and industrial applications. The vibration response of these tubes under dynamic excitation is one of the research topics in structural-acoustic coupled problems[1]. A first step in the dynamic characterization is the measurement of modal parameters such as natural frequencies, mode shapes, and damping. The flexible narrow tube structures have very thin walls and measuring modal parameters of such structures is quite challenging using contact type excitation methods like shaker or impact hammer. Similar challenges exist for measuring vibration response on thin walls using a contact-type sensor such as an accelerometer.

Modal parameters of flexible structures are sensitive to a small change in either geometry or boundary condition, and hence the measurement of vibration response of such structures becomes quite ambitious

---

as discussed in Mehmet Avcar[2]. Hence, the measurements of the modal parameters of these structures required a controlled environment. Farshidianfar A. et al. discussed a theoretical and experimental analysis of a long circular cylindrical shell[3]. They used non-contact acoustical excitation instead of contact excitation. It was demonstrated that only one acoustical source location is sufficient to excite all modes in the interested frequency range instead of multiple excitation points used in contact methods. Hence, the current study also focused on the use of non-contact acoustic excitation method rather than traditional contact type ones.

The main aim of the present work is to measure the dynamic response of narrow flexible tubes in a controlled environment with non-contact type excitation and response measurement methods. To carry out the measurements, a plane wave acoustic excitation was generated using an impedance tube setup discussed in reference[4], while vibration response of the tube is measured by laser vibrometer[4,5]. The non-contact vibration measurement method is appropriate for lightweight structures. Laser Doppler Vibrometry (LDV) is presently the technique that offers the finest displacement and velocity resolution used in many fields of basic science. The consideration of velocity data interpretation for lightweight structures has advantages over displacement[6,7]. Hence, vibration velocity of the structure was measured rather than displacement using LDV. The complete experiments were carried out under a free-free boundary condition, and the surrounding environment was ensured quiet to minimize the effect of background noise. A finite element method is used to compare the measured results with predicted ones[8,9]. A systematic parametric study was conducted to study the effect of diameter, length, membrane, and periodicity. The test methodology and results presented in this work become the basic framework for measuring the vibrations on the structure where contact type excitations and measurement techniques are not feasible to use.

## 1.1 Experimental setup and methodology

Figure 1 shows the schematic of the experimental setup used to measure the vibrations on the thin, flexible, narrow tube while the experimental setup and a closer view of the thin polypropylene straw sample is shown in Figure 2. The test sample tube was hung freely by two thin threads to achieve the free-free boundary condition during measurements. The periodic random noise generated by two different size impedance tubes to cover a different frequency range of excitation. The larger diameter impedance tube ($\phi$ 100 mm) used to generate the plane wave excitation in the frequency range of 63-1600 Hz, and a smaller size ($\phi$ 30 mm) impedance tube was used to provide acoustic excitation in the frequency range of 800-6300 Hz.
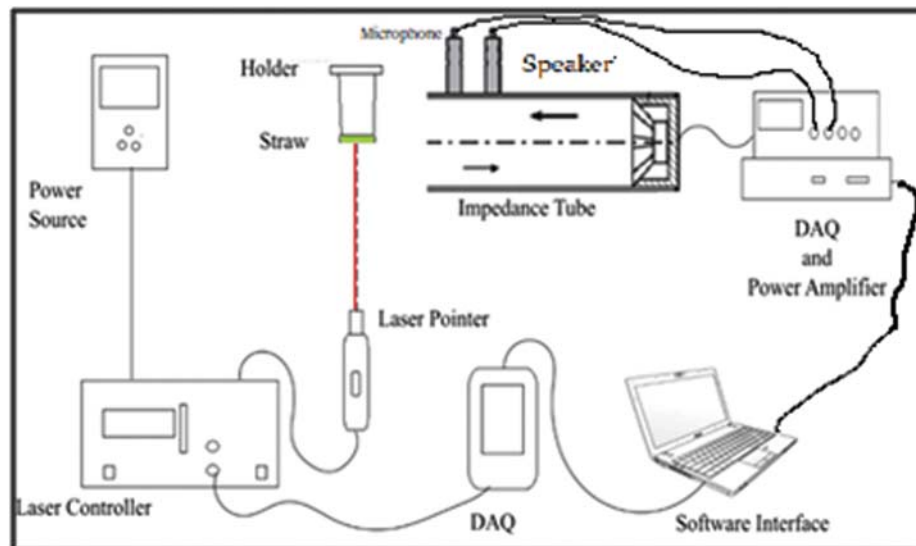


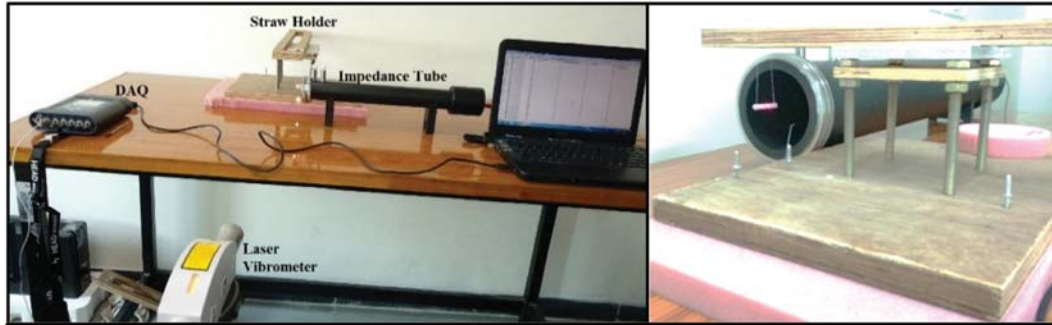**Fig. 1.** Schematic diagram of the experimental setup

**Fig. 2.** Test sample supported as a free-free B.C in the experimental setup

Two microphones were flush-mounted in an impedance tube which provides measured pressure data for calculating acoustic input power. Speaker was mounted at one end of the impedance tube, and another end was exposed to the test sample as shown in Figure 2.

Vibration velocity response as a function of frequency was measured on the tube wall surface by using a POLYTEC laser vibrometer. Laser vibrometer consists of a laser pointer that produces a visible red beam (l = 0.6328 μm) and has a maximum velocity range of 0.5 m/s, and minimum resolution is less than 0.05 microns/sec[5,10]. A sensitivity of 5 mm/s/V was used to sense the surface vibrations in the form of velocity because the tube vibrations due to acoustic excitations would be minimal and needed to be sensed with high accuracy.

Two different data acquisition (DAQ) systems were connected to a computer for further post-processing. One DAQ was used to measure input acoustic power. The same system was used as a function generator to provide signal input to the speaker connected to the impedance tube. The second DAQ system was used to measure the vibration response of laser vibrometer. However, these two DAQ systems were triggered from one computer. These two DAQ system functions can be integrated into one DAQ system in the future while developing customized measurements. The complete experiment was performed in a quieter room to avoid the effect of background noise and multiple reflections of sound.

## 1.2 *Description of test samples*

A polypropylene tube samples with four different diameters and three different lengths are considered to study the effect of the geometry on modal parameters. Also, structural features like the addition of membrane and periodicity in the structure were studied. A radial mode is one of the critical vibration modes to be identified for acoustic-structural coupled problems. The vibration measurements were carried out at a single point and chosen the middle of the sample length as a measurement location. However, the same measurement methodology can be conducted along the length and circumference for mode shape creation and curve fitting algorithms for modal parameter extraction.

Three different lengths (L) of 17 mm, 34 mm and 40 mm are considered, while the diameters (D) include 4 mm, 5 mm, 6 mm, and 10 mm. Two different wall thickness of 0.1 mm and 0.15 mm are considered in this study. Geometric details of the twelve test samples specified in Table 1. A nomenclature is introduced to find each sample based on the dimensions. It can be read as an example of "L17D4W1" which means length (L) of 17 mm, diameter (D) of 4 mm and wall thickness (W) of 0.1 mm.

### 1.2.1 Inclusion of membrane between two narrow tubes

To understand the effect of the membrane, two narrow tube samples with the same diameter and length of 17 mm are glued with a membrane in a back-to-back arrangement, as shown in Figure 3. This configuration is considered a single narrow tube with a length of 34 mm with a middle membrane. The notation for a sample is given as L34D5W1M. Free-free boundary conditions are created for the test sample by hanging with thin thread, as shown in Figure 2. The vibration measurements were carried out on the membrane as well as the tube wall.

**Table 1.** Dimensions of different narrow tubes used in an experimental study.

| Sample No. | Length (mm) | Diameter (mm) | Wall thickness(mm) | Notation |
|---|---|---|---|---|
| 1 | 17 | 4 | 0.1 | L17D4W1 |
| 2 | 34 | 4 | 0.1 | L34D4W1 |
| 3 | 40 | 4 | 0.1 | L40D4W1 |
| 4 | 17 | 5 | 0.1 | L17D5W1 |
| 5 | 34 | 5 | 0.1 | L34D5W1 |
| 6 | 40 | 5 | 0.1 | L40D5W1 |
| 7 | 17 | 6 | 0.1 | L17D6W1 |
| 8 | 34 | 6 | 0.1 | L34D6W1 |
| 9 | 40 | 6 | 0.1 | L40D6W1 |
| 10 | 17 | 10 | 0.15 | L17D10W1.5 |
| 11 | 34 | 10 | 0.15 | L34D10W1.5 |
| 12 | 40 | 10 | 0.15 | L40D10W1.5 |
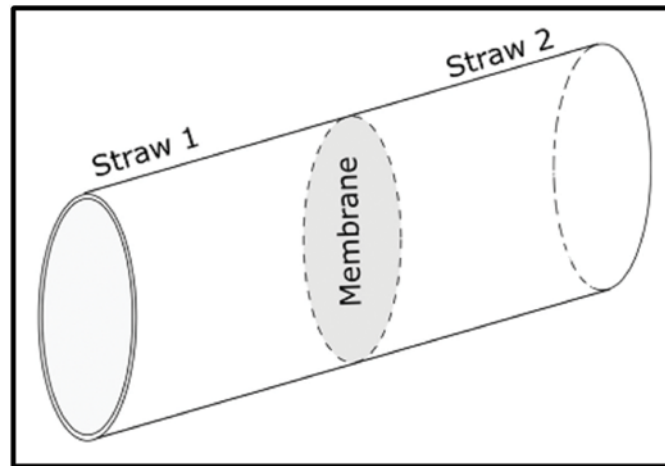


**Fig. 3.** Schematic Representation of glued straws in a back-to-back arrangement with a membrane in the middle

### 1.2.2 Inclusion of periodicity

A complete periodic sample was developed from the tubes of 6 mm diameter and the central membrane in-between layer of periodic tubes as shown in Figure 4. The complete length of sample was 34 mm while the diameter was 100 mm. The periodicity in the experimental model was achieved by two layers of straw core attached with a central polypropene membrane having thickness of 0.1 mm. The individual layers of straw core were obtained by wrapping the straw sample with cello tape in circular manner to obtain the 100 mm diameter sample. The vibration measurement was carried out on the membrane at various points of this periodic sample.

### 1.3 *Numerical modelling*

Numerical modal analysis using commercial Finite Element Method software (ANSYS) was performed to calculate natural frequencies and mode shapes of the selected experimental configurations. The predicted numerical results are compared with experimental results. For numerical analysis, the entire structure

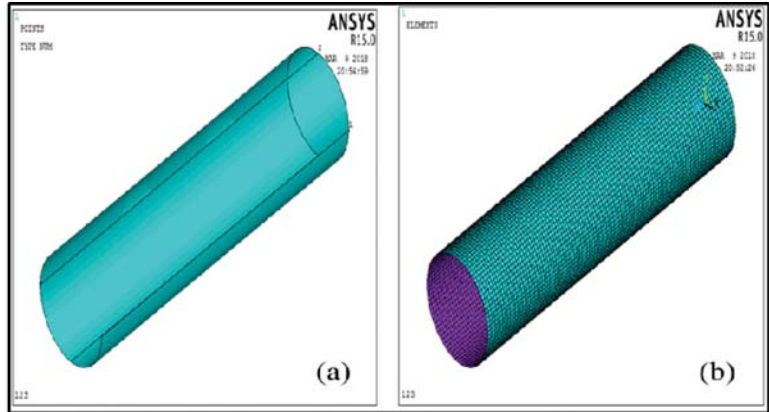**Fig. 4.** Periodic straw sample of 100 mm diameter with the membrane at middle

**Fig. 5.** (a) Geometric model (b) Meshed model of the tube sample

was discretized into elements on which boundary conditions or loads were applied[10]. The tube wall surface was discretized with Shell 63 elements. A mapped mesh was created by providing 100 divisions in the longitudinal and 20 divisions in circumferential directions. Free- Free boundary conditions were applied in the analysis. Polypropylene material properties shown in Table 2 were used for analysis and the material was assumed as isotropic. The Block-Lanczos modal extraction method was used in the analysis, and modes were extracted up to 6300 Hz[11]. The geometry and meshed model used for numerical analysis of a single flexible narrow tube are shown in Figure 5.

**Table 2.** Properties of tube used in the numerical analysis.

| Material | Density (kg/m$^3$) | Young's modulus (GPa) | Poisson's ratio |
|---|---|---|---|
| Polypropylene | 1200 | 1.15 | 0.4 |

Numerical modal analysis of the narrow flexible tube with the middle membrane was performed to calculate modal parameters. This sample modelled with the help of a previous single narrow tube (referred to as a unit cell) model, and the same unit cell copied in the negative direction, and the membrane was created with the area tool. The whole sample was glued together to form a narrow tube with a middle membrane. The dimensions of tube were a total length of 34 mm, a wall thickness of 0.1 mm, and a diameter of 5 mm. A membrane wall thickness of 0.1 mm was considered for the study. The complete structure was having an equal wall thickness of 0.1 mm in all directions. Figure 6(a) and Figure 6(b) shows the geometric model and meshed model of the structure considered for analysis.
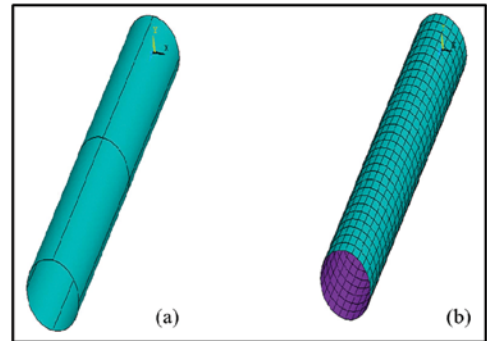


**Fig. 6.** (a) Geometric model (b) Meshed model of the single circular tube sample with the membrane at middle

The periodic arrangement of narrow tubes with middle membrane structure created using a unit cell as mentioned previously. The unit cell of circular tube diameter of 5 mm, 17 mm length, and 0.1 mm wall thickness was copied at a position so that the surface of a unit cell will match the opposite surface of the copied unit cell[1] as shown in Figure 6(a). The membrane between two layers of periodic structure was 0.1 mm thick. The same configuration was considered for the experimental study also. The meshing was done considering the same mesh parameters as taken for a single cell and the boundary condition
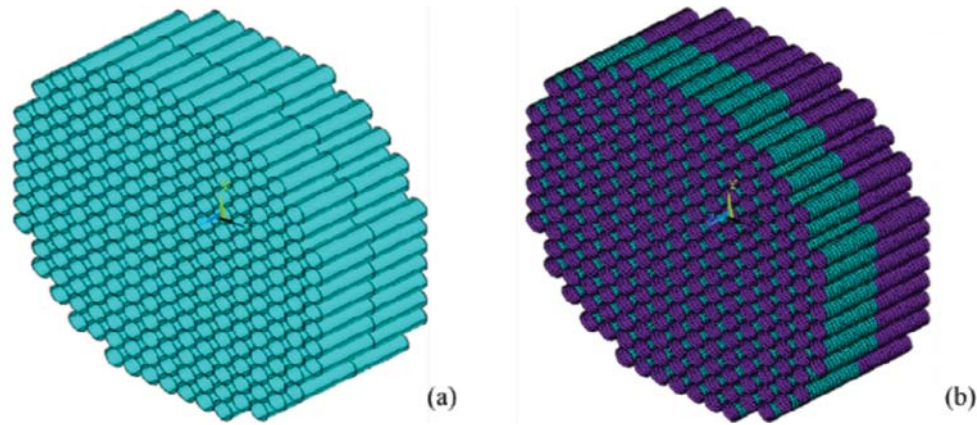
**Fig. 7.** (a) Geometric model (b) Meshed model of the 100 mm periodic straw sample

assumed was free-free. Full test sample dimensions of 100 mm diameter were considered for analysis instead of periodic boundary conditions applied to the unit section due to finite dimensions. The geometry and meshing of a complete periodic sample of 100 mm diameter are shown in Figures 7(a) and (b), respectively.

## 2. RESULTS AND DISCUSSION

By using plane-wave excitation, the vibration velocity was measured for 12 configurations of single narrow tubes, as mentioned in Table 2 under the free-free condition and are shown in Figure 8. The measured vibration response shows the peak values in the frequency range above 1000 Hz except for 10 mm diameter narrow tubes. The primary assumption in this method is the peak value in the response is associated with a natural frequency. However, this assumption needs to eliminate by implementing curve fitting methods in future work. The focus of the current study is to find the fundamental frequency by experimental method. From the results, it is observed that the increase in diameter of the straw causes the fundamental mode to shift towards the lower side and vice versa, as shown in Figure 8 and Table 3. For a change in length keeping diameter same, the natural frequency does not change for the considered samples. The longitudinal or bending modes are on the higher side and for considered cases, the radial modes which are independent of the length dominate as fundamental modes. The bending mode of case 3 (Sample, L40D4W1) could not find the fundamental axial mode in an experiment. It may be due to the amplitude of vibration being small at the single point measurement location. For sample number 4 (L17D5W1), the first two modes are closely spaced and cannot distinguish them in experimental results compared to numerical results.

Table 3 shows the comparison of fundamental natural frequency results obtained by the experimental and numerical methods for single circular tube samples. Here, the sequence followed for sample number is the same as in Table 2. The percentage error calculated is to cognize the deviations in results obtained by experimental and numerical results. The experimental outcomes are considered as a reference to compute the percentage error.

Comparing experimental and numerical natural frequencies of the first two modes indicates that the numerical method results are in good agreement with a maximum absolute error of 7.2%.

Table 4 shows the predicted first two mode shapes of single flexible narrow tubes. It is observed from numerical results that the fundamental mode is radial mode except in case 3, where the bending mode is fundamental. Results show that the radial modes are independent of the sample's length and depend only on the diameter. It could be observed that as the diameter of the tube increases the radial natural frequency reduces. As the diameter reduces, and length increases, the bending mode starts dominating as fundamental mode (case - c).
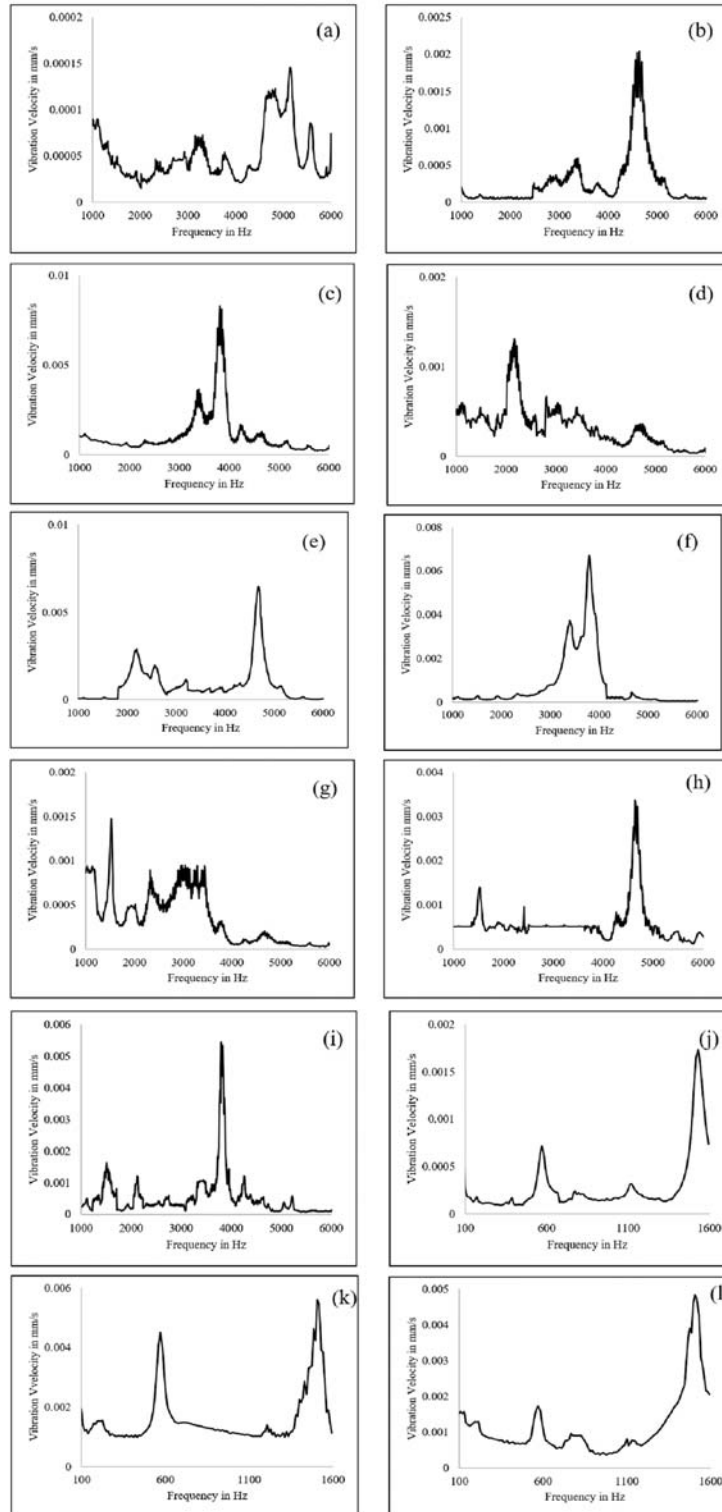
**Fig. 8.** Vibration measurement on different tube samples as per sequence given in Table 2
(a) L17D4W1, (b) L34D4W1, (c) L40D4W1, (d) L17D5W1, (e) L34D5W1, (f) L40D5W1, (g) L17D6W1, (h) L34D6W1, (i) L40D6W1, (j) L17D10W1.5, (k) L34D10W1.5, (l) L40D10W1.5

**Table 3.** Validation of results obtained for single circular straw samples without membrane at middle.

| Sample No. | $\omega_{Experiment}$ (Hz) | $\omega_{FEA}$ (Hz) | % Error |
|:---:|:---:|:---:|:---:|
| a | 3305.3 | 3452.4 | 4.4 |
|   | 3779.0 | 3504.3 | 7.2 |
| b | 3380.7 | 3456.3 | 2.2 |
|   | 3800.6 | 3760.2 | 1.0 |
| c | - | 2830.7 | - |
|   | 3423.7 | 3456.8 | 0.9 |
| d | 2207.1 | 2186.9 | 0.9 |
|   |   | 2242.8 | 1.6 |
| e | 2207.1 | 2189.9 | 0.7 |
|   | 2594.7 | 2781.8 | 7.2 |
| f | - | 2190.2 | - |
|   | 3413.0 | 3450.3 | 1.0 |
| g | 1518.0 | 1508.1 | 0.6 |
|   | - | 4263.7 | - |
| h | 1528.8 | 1510.5 | 1.19 |
|   | 2411.7 | 2494.6 | 3.4 |
| i | 1507.3 | 1510.8 | 0.2 |
|   | 3832.9 | 4015.2 | 4.7 |
| j | 581.3 | 535.1 | 7.9 |
|   | 1528.8 | 1513.9 | 0.9 |
| k | 570.6 | 536.42 | 5.9 |
|   | 1431.9 | 1516.9 | 5.9 |
| l | 570.6 | 536.6 | 5.9 |
|   | 1518.0 | 1517.1 | 0.05 |

## 2.1 *Effect of membrane in a flexible narrow tube*

The measured vibration velocity response on flexible narrow tube walls shown in Figure 9. As discussed in the previous section, a single straw sample without membrane shown the fundamental natural frequency at 2207.1 Hz (Refer Figure (8 - e)) and the same predicted in the numerical analysis for sample L34D5W1 as 2189.9 Hz. The addition of membrane shifts the first peak to 1528.8 Hz. This is because the addition of membrane (change in mass and stiffness) into the structure leads to a change in the configuration of a tube. The peak obtained at 1528 Hz, also observed that the fundamental mode shapes represent the complete tube configuration, not local membrane mode. The subsequent peak frequencies at 1933.9 Hz, 4288.1 Hz, and 5181.8 Hz are representing higher-order modes of the complete tube configuration.
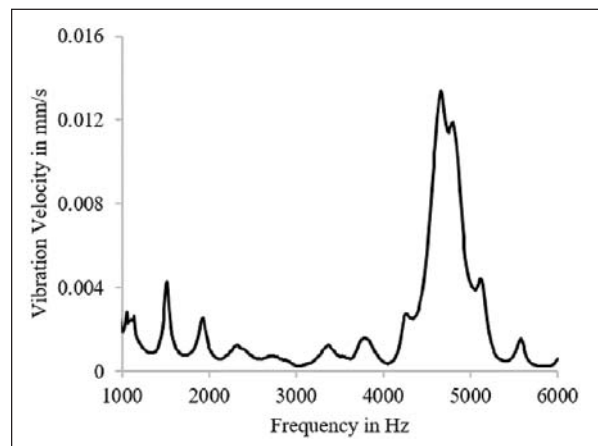


**Fig. 9.** Vibration measurement on the single flexible narrow tube with a membrane in the middle (L34D5W1M)

**Table 4.** Natural frequencies and mode shapes for a single circular narrow flexible tube sample.

| | $F_{n1} = 3452.4$ | $F_{n2} = 3504.3$ | | $F_{n1} = 1508.1$ | $F_{n2} = 1566.2$ |
|---|---|---|---|---|---|
| 1 (L17D4W1) | | | 7 (L17D6W1) | | |
| | $F_{n1} = 3456.3$ | $F_{n2} = 3760.2$ | | $F_{n1} = 1510.5$ | $F_{n2} = 2494.6$ |
| 2 (L34D4W1) | | | 8 (L34D6W1) | | |
| | $F_{n1} = 2830.7$ | $F_{n2} = 3456.8$ | | $F_{n1} = 1510.8$ | $F_{n2} = 2102.2$ |
| 3 (L40D4W1) | | | 9 (L40D6W1) | | |
| | $F_{n1} = 2186.9$ | $F_{n2} = 2242.8$ | | $F_{n1} = 535.14$ | $F_{n2} = 593.95$ |
| 4 (L17D5W1) | | | 10 (L17D10W1.5) | | |
| | $F_{n1} = 2189.9$ | $F_{n2} = 2781.8$ | | $F_{n1} = 536.42$ | $F_{n2} = 1516.9$ |
| 5 (L34D5W1) | | | 11 (L34D10W1.5) | | |
| | $F_{n1} = 2190.2$ | $F_{n2} = 2532.4$ | | $F_{n1} = 536.58$ | $F_{n2} = 1517.1$ |
| 6 (L40D5W1) | | | 12 (L40D10W1.5) | | |



With the addition of membrane, the numerical results are also shifted towards the lower side than the results of a simple tube sample (L34D5W1) of the same configuration without a membrane as shown in Table 4 (sample 5).

**Table 5.** Natural frequencies and mode shapes for a single circular narrow tube sample (L34D5W1 M) with a membrane in the middle.
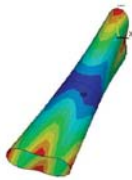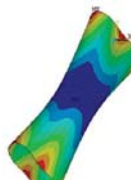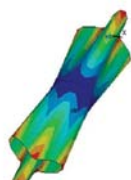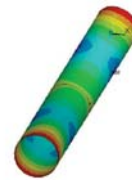
| $F_{n1} = 1533.1$ | $F_{n2} = 1944.3$ | $F_{n3} = 4296.0$ | $F_{n4} = 5189.7$ |
|---|---|---|---|
| | | | |

Table 5 shows the predicted natural frequencies and corresponding mode shapes of the considered tube sample. Table 6 shows the comparison of experimental and numerical results of fundamental natural frequencies. It is observed that error is less than 1% and there is a good agreement.

**Table 6.** Validation of results obtained for the single circular straw sample with a membrane.

| $\omega_{Experiment}$ (Hz) | $\omega_{FEA}$ (Hz) | Error (%) |
|---|---|---|
| 1528.8 | 1533.1 | 0.28 |
| 1933.9 | 1944.3 | 0.53 |
| 4288.1 | 4296.0 | 0.18 |
| 5181.8 | 5189.7 | 0.15 |

### 2.2 Addition of periodicity in the narrow circular tube with membrane in middle

This study emphasis on the discussion of the measurements performed on membrane only and not on the tube walls. The vibration measurement was carried out on the membrane at various points of the structure. Large-sized (100 mm diameter) impedance tube was used to generate plane wave excitation, and the interested frequency range was up to 1600 Hz.

Figure 10 shows that the addition of periodicity in the structure further disturbs the natural frequency and shifts it towards the lower side than that of the structure without periodicity and a membrane.
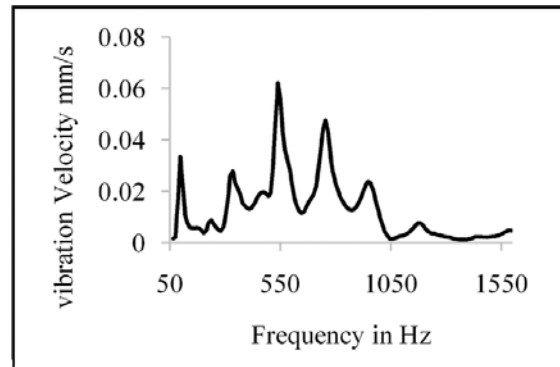


**Fig. 10.** Vibration measurement of the periodic straw sample with the membrane in middle

The natural frequency and first three mode shapes obtained by the numerical method are shown in Table 7. It is observed that overall structure modes are membrane dominant. The fundamental natural frequency reduced drastically as compared to a single narrow tube with and without membranes. Here,

**Table 7.** Natural frequencies and mode shapes observed in numerical analysis for straw configuration.

| | $F_{n1} = 75.34$ Hz | $F_{n2} = 146.19$ Hz (Axial) | $F_{n3} = 215.63$ Hz | $F_{n4} = 215.66$ Hz(Axial) | $F_{n5} = 299.3$ Hz |
|---|---|---|---|---|---|
| Mode shape in a Front direction | | | | | |
| Mode shape in Back direction | | | | | |

the mode shapes associated with axial variation (such as mode shape at 146.19 Hz) captured in the numerical model are missing in the measurements. So, it is better to do the measurements on the tube wall and membrane surfaces together.

Table 8 shows the comparison of experimental and numerical modal natural frequencies. The measurement error for fundamental natural frequency is more than 10%; however, the absolute frequency difference is not much. As the structure is periodic, the effect of membrane and change in each individual tube's functional boundary condition results in the natural frequency shifting towards a lower frequency compared to the single straw sample. Some of the modes were not captured in the experimental analysis as shown in Table 3 and Table 8, because these modes are symmetrical.

**Table 8.** Comparison of results obtained by the experimental and numerical method for 100 mm periodic circular sample.

| $\omega_{\text{Experiment}}$ (Hz) | $\omega_{\text{FEA}}$ (Hz) | Error (%) |
|---|---|---|
| 96.8 | 75.3 | 22.1 |
| - | 146.2 | - |
| 226.0 | 215.63 | 4.8 |
| - | 215.65 | - |
| 333.76 | 299.3 | 10.3 |

## 3. SUMMARY

The non-contact vibration measurement method has been discussed to find the natural frequencies of thin, flexible narrow tubes. An experimental setup has been developed to provide vibration excitation to the flexible narrow tube using an acoustic plane wave. The plane wave is generated by a speaker connected to a tube. Two different size tubes are considered for generating various frequency ranges. Vibration measurements were done using a non-contact laser vibrometer. The measured vibration response is used to find the natural frequency of the test sample. Three configurations were chosen for a test. The first configuration is a narrow circular tube with different diameter, length, and thickness. The second configuration is narrow circular tubes with a middle membrane, and the last configuration is an arrangement of narrow flexible tubes in a periodic manner with a central membrane.

A numerical modal analysis has been done to find the natural frequencies and mode shapes for chosen test sample configurations. The comparison between experimental and numerical results of the first few natural frequencies are shown a fair agreement. It was observed from the parametric studies that natural frequencies are reduced by introducing membrane and periodicity of single flexible narrow tubes. The fundamental natural frequencies of the tube are inversely proportional to its size (length, diameter).

The current manuscript provided preliminary results based on peak identification method from measured vibration response. However, further studies are needed to implement the traditional curve fitting methods to extract modal parameters. The proposed non-contact measurement method can be applied to measure the free vibration characteristics of thin structures like filter papers and thin membranes of acoustic meta materials where traditional contact type excitation and sensors may not be feasible to use.

## 4. ACKNOWLEDGEMENT

## 5. REFERENCES

[1]   C. Akiwate Deepak, D. Date Mahendr, B. Venkatesham and S. Suryakumar, 2018. Acoustic properties of additive manufactured narrow tube periodic structures, *Journal of Applied Acoustics,* **136,** 123-131.

[2]   Avcar Mehmet, 2014. Free Vibration Analysis of Beams Considering Different Geometric Characteristics and Boundary Conditions, *International Journal of Mechanics and Applications,* **4,** 94-100.

[3]   A. Farshidianfar, M. H. Farshidianfar, M. J. Crocker. and W. O. Smith, 2011. Vibration analysis of long cylindrical shells using acoustical excitation, *Journal of Sound and Vibration,* **330**(14), 3381-3399.

[4]   Aniket A. Hase, M. Mirza Manzoorahamad, Deepak C Akiwate, B. Venkatesham and Ravikumar V. Kamani, 2018. Vibration Analysis of Flexible Narrow Tubes using Acoustic Excitation, WESPAC 2018, New Delhi, India, November 11-15.

[5]   User Manual: Polytec Laser Vibrometer

[6]   Piyush Garg, 2017. Displacement Measurement Using a Laser Doppler Vibrometer Mounted on an Unmanned Aerial Vehicles, University of New Mexico, UNM Digital Repository.

[7]   Osami Sasaki and Nobusuke Seki, 1982. Measuring movement with an LDV system, *Journal of Optical society of America,* **21**(23), 4200-4202.

[8]   P. Castellini, G. M. Revel and L. Scalise, 2004. Measurement of Vibrational modal parameters using laser pulse excitation techniques, *Measurements,* **35,** 163-179.

[9]   D. Chapelle and K. J. Bathe, 1998. Fundamental Considerations for the Finite Element Analysis of Shell Structures, *Journal of Computers and Structures,* **66**(1), 19-36.

[10]  User Manual: ANSYS APDL

[11]  L. Komzsik, 2003. The Lanczos Method: Evolution and Application. 2nd edition. Society for Industrial and Applied Mathematics Publishers, Philadelphia.

# Under water acoustic performance optimization of a functionally graded viscoelastic lining

**S. Mishra, K. Parida and S.N. Panigrahi**

*School of Mechanical Sciences, Indian Institute of Technology Bhubaneshwar,*
*Bhubaneshwar-752050, India*
*e-mail: psatyan@iitbbs.ac.in*

## ABSTRACT

The development of anechoic linings is integral to the study of underwater acoustics. It has been observed that the present linings are designed to suit a single application. In this study, acoustic absorbers made of functionally graded viscoelastic materials (FGVMs), obeying the power-law variation, have been analytically investigated using a transfer matrix approach. A few geometric parameters and three key material properties were suitably varied along the thickness of the lining. The optimal values of these properties have been obtained by means of a single-objective genetic algorithm. A novel objective function has been developed which takes into account the highly conflicting requirement of obtaining the optimal transmission loss and echo reduction. The encouraging results obtained through the optimization process assisted in developing a set of guidelines for the selection of underwater acoustic linings to suit the application.

## 1. INTRODUCTION

Underwater vehicles delving deep into the sea are coated with acoustic linings for stealth. These vehicles are subjected to high pressures (~ 4-5 MPa for every 500m), making it vital for the linings to not only retain the geometrical integrity but also to maintain the designed acoustic characteristics. Owing to their high incompressibility, viscoelastic materials are usually employed for such kind of applications. Vibro-acoustic response of these linings has also been shown to be frequency-dependent. However, researchers continuously strive to achieve better performances over wider ranges of frequencies. By controlling the material properties, this objective can be achieved. Functionally Graded Viscoelastic Materials (FGVMs) are known to offer the liberty of smooth and continuous transition of their properties as a function of spatial dimensions. By appropriately controlling the variation in these material properties, the acoustic wave can be expected to see a gradual change of acoustic impedance while propagating through the lining that joins different zones of highly different characteristic impedances. This aspect of gradual change of impedance can be effectively used to control the reflection, transmission and absorption of acoustic waves in the lining. The present study focuses on exploiting the above mentioned flexibility in controlling the properties of FGVM for designing better anechoic linings.

A thorough literature survey shows that the literature on FGVMs is scarce. However, FGVMs possess properties much alike those of the generally used Functionally Graded Materials (FGMs), and therefore an investigation of the behaviour of the FGMs is imperative. A broad survey of the literature points to a

fact that the acousto-mechanical characteristics of an FGM lining not only depend on the gradation of its material properties, but also on the factors like size, position and operational frequency. Hence the study of wave propagation through FGMs is vital for the analysis of acoustic linings. In this regard, various numerical and analytical models to analyse the vibration and wave propagation in FGMs have been developed in the past[1-6]. These studies, however, have approximated the FGMs as multi-layered media, and the material properties within a layer are expressed either through linear or quadratic functions. This approach poses a difficulty in accurately approximating the material properties of the constituent particles within the volume composition. Another difficulty in studying the wave propagation in FGM linings comes from the different type of boundary conditions that these linings may have. Chiu and Erdogan[7] have tried to address this issue while analysing wave propagation in different combinations of functionally graded materials such as nickel/zirconia and aluminium/silicon carbide with varying boundary conditions. Under the influence of various boundary conditions, the acoustic wave propagation in the linings can be considered to possess the similar nature as that of propagation of stress waves in the material. Analysing from this angle, the effects of variation of material properties on stress wave propagation has been investigated by Moghaddam *et al.*[8] and it has been shown that the resulting stress field can be controlled by suitably controlling the grades along the thickness. The sound transmission loss (TL) is an important parameter to characterize the effectiveness of the lining. Chandra *et al.*[9] evaluated the TL of the FGM plate for several incidence angles and various power law distribution for representing the material gradation. Researchers have also used the transfer matrix method, a highly efficient 1-D approach, to obtain the TL by analysing the elastic wave propagation. This method has been extended for the study of a non-homogeneous domain where in the TL for the locally periodic structures has been evaluated using the Chebyshev polynomials[10]. All the above methods generally employ certain assumptions to make the linings bounded. However, some applications mandate the sizes of the linings, so they can be considered as unbounded panels. Hence analytical models to study the sound transmission through various unbounded panels too have been developed through matrix manipulation and Fourier component analysis[11]. Thus, the transfer matrix approach can be suitably adopted for the analytical investigation of the FGM linings, and with the variation in the material properties, the performance can be improved. The present study has tried to apply both the above mentioned approaches depending on the requirement.

While the majority of the studies have focused on predicting the acoustic performance of the linings by considering its physical and geometrical characteristics, it is also important to obtain the optimized values of these parameters. Numerous studies[12-15] have been conducted for the optimization of the acousto-mechanical properties of the structures. For instance, Genetic Algorithm (GA) has been used to optimize the parameters of the viscoelastic layer[16] and sandwich panels[17] under normal incidence for reducing the reflection of the acoustic wave. While GA has proved to be a powerful tool in obtaining the best possible parameters, the topology optimization method too has been found effective in the optimization studies. To cite a literature that has been of use in the present study, Zhang and Kang[18] carried out research on reducing the resonant noise and vibration in shell structures by minimizing the sound pressure at a point, and provided an optimal distribution of the damping material in the structure. Recently optimization of the acoustic characteristics has been done by Li and Li[19]. They have employed optimization techniques by taking the reflection coefficient as the objective function under zero transmission backing condition and formulated a relation between sound absorption of anechoic coating and optimum material distribution in the material. Literature are in abundance in the domain of optimization but it is evident that the focus has primarily been on optimizing the geometrical parameters, while the influence of material property distribution on the underwater performance still remains unexplored.

In the present study, an analytical formulation using transfer matrix method has been adopted to investigate the acoustic characteristics of the linings. By taking the advantage of flexibility in defining the material properties of FGVMs, optimization of some of the crucial material parameters has been carried out to meet the requirements of a superior underwater anechoic lining.

## 2. PROBLEM FORMULATION

The present study focuses on three major phenomena which occur when a lining is subjected to an acoustic wave : reflection, transmission and absorption, as shown in Fig. 1. It is a well-known fact that high frequency noise from internal machinery of underwater vehicles are hardly transmitted through the thick hull. However, it is quite difficult to avoid the transmission of low-frequency noise (100 Hz - 2 kHz). On the other hand, reflection of the waves from active sonar should be avoided for increasing the stealth of the vehicle. The above two phenomena are usually quantified by two parameters: Echo Reduction *(ER)* and Transmission Loss *(TL)*, given by

$$ER = 10\log_{10}\left(\frac{W_{inc}}{W_{ref}}\right) \; ; \quad TL = 10\log_{10}\left(\frac{W_{inc}}{W_{trans}}\right) \tag{1}$$

where $W_{inc}$, $W_{ref}$ & $W_{trans}$ represent the incident energy, reflected energy and the transmitted energy, respectively.
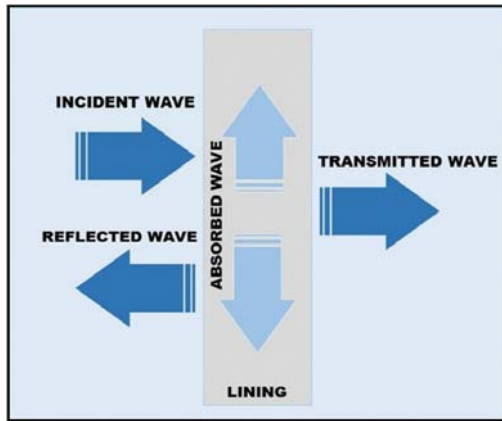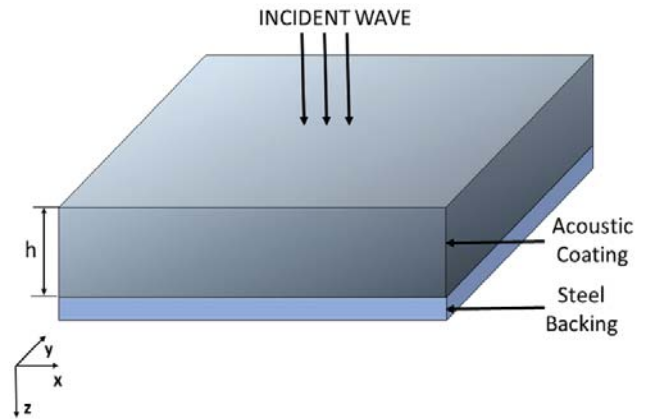


**Fig. 1.** Concept of Wave Propagation



**Fig. 2.** Typical configuration of simple-FGVM acoustic lining

While the former is used to quantify the effectiveness of a coating to avoid the reflection of any sound wave that impinges on it, the latter is used to quantify the degree of obstruction of any sound through the layer. Both of them represent a fraction of the incident energy, and the objective is to maximize both of them requires highly conflicting approaches. An efficacious way of simultaneously achieving these contradictory objectives is by maximizing the absorption of the acoustic wave inside the lining. The absorption coefficient of a material that depends on the damping property of the material can be given by:

$$\alpha^2 = 1 - |R|^2 - |T|^2 \tag{2}$$

here, *R* is the power reflection coefficient and *T* is the power transmission coefficient which are related to *ER* and *TL* defined earlier.

In order to investigate the above acoustic parameters, an FGVM layer of thickness h, submerged in water, and subjected to a harmonic wave impinging on the surface, as in Fig. 2, is considered. Such a configuration is termed as simple-FGVM as opposed to other configurations that will be taken in the subsequent sections. Considering the most prevalent conditions, only the waves normal to the surface are considered. The transverse dimensions of the plate, in *x*- and *y*- directions, are assumed to be infinite due to larger lateral dimensions as compared to the thickness. The Young's modulus, density and loss factor are defined as functions of thickness: $E = E(z)$, $\rho = \rho(z)$, and $\delta = \delta(z)$, respectively, in order to represent

the varying material property of the layer. The Poisson's ratio of the viscoelastic material is already very high ($\approx 0.4995$) and hence its variation in that range will not have any significant role in altering the acoustic characteristics of the lining. As such, the Poisson's ratio has been assumed to be constant along the thickness throughout the current study. FGVMs can be classified on the basis of the functions defining the variation in material properties. In this paper, FGVM following a material variation through power-law functions (P-FGVM) has been considered.

## 2.1 Material properties of P-FGVM

The variation of material properties in P-FGVM is characterized by a power function and is given by Eq. (3)

$$P_t(z) = P_0 + \left(\frac{z}{h}\right)^M (P_1 - P_0) \tag{3}$$

where $P_1$ and $P_0$ denote the material properties at $z=h$, and $z=0$, respectively. This is based on the Voigt model of the mixture to represent effective property of the lining as a function of a growth parameter $V_c$ which can be defined as a function of a non-dimensional distance between these surfaces[8]:

$$V_c = \left(\frac{z}{h}\right)^M (0 \le M \le \infty) \tag{4}$$

For the present study, the growth parameter behaves as volume fraction as taken from[8]. The parameter $M$, which is called the grading index, determines the rapidity with which the property changes along the thickness. A sharp variation of a material property near the end surfaces can be achieved by setting either a very small or a very large value for the parameter $M$. It can be observed that for $M=1$, the behaviour of P-FGVM becomes linear.

As the lining under investigation has to be designed for underwater applications, at least one of the two sides has been considered to be facing a semi-infinite domain of water and acoustic waves are assumed to be impinging on this surface. The frontal layer in contact with water has been assigned appropriate material properties with an intention to match the characteristic impedance to that of water. This enables the layer to minimize the reflection by encouraging the incident wave to enter the lining. The properties are thereafter varied along the thickness so as to attain maximum possible absorption of acoustic energy without any substantial reflection.

## 2.2 Theoretical model

The acoustic performance of linings made up of the above mentioned FGVM can be analysed mathematically by means of an analytical model. In this regard, the transfer matrix method is known to be a very powerful tool in obtaining the three parameters: *TL, ER* and absorption coefficient. Using this approach, the lining has been divided into *'n'* no of homogenous layers and each layer has been given the corresponding properties defined by *P* in the previous section. This yields a matrix formulation for each such layer which are combined to obtain the required parameters. A schematic of the division of the layers is illustrated in Fig. 3, where $T_1$, $T_2$...$T_n$ represent the transfer matrix for each individual layer of thickness $(l_r)$. The variation in the material property for a particular value of M can also be observed in the figure.

As the proposed acoustic lining has been considered to be infinite in lateral dimensions, compared to the thickness, the problem can be idealized into a one-dimensional wave propagation. Also since plane waves are considered in the analysis, the plane of the wave-front is perpendicular to the
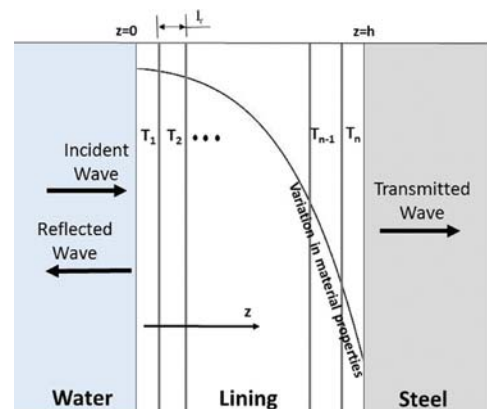


**Fig. 3.** Schematic representation of the transfer matrix layers in FGVM

*z-axis.* The governing equation of motion for the FGVM lining under consideration can thus be written in the similar form as the 1-D wave equation[20].

$$\frac{\partial^2 p}{\partial z^2} = \frac{1}{c^2}\frac{\partial^2 p}{\partial t^2} \tag{5}$$

where, $p$ is the acoustic perturbation on pressure and $c$ is the speed of sound in the medium and is given by

$$c = \sqrt{\frac{E}{\rho}} \tag{6}$$

Here $E$ is the Young's modulus of elasticity and $\rho$ is the density of the medium.

As is known, the general solution to Eq. (5) is given by:

$$p(z,t) = \left[ C_1 e^{-jkz} + C_2 e^{jkz} \right] e^{j\omega t}$$

and the corresponding particle velocity is given by

$$u(z,t) = \frac{1}{Z}\left[ C_1 e^{-jkz} + C_2 e^{jkz} \right] e^{j\omega t}$$

where $Z = \rho c$ is the characteristic impedance of the medium and $k$ is the wave number, given by $k = \omega/c, \omega$ being the angular frequency.

Considering steady-state sinusoidal variation of the temporal term, the following relationships are obtained

$$p = A^{-jkz} + B^{jkz}$$

and,

$$u = \frac{1}{Z}[Ae^{-jkz} - Be^{jkz}]$$

This leads to the formulation of the transfer matrix for the single layer of FGVM plate which can be written as[20]:

$$\begin{bmatrix} p_r \\ v_r \end{bmatrix} = \begin{bmatrix} \cos\ kl_r & jZ_r\ \sin\ kl_r \\ \dfrac{j}{zr\ \sin\ kl_r} & \cos\ kl_r \end{bmatrix} \begin{bmatrix} p_r - 1 \\ v_r - 1 \end{bmatrix} \tag{7}$$

From Eq. (7), transfer matrix for the $n^{th}$ layer can be written as:

$$T_n = \begin{bmatrix} \cos k_n l_n & jZ_r \sin k_n l_n \\ \dfrac{j}{Z_r \sin k_n l_n} & \cos k_n l_n \end{bmatrix} \tag{8}$$

$k_n$ is the wavenumber of the corresponding $n^{th}$ layer. The total transfer matrix can thereafter be evaluated using all the individual transfer matrices, as follows:

$$T = \Pi_{i=1}^{n} T_i = \begin{bmatrix} T_{11} & T_{12} \\ T_{21} & T_{22} \end{bmatrix} \tag{9}$$

For a viscoelastic material, the complex modulus of elasticity is given by

$$E = E^{'}\left(1 + i\delta\right) \tag{10}$$

is used. Here $E'$ represents the storage modulus of the FGVM plate and $\delta$ is the loss factor. These two quantities are evaluated using the relations for *P(z)* for different types of FGVMs defined in the previous section.

The Poisson's ratio *(v)* has been kept constant for the analysis, and the bulk modulus *(B)* and shear modulus *(G)* are calculated as:

$$B = \frac{E_0}{3(1+2v)}$$

$$G = \frac{E_0}{2(1+v)}$$

where $E_0$ is given by

$$E_0 = \frac{E(1-v)}{(1+v)(1-2v)}$$

Thereafter the speed of sound, can be calculated as:

$$c = \sqrt{\frac{3B+4G}{3\rho}} \tag{11}$$

and can be used to find out the wave number. Thus by knowing the thickness of each layer and the corresponding wave number, the coefficients of the transfer matrix can be readily evaluated. It is noteworthy that the speed of sound given by Eq. (6) is used when the cross-section of the medium is comparable to the wavelength of the incident sound wave. Since in the current study, these dimensions are considered to be infinite, the speed of sound has been evaluated by Eq. (11).

The impedances $Z_f$ and $Z_b$ are given as[21]:

$$Z_f = \frac{p_f}{v_f} \quad Z_b = \frac{p_b}{v_b} \tag{12}$$

here the subscripts $f$ and $b$ denote the front interface and back interface respectively. Thus from the transfer matrix, $Z_f$ is obtained as:

$$Z_f = \frac{T_{11}Z_b + T_{12}}{T_{21}Z_b + T_{22}} \tag{13}$$

and thereafter the *TL* and the *ER* of the anechoic layer can be evaluated by the following relations:

$$TL = 20\log\left(\frac{T_{11} + \dfrac{T_{12}}{Z_b} + T_{21}Z_b + T_{22}}{2}\right) \tag{14}$$

$$= 20\log\frac{1}{R}$$

here, $R$ is known as the reflection coefficient and is given by:

$$R = \frac{Z_f - Z_w}{Z_f + Z_w} \tag{15}$$

where $Z_w$ is the impedance of the water medium.

Finally, due to energy conservation, the sound absorption coefficient $\alpha$ can be calculated from Eq. (2).

## 3. OPTIMIZATION TECHNIQUE

As has been set earlier, the aim of the present work is to obtain an enhanced broadband *TL* and *ER* spectrum for the linings. However, they are crucial over different ranges of frequency. Hence the desired

performance should correspond to maximizing the areas under the *TL* and the *ER* curves separately. This in turn is equivalent to maximizing the fraction of the total energy being absorbed by the lining. This fraction can be expressed by means of the area under the spectrum of absorption coefficient $(\alpha_a)$. Therefore, while evaluating $\alpha_a$ from Eq. 2, instead of using *TL* and *ER*, squares of the coefficients of pressure transmission $(\alpha_t)$ and pressure reflection $(\alpha_r)$ should be used. It is noteworthy that while $\alpha_t$ represents the fraction of total energy transmitted across the lining, $\alpha_r$ represents the fraction which gets reflected from the lining. So Eq. (2) now can be expressed as:

$$\left|\alpha_\alpha(f)\right|^2 = 1 - \left|\alpha_r(f)\right|^2 - \left|\alpha_t(f)\right|^2 \tag{16}$$

In order to exemplify the above discussion for a typical layer of FGVM material that is completely submerged in water and having semi-infinite water on both sides, the *TL* and *ER* curves have been evaluated and presented in Fig. 4. For such a condition, the transmission coefficient can be seen to be starting from a very high value, of about one, at lower frequencies and it reduces quite sharply to attain very low values at higher frequencies. It can be observed that the fraction of the transmitted energy drops down to below 2% beyond about two kilohertz of frequency. This is highly undesirable as the internal noise sources are known to be generated at such low frequencies and are unaffected even by the thickness of the hull. Similarly, as can be observed from Fig. 4b, the reflection coefficient starts from very low value, and increases to about 90% at nearly 2000 Hz. This is very typical of the performance of such plates inside water. It can also be observed that for a given lining, the *TL* and *ER* are complementary to each other. With the increase in one the other tends to decrease, and thus it is a conflicting requirement to maximize both at the same time, as was discussed in the previous section.
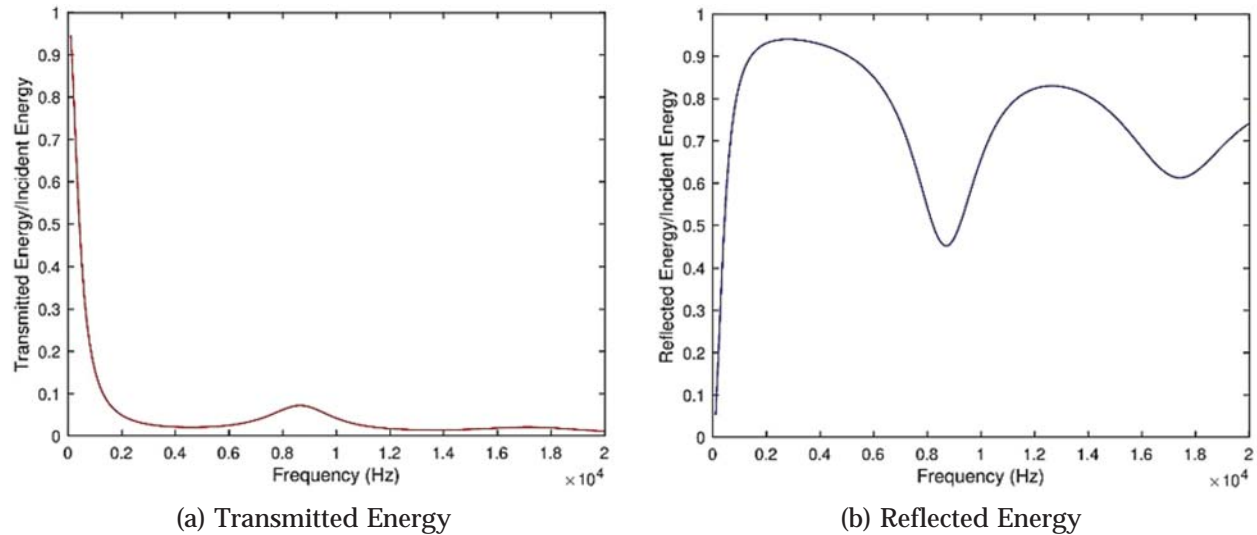


(a) Transmitted Energy                    (b) Reflected Energy

**Fig. 4.** A typical variation of transmitted and reflected energy versus frequency plotted as a fraction of the incident energy.

The corresponding variation of absorption coefficient with frequency is shown in Fig. 5. As depicted by Eq. (16), this curve represents variation of the actual fraction of energy that is being absorbed by the lining with respect to frequency for a typical plate in water and thus effectively describes the performance of the lining.

The absorption coefficient, as shown above, can be seen to be a function of frequency. The requirement is not only to have a very good absorption coefficient at any specific frequency, but to have the absorption as high as possible over the entire range of operation. Therefore, instead of looking at low values of *TC* or *RC*, it is desirable to make the area under these curves minimum. In other words, the area shown as shaded region in Fig. 6 needs to be maximized.
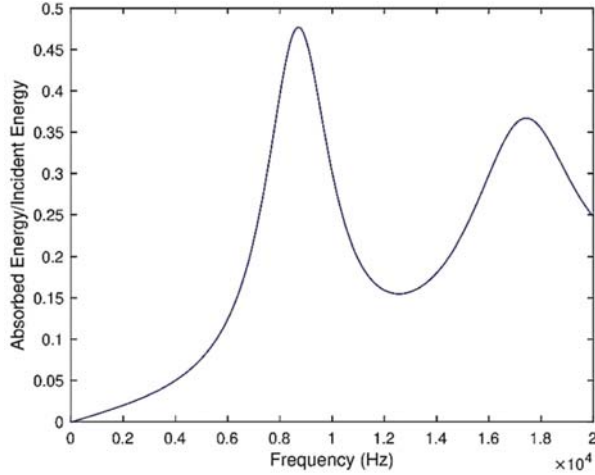
**Fig. 5.** Variation of absorbed energy versus frequency plotted as a fraction of the incident energy.
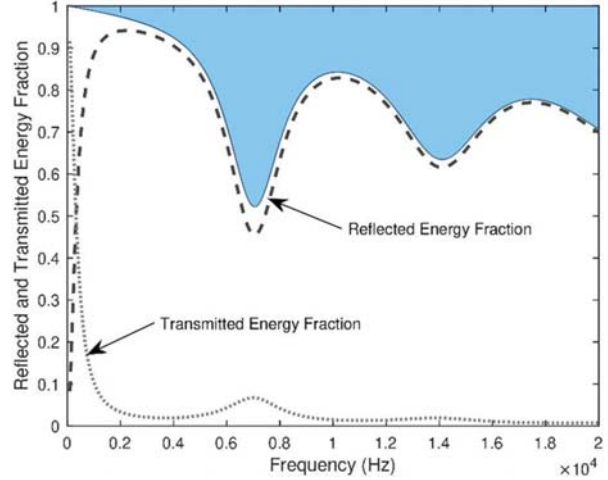


**Fig. 6.** Definition of the objective function for the problem at a hand

Hence, a very basic objective function can now be defined as follows

$$F_{0bj} = \int_{f_{min}}^{f_{max}} \alpha_\alpha^2(f)\,df = \int_{f_{min}}^{f_{max}} \left[ 1 - |\alpha_r(f)|^2 - |\alpha_t(f)|^2 \right] df \tag{17}$$

However, as discussed earlier, inasmuch as the transmission loss is quite important in the low frequency zone (<2000Hz) while the echo reduction is more important in the high frequency zone (>5000Hz), a more appropriate objective function can be developed by multiplying separate weight functions to each of these components as follows:

$$F_{0bj} = \int_{f_{min}}^{f_{max}} \alpha_\alpha^2(f)\,df = \int_{f_{min}}^{f_{max}} \left[ 1 - w_r(f)|\alpha_r(f)|^2 - w_t(f)|\alpha_t(f)|^2 \right] df \tag{18}$$

In order to make the objective function represent the requirement more appropriately, let $f_{max}^t$ be defined as the cutoff frequency for *TL* below which we require the transmission to be as low as possible. Similarly, let $f_{min}^r$ be defined as the cut off frequency above which the *ER* has to be very effective. The simplest condition could be to define step functions with the above mentioned frequencies as the band-stop and band-pass cut-offs for $w_t(f)$ and $w_r(f)$, respectively, as shown in Fig. 7a. The shown functions can be written mathematically as:

$$w_t(f) = \begin{cases} 0 & f < f_{max}^t \\ 1 & f \geq f_{max}^t \end{cases} \quad w_r(f) = \begin{cases} 0 & f < f_{min}^r \\ 1 & f \geq f_{min}^r \end{cases} \tag{19}$$

However, such kind of weight functions exhibit discontinuity at the location of the respective cut-off frequencies while it is desirable to have a smooth function over the entire domain. Therefore, this issue can be resolved by introducing some sigmoid type function to represent the weights. Two such functions are shown in Fig. 7b, and can be written mathematically as:

$$w_t(f) = \frac{1}{2}\tan h\left(-\lambda_t\left(f - f_{max}^t\right)\right) \quad w_r(f) = \frac{1}{2}\tan h\left(\lambda_r\left(f - f_{min}^r\right)\right) \tag{20}$$

where, $\lambda_t$ and $\lambda_r$ are constants which can play the role of controlling parameters in the optimization algorithm to control the steepness of the transition near the cut-off frequencies.
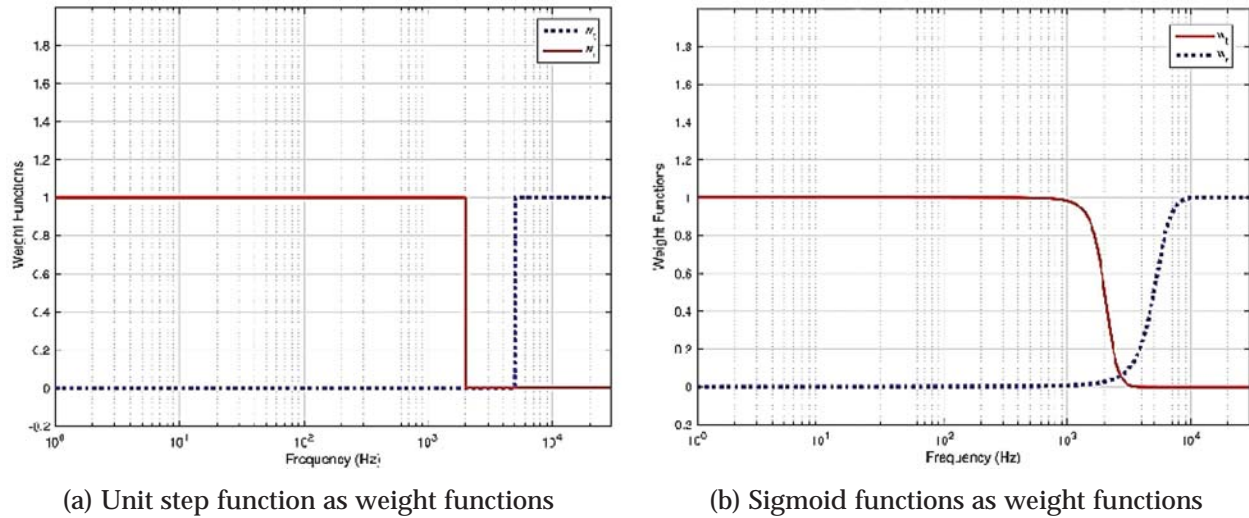
(a) Unit step function as weight functions

(b) Sigmoid functions as weight functions

**Fig. 7.** Suitability of various functions as weight functions.

Application of these functions on some representative *RC* and *TC* curve are shown in Figs. 8a and 8b. Fig. 8a shows the effect of the weight function on two typical transmission coefficient spectra while Fig. 8b shows the same for some typical reflection coefficient spectra. The curve denoted by $w_t$ represents the weight function with a smoothing parameter value of $\lambda_t = 0.002$ and the curve denoted by $w_r$ represents the weight function with a smoothing parameter value of $\lambda_r = 0.0006$. This diagram clearly depicts the effect of the weight functions on *TC* and *RC* in nullifying the contribution of the transmission loss curve beyond the cut-off frequency. Moreover, it can be clearly observed that the weighted functions are completely smooth and can be integrated as and when required.
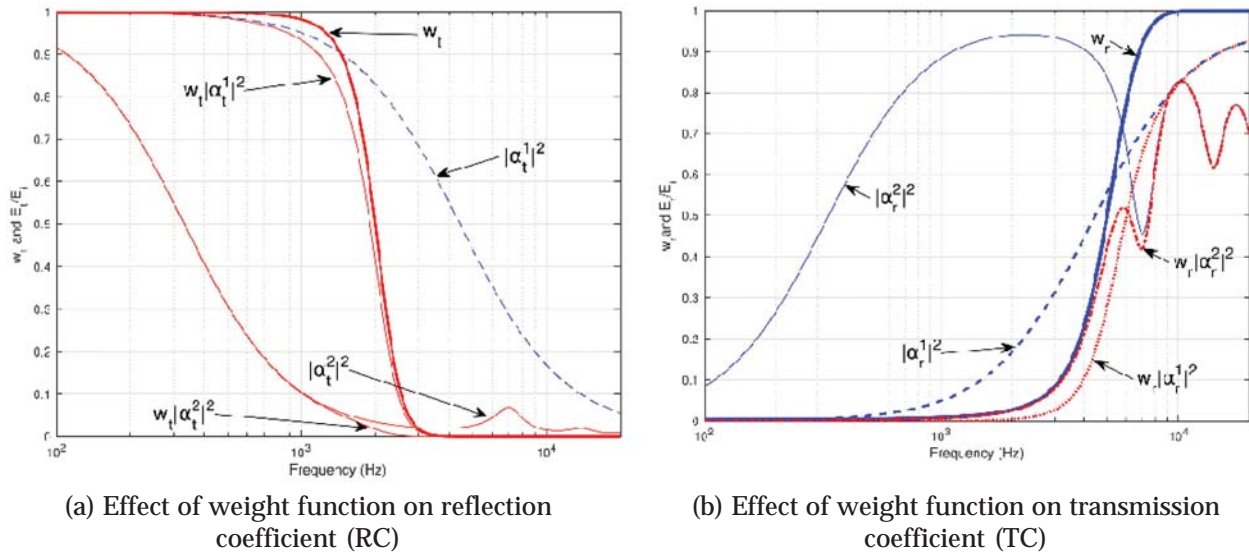


(a) Effect of weight function on reflection coefficient (RC)

(b) Effect of weight function on transmission coefficient (TC)

**Fig. 8.** Effect of weight functions on the acoustic performance

For a given set of parameters, the effects of weighting functions on the actual absorption spectra are shown in Fig. 9a. It can be observed that the area denoted by 'a' will be present for any configuration as long as the weighting functions are fixed. The absorbed energy represented by this area is like a pseudo area and it does not contribute to any actual absorption. This area is a consequence of the specific forms
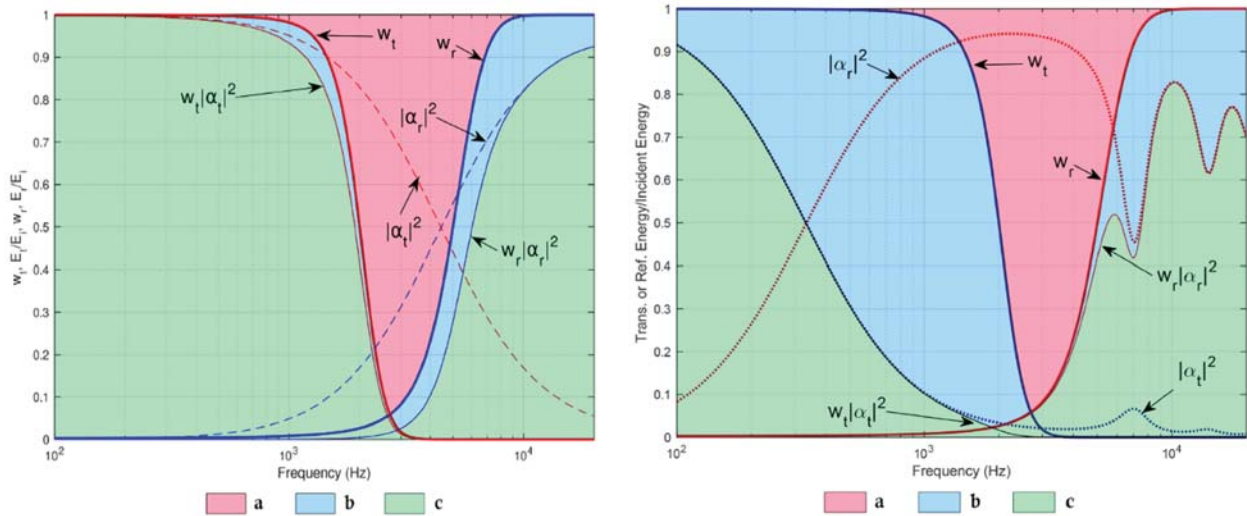
**Fig. 9.** Effect of weight functions on the absorption coefficient
(a) for one set of parameters, and (b) for different set of parameters

of the weighting functions, and is a result of the gap between the cut-off frequencies for $w_t$ and $w_r$. It does not affect the process of optimization as this dummy area is not considered in the analysis. Similarly, $c$ is the area which is not contributing to any of the absorption of the energy as this area represents the energy that is either getting reflected back or getting transmitted across the layer. However, the area $b$ represents an actual contribution from the presence of the material layer to absorption. It is thus quite clear that with the given weight functions, the objective is to increase area b as much as possible since no changes can be made to area a. Similarly, for another set of parameters, the actual absorption can be seen to be quite significant as presented in Fig. 9b.

## 4. VALIDATION OF THE DEVELOPED OBJECTIVE FUNCTION

The suitability and adequacy of the developed objective function in achieving the set goal has been evaluated by applying it to some well-known problems. These problems have been carefully chosen such that their response spectra (represented through closed-form functions) are known to share vital statistical characteristics with the developed objective function. As a matter of fact, the aim is not only to maximize the area under the curve, but also to have the standard deviation as minimum as possible, for the presence of any kinds of troughs and crests in the final curve tend to increase the standard deviation for the same area under the curve. This is undesirable owing to the logarithmic nature of addition of acoustic spectrum. Since the desired nature of the response spectrum of the chosen problem are well known and can be quantified in terms of the standard deviation, it is expected that the developed objective function can be validated by applying it on them.

From the current discussion, it is quite clear that to obtain the optimum response spectrum, while on one hand, the area under the curve has to be maximized, on the other, the standard deviation has to be minimized at the same time. This fits into the definition of a standard multi-objective optimization problem. In the present study, authors have chosen Genetic Algorithm (GA) as their optimizing tool due to its ease of use and its proven potential as an optimization algorithm. In line with this, the two-objective optimization at hand has been converted into a single objective optimization problem. This has made the process of optimization faster allowing more controlling parameters to be chosen over a wider search space. Consequently, a fitness function has been defined by using a penalty factor optimization method, given by:

$$F = F_{obj} - \beta \sigma_{obj} \tag{21}$$

where, $F_{Obj}$ is given by Eq. (18), $\beta$ is the penalty parameter and $\sigma_{obj}$ is the standard deviation of the objective function. A lower value of penalty factor signifies a greater bias towards $F_{Obj}$ and a higher value shifts the bias towards the standard deviation. This trade-off between the compromised values depend on the choice of $\beta$. Two examples have been considered to demonstrate the effectiveness of the fitness function in the subsequent sections.

### 4.1 Test Function-I

For the first level of validation, $sin^2(nx)$ has been adopted as a test function whose integral can be considered as $F_{obj}$ which has been optimized using the developed fitness function through GA.

Fixing the domain of this test function, which in turn signifies a restricted search space, brings out the actual strength of the developed fitness function. For instance, it can be observed from the Fig. 10 that both $F_{obj}$ and $\sigma_{obj}$ always remain the same for any integer value of n if the domain is set to the limits $[0, 2\pi]$. Focussing only on the $F_{obj}$ as the fitness function for now by taking $\beta = 0$ in Eq. 21, a variation in $F_{obj}$ can be observed for irrational values of *n* as shown in Fig. 11a. It can be seen that the maximum value of $F_{obj}$ is obtained



**Fig. 10.** Plot of the three test functions

in the search space [0.25 0.5]. The fitness function when optimized using GA comes out to be 3.8241 for *n* = 0.3576 which has been validated to be in accordance with the result obtained from Fig. 11b.
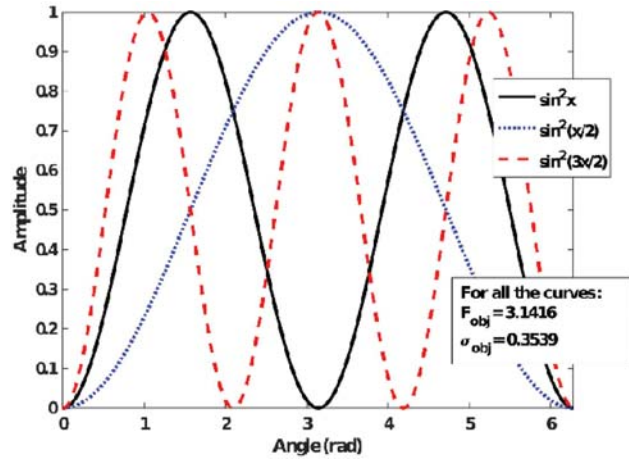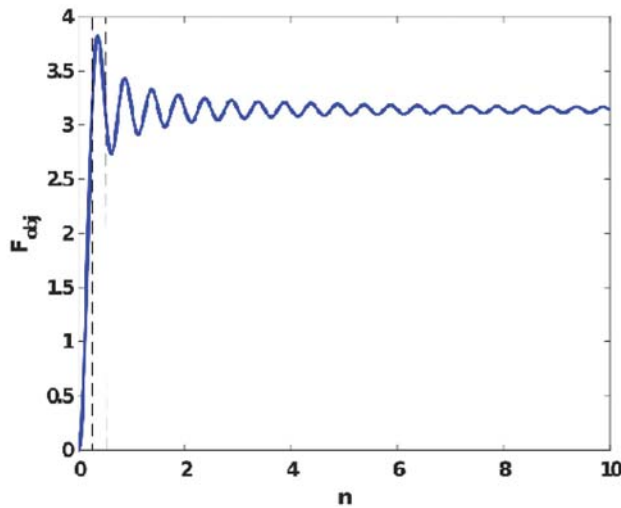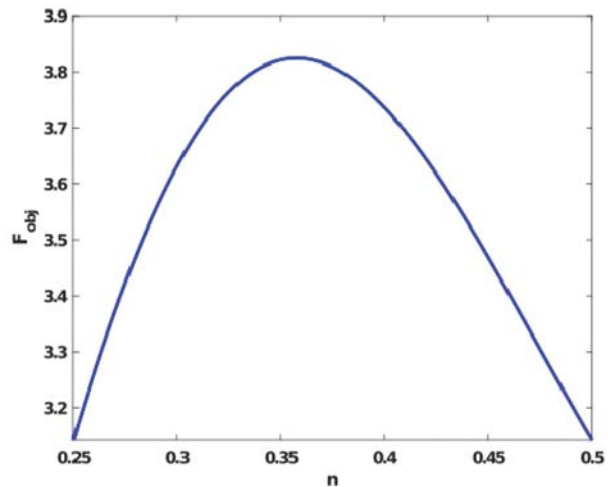


(a) Variation of $F_{obj}$ for n=0 to 10    (b) Variation of $F_{obj}$ for n=0.25 to 0.50

**Fig. 11.** Plot of $F_{obj}$ with *n*

Thereafter, considering the value of $\beta$ to be 1, and $F_{obj} = 0$, signifies that the fitness function, which is now equal to $\sigma_{obj}$, has to be minimized. Thus, in the same search space, the optimal value of *n* can be obtained following the same process as for the previous case. This yields the value of *n* to be 0.4156, at which the fitness function is equal to 0.3287. The same has been analytically validated from the following the current discussion on the validation of the developed optimization tool, the fitness function as defined by Eq. (21), has been maximized for a non-zero $\beta$. For instance, taking $\beta = 20$, the value of n was found to
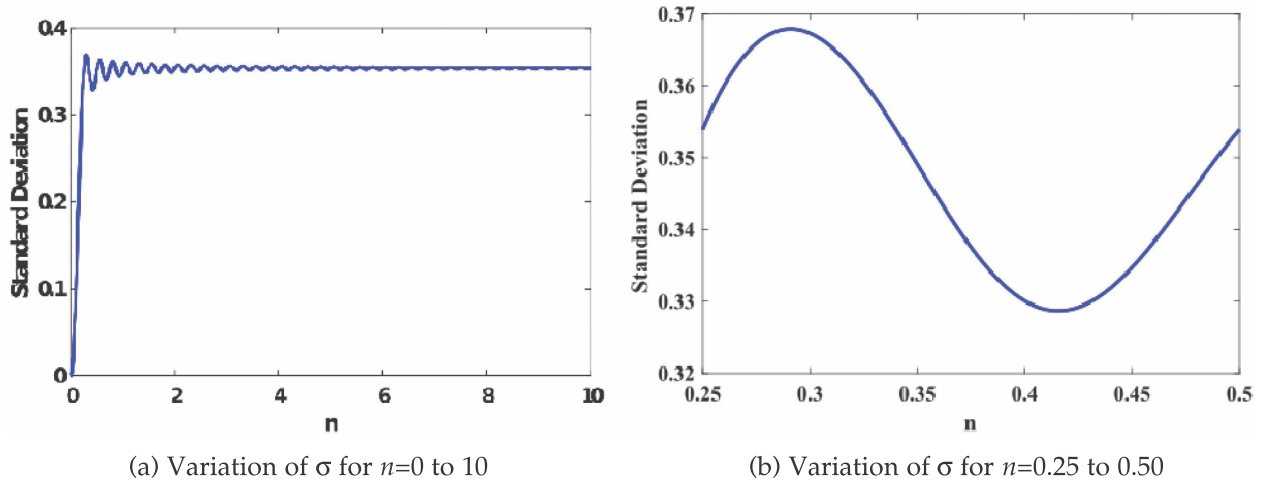
(a) Variation of σ for $n$=0 to 10



(b) Variation of σ for $n$=0.25 to 0.50
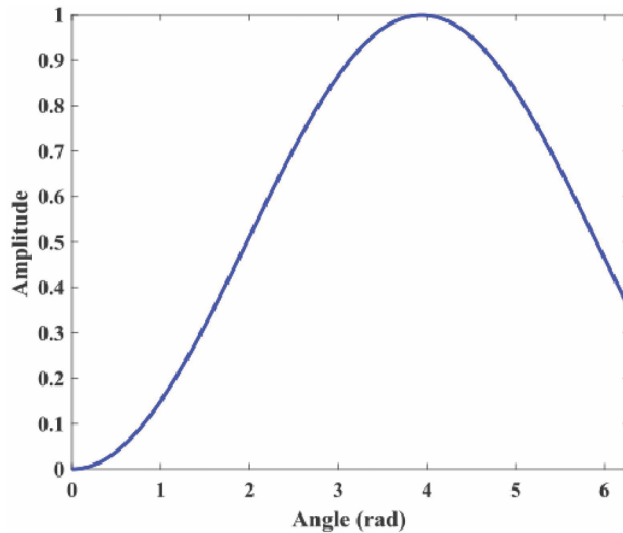
**Fig. 12.** Variation of σ with $n$



**Fig. 13.** Plot of $\sin^2(nx)$ with $n$=0.3986

be 0.3986 for which $F_{obj}$ and $\sigma_{obj}$ are found to be 3.7414 and 0.3303, respectively. The same can be obtained analytically as shown in Fig. 13 which thus provides a strong validation on the effectiveness of the developed optimization tool.

### 4.2 Test function-II

For the second level of validation, the $sinc(x)$ function, defined as Eq. (22) and shown in Fig. 14a, has been chosen as the test function. Following the similar approach that has been adopted for the first test function, a search space needs to be defined. Fig. 14b shows the variation of $F_{obj}$ and $\sigma_{obj}$ with $n$ for $n \in [0\ 1]$, and it can be observed that the $F_{obj}$ has a very high value in the vicinity of $n = 0$. However a significant variation in $F_{obj}$ and $\sigma_{obj}$ can be seen in the range $n \in [0.22\ 0.38]$ which therefore is taken to be the search space for the maximization of the fitness function.

$$\sin c(x) = \frac{\sin(n\pi x)}{n\pi x} \tag{22}$$

(a) Curve of sinc(x) for *n*= 1

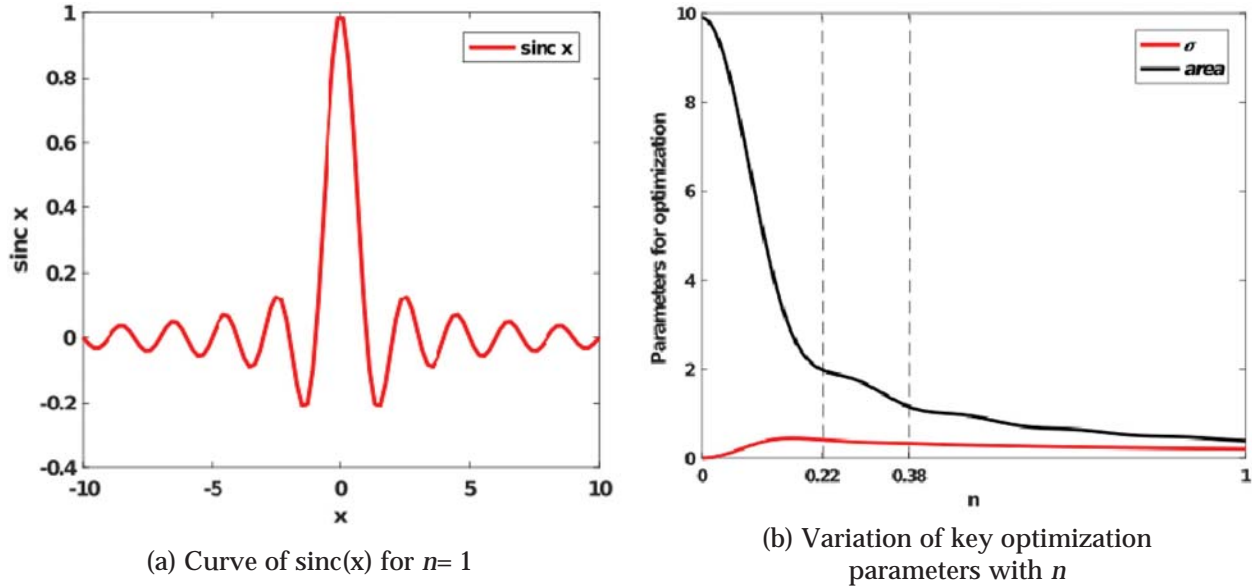(b) Variation of key optimization parameters with *n*

**Fig. 14.** Plots of sin*c* function

Thereafter, the optimization algorithm is applied, with $\beta = 10$, and the value of n was obtained to be 0.2660 at which the value of $F_{obj}$ and $\sigma_{obj}$ are obtained to be 3.866 and 0.3792 respectively, which can be analytically verified from Fig. 15a. The plot of sin*c(x)* for optimum n is shown in Fig. 15b.
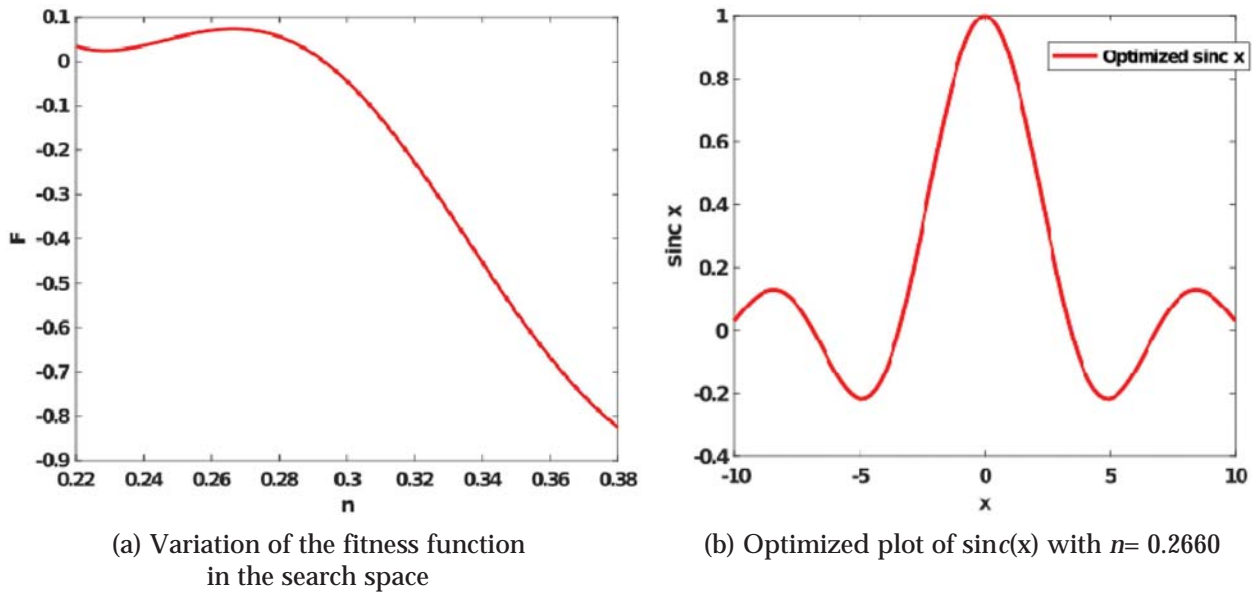


(a) Variation of the fitness function in the search space

(b) Optimized plot of sin*c*(x) with *n*= 0.2660

**Fig. 15.** Optimization of the fitness function for the test function-II

## 5. RESULTS AND DISCUSSION

In an earlier section, an analytical model has been developed for obtaining the key parameters that characterize the acoustic performance of the FGVM linings. In the present section, the study has been extended to different types of configurations where these linings are employed for various underwater applications. In order to validate the adequacy of this model in analysing the configurations under
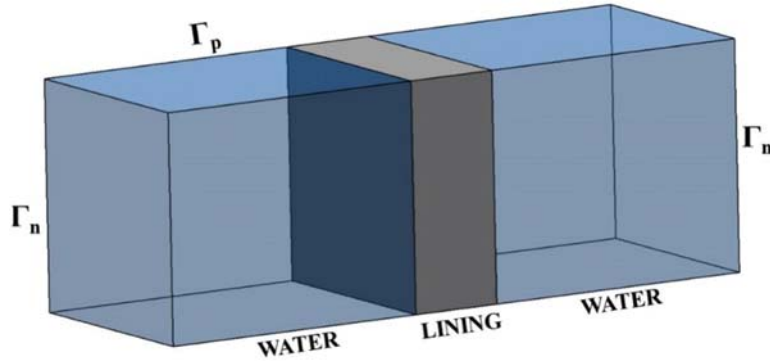
**Fig. 16.** Configuration of simple-FGVM Lining

consideration, finite element based numerical simulations have been carried out. Considering the simplest case of the lining, surrounded by water on both the sides, a 3-D model (as shown in Fig. 16), has been generated. To simulate the same, the acoustic waves are made to impinge on the lining from inside a semi-infinite water region. Perfectly matching layers (PMLs) have been imposed on the boundary surfaces ($\Gamma_n$ in Fig. 16), to avoid any reflection of the wave back into the model, and boundaries, denoted by $\Gamma_p$, have been assigned a periodic boundary condition.

In order to obtain efficient acoustic characteristics over the entire range of frequency, the parameters which have been used to define the variation of material properties are optimized. The fitness function as defined in Eq. (21) has been maximized over the frequency range of [100 Hz 20 kHz], to obtain the optimal parameters.

The material properties of the FGVM lining for the study are given in Table 1. As has been outlined in a previous section, the Poisson's ratio for the lining has been kept constant and has been assigned the value of 0.49 throughout the study.

In order to investigate the acoustic characteristics, a comparative study has been carried out on steel, viscoelastic layer and FGVM layer, for the same thickness, as shown in Fig. 17. For this analysis, the FGVM lining has been divided into n number of layers and each layer has been given different material properties as per Eq. (3). The frontal layer has been assigned the properties that of the viscoelastic layer while the back layer has been assigned the values of steel as given in Table 1.

This therefore assists in smooth propagation of the wave by gradually varying the impedance over the interfaces. Fig. 17a validates the analytical model by comparing it with the results from a corresponding 3-D FE analysis.

Fig. 17a shows the advantage of using a FGVM material as an acoustic lining. When steel alone is analysed, it has been observed that the *RC* remains at almost 100% for higher frequency ranges, while the effect of using only viscoelastic material lowers if down to about 70%. On the other hand, the proposed FGVM linings are found to have much lower *RC* of about 40% in the frequency bands of 9 kHz to 20

**Table 1.** Material parameters for single layer analysis.

| Properties | Steel | Water | Viscoelastic | FGVM | |
| --- | --- | --- | --- | --- | --- |
| | | | | Front Interface | Back Interface |
| $E$ (N/m$^2$) | $2.1 \times 10^{11}$ | – | $1.4 \times 10^8$ | $1.4 \times 10^8$ | $0.7 \times 10^8$ |
| $\rho$ (kg/m$^3$) | 7850 | 1000 | 1100 | 1100 | 2200 |
| $\delta$ | – | – | 0.23 | 0.23 | 0.345 |
| $c$ (m/s) | 6100 | 1500 | – | – | – |

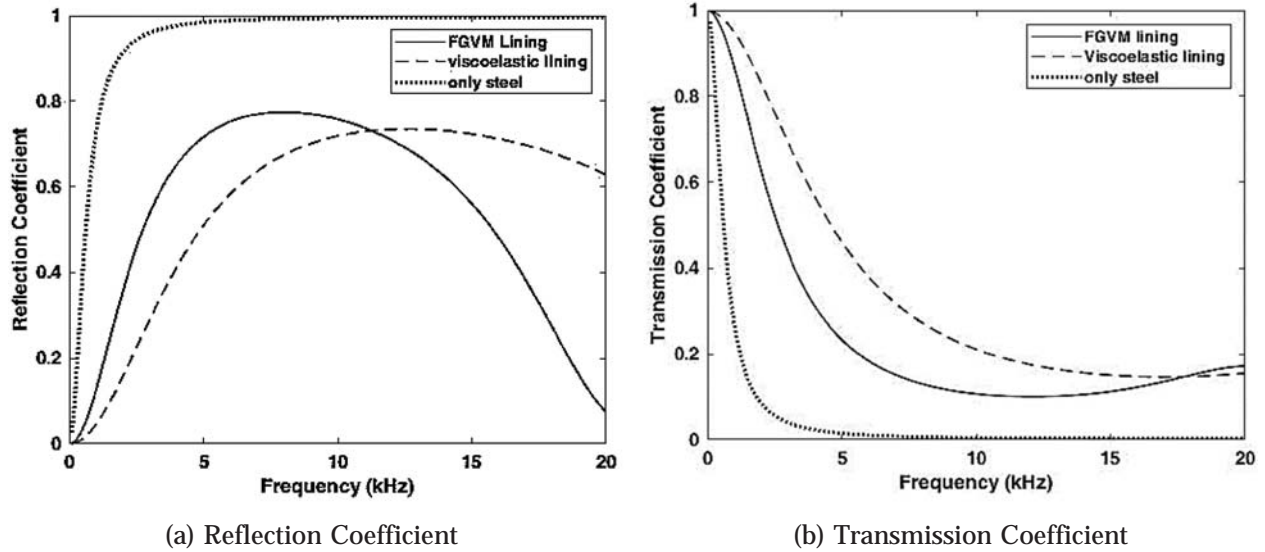(a) Reflection Coefficient  (b) Transmission Coefficient

**Fig. 17.** Underwater acoustic analysis of single layer of steel, viscoelastic and FGVM materials.

kHz. The index M for P-FGVM have been taken to be equal to 10, while the thickness of steel backing is 10mm. Out of all the three, the RC curve satisfies the criterion of the minimum fitness function as defined by Eq. (21) for the FGVM lining for a suitable value of the penalty parameter. It is vital to examine the effect of the proposed lining on the *TC* over its dominant frequency range. Fig. 17b outlines the *TC* for the three cases, and as expected steel layer shows a sharp fall in the frequency range below 2000Hz.

The analysis of simple FGVM has been done to project its potential utility as acoustic linings. But such a simple FGVMs cannot be utilized in such a configuration. It therefore becomes necessary to analyse the acoustic performance with a steel backing. The performance of such a single layer of coating is investigated and validated with the existing results[22]. Here the square unit cell of thickness 50 mm, backed by a 6 mm thick steel plate, has been considered. Fig. 18 shows the match between the two models.
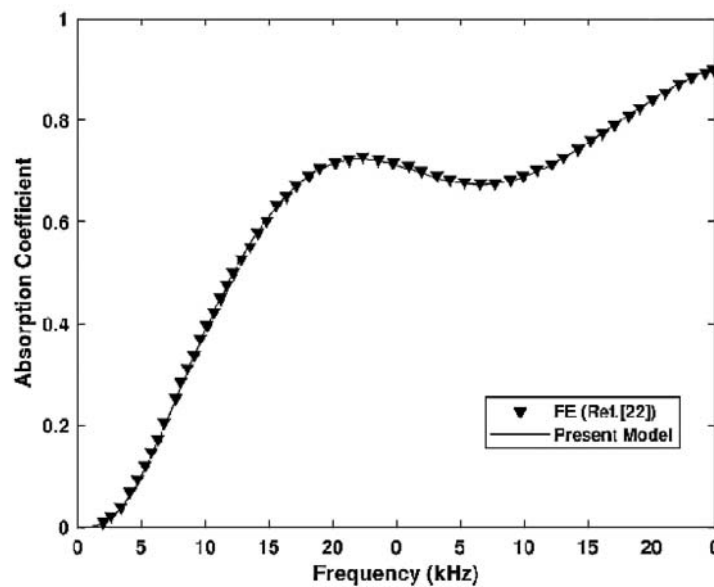


**Fig. 18.** Validation of the numerical model with steel

### 5.1 *Optimized configuration of the lining*

The previous section emphasized the utility of FGVM materials as acoustic linings for underwater applications and presented the validations of the developed analytical models. However, the present study is focused on cloaking steel plates of thicknesses of about 10mm, and therefore a configuration as shown in Fig. 19 is considered next.
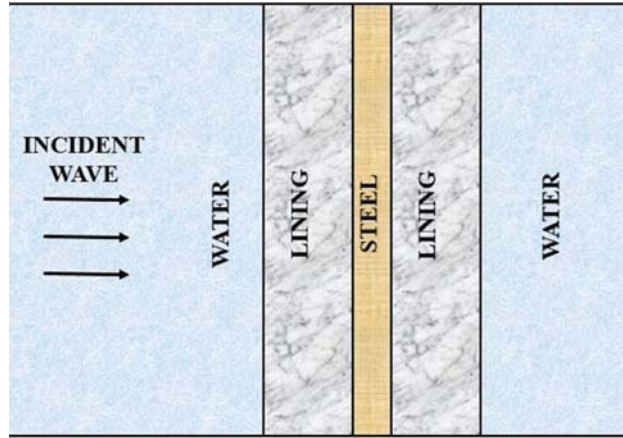


**Fig. 19.** Configuration of simple-FGVM Lining

The lining has been made to cover both the surfaces of the steel plate. This configuration offers an advantage by allowing to vary the geometrical aspects of the lining towards the back interface without affecting the drag which may develop due to such variations in the linings attached on the outer surface, Further, depending upon the underwater application of such a configuration, the layer beyond the lining and the backing may be considered to be filled with either water or air. For the analysis, the water on the left boundary is considered to be semi-infinite while the thickness of the lining has been taken as 100 mm while that of steel backing as 10 mm, respectively.

It has already been highlighted in a previous section that the material variation in the FGVM lining follows a power-law. For the current configuration, the outer and inner linings have been assigned different indices as $M_1$ and $M_2$, respectively. It is therefore vital for the study to investigate their effect on the
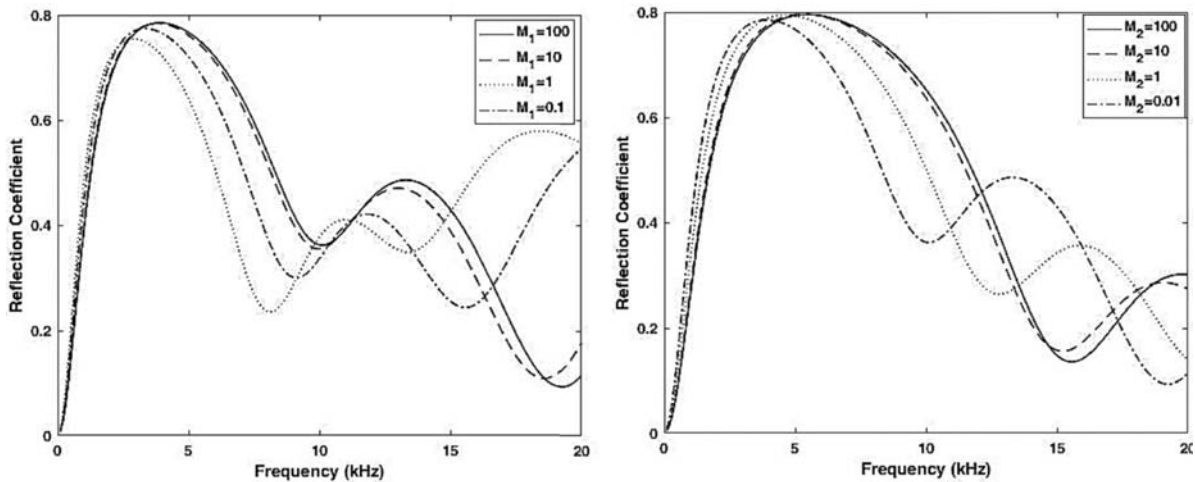


(a) RC with varying $M_1$, here, $M_2$=0.1      (b) RC with varying $M_2$, here, $M_1$=100

**Fig. 20.** Optimal selection of the grading index

performance of the lining. As can be observed from Fig. 20, while keeping $M_2$ constant, a better acoustic characteristics, as can be quantified from the fitness function, is obtained when $M_1 = 100$. Similarly when $M_1$ is kept constant, the optimal value of $M_1$ obtained is equal to 0.01. This means that for such a lining, the material property varies sharply at $z = h$ for the frontal layer and at $z = 0$ for the inner layer. This implies that the lining behaves as if having a viscoelastic layer with constant material properties for about 95% of the thickness. Therefore, it becomes important to analyse the effect of such a configuration where the thickness of viscoelastic layer, with properties same as that of frontal layer, is taken to be 95 mm while that of FGVM lining of 5 mm.

Fig. 21 shows the effect of employing such a configuration of materials as acoustic linings. In case, where the two different materials were used, the lining behaves the same as completely viscoelastic material with constant material properties neglecting the effect of the presence of the FGVM material. The FGVM linings, on the other hand, offer better acoustic characteristics as it satisfies the criterion set by the fitness function for the curve shown. Whilst, in its dominant range of frequency, *TC* falls more sharply for the FGVM lining (Fig. 21b).



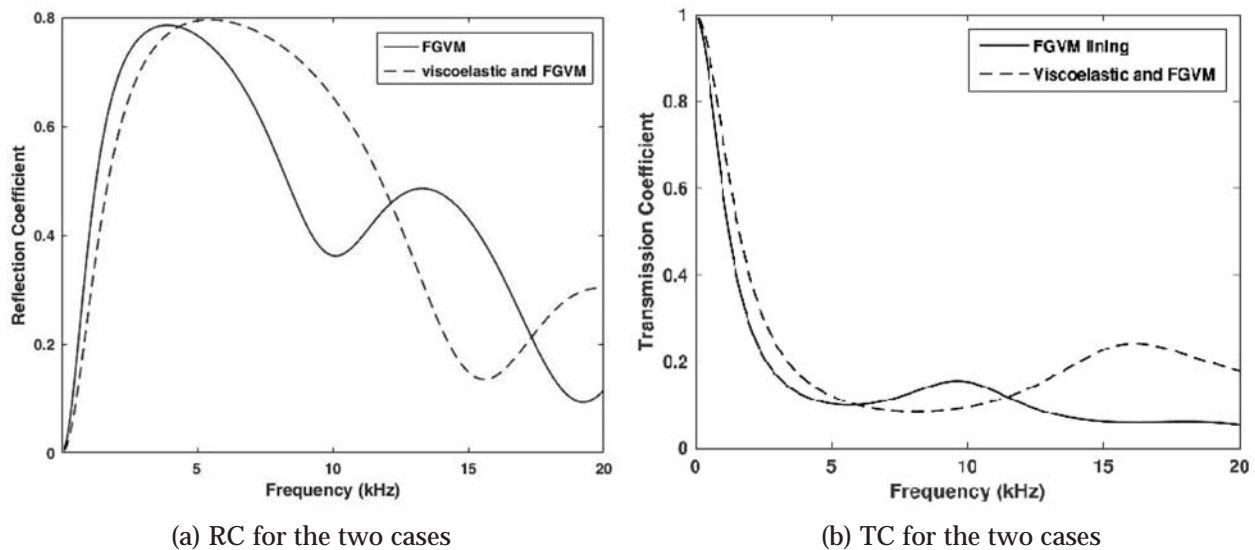(a) RC for the two cases          (b) TC for the two cases

**Fig. 21.** Comparison between using only FGVM and lining with 95 mm
viscoelastic material and 5mm FGVM

Now since the advantage of employing FGVM material for such an application has been laid, it becomes important to evaluate the performance for the properties at the back interface. It has already been mentioned that the FGVM material offers the flexibility to manipulate the material properties as per the requirement, and after the selection of the function defining the variation, the only variable left is the material properties at $z = h$ for frontal lining and at $z=0$ for back lining. As such, Fig. 22 shows the effect of the material properties defined at the back interface on the acoustic performance of the linings. As can be observed from Fig. 22a, *RC* below 40% is obtained in the frequency range of 14 kHz to 20 kHz for the cases when $E_2=10\,E_1$ and $E_2=E_{steel}$. On the other hand, *RC* falls below 40% at about 12 kHz in the case when $E_2=0.5\,E_1$, which also satisfies the criteria set by the fitness function.

The selection of the optimal parameters for the lining yielded in some exciting results in the mentioned frequency domain, and it has been observed that a steel backing of 10 mm can be suitably hidden. But the steel plate, intended to provide strength to the object, may have thicknesses suitable for its application. It therefore becomes important to investigate the effectiveness of the acoustic lining for varying thickness of the hull. As can be observed from Fig. 23, the proposed lining has the potential to camouflage steel of thickness up to 30 mm in the frequency range of 14 kHz to 20 kHz. The RC drops down below 40% for
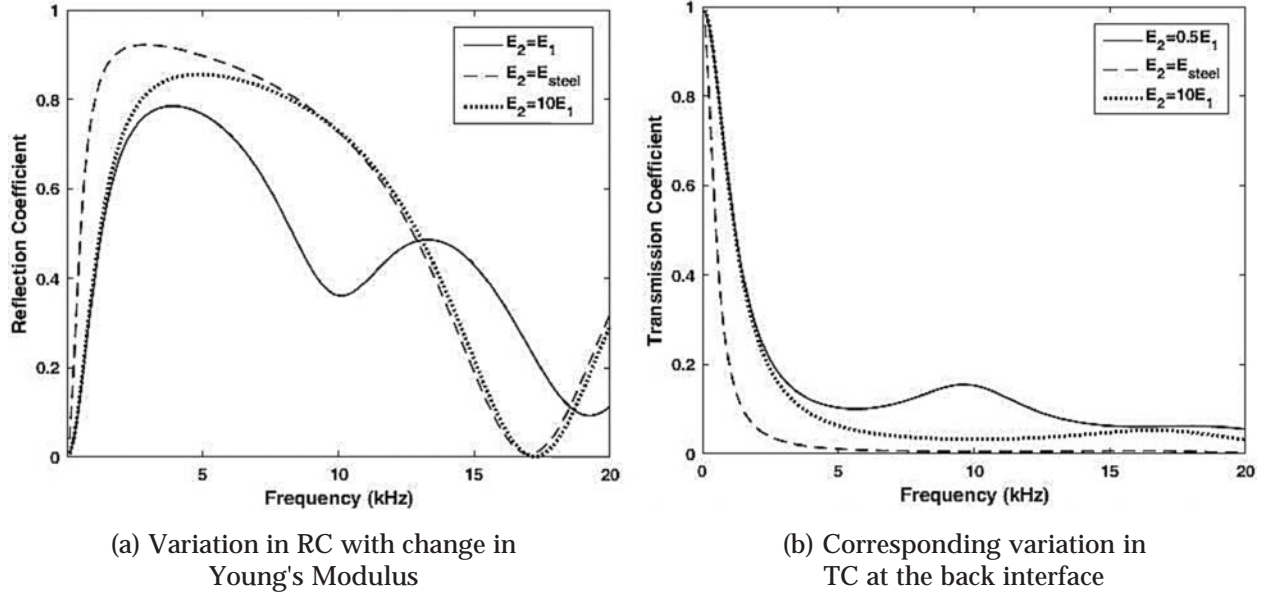
(a) Variation in RC with change in
Young's Modulus

(b) Corresponding variation in
TC at the back interface

**Fig. 22.** Selection of the optimal material properties at the back interface for the frontal layer



(a) RC for varying thickness of steel

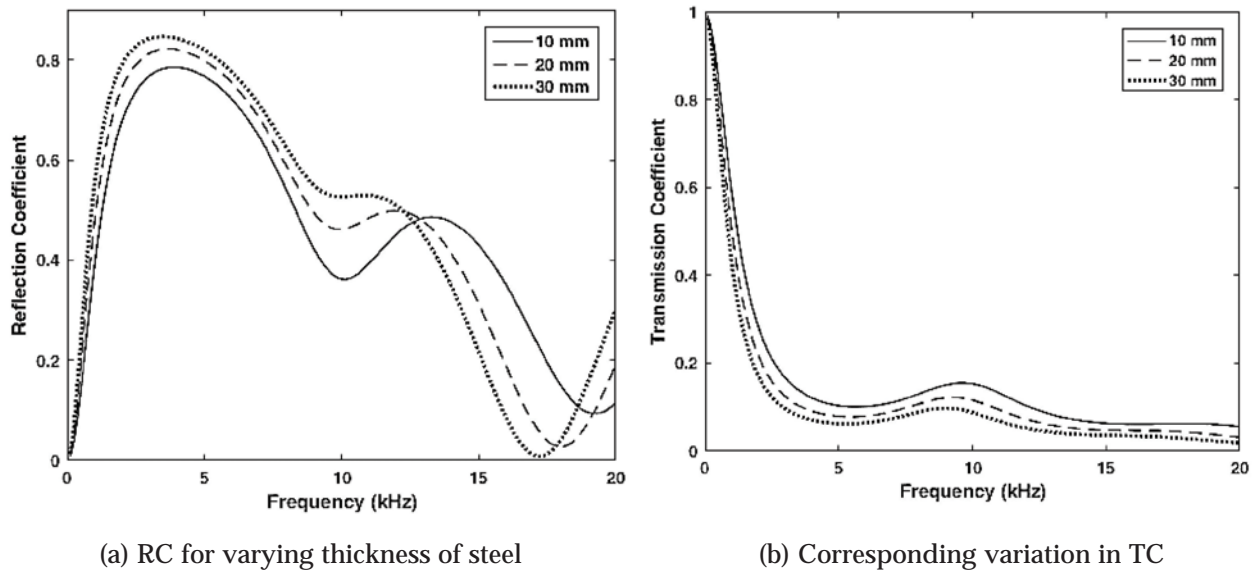(b) Corresponding variation in TC

**Fig. 23.** Variation in the acoustic characteristics with the variation in thickness of steel.

all the three cases in the frequency range of 12 kHz to 20 kHz. For the stealth of steel greater than 30 mm, the penalty parameter in the fitness function can be suitably varied as per the requirement to obtain a new set of optimal parameters.

Variation in thickness impacts the overall weight of the designated underwater object and therefore offers a constraint. As such, an analysis on the optimal value of the thicknesses of both the frontal layer and the back layer is necessary. It has been shown that two FGVM layers of 100 mm each can camouflage steel hulls of thickness upto 30 mm. Therefore, the variation is now made from 10 mm to 100 mm at both the layers. Fig. 24 shows the corresponding acoustic characteristics and it can be observed that *RC* increases to above 80% in the frequency range of 8 kHz to 20 kHz when the thickness of the lining is reduced to

(a) RC for varying thickness of linings     (b) Corresponding variation in TC
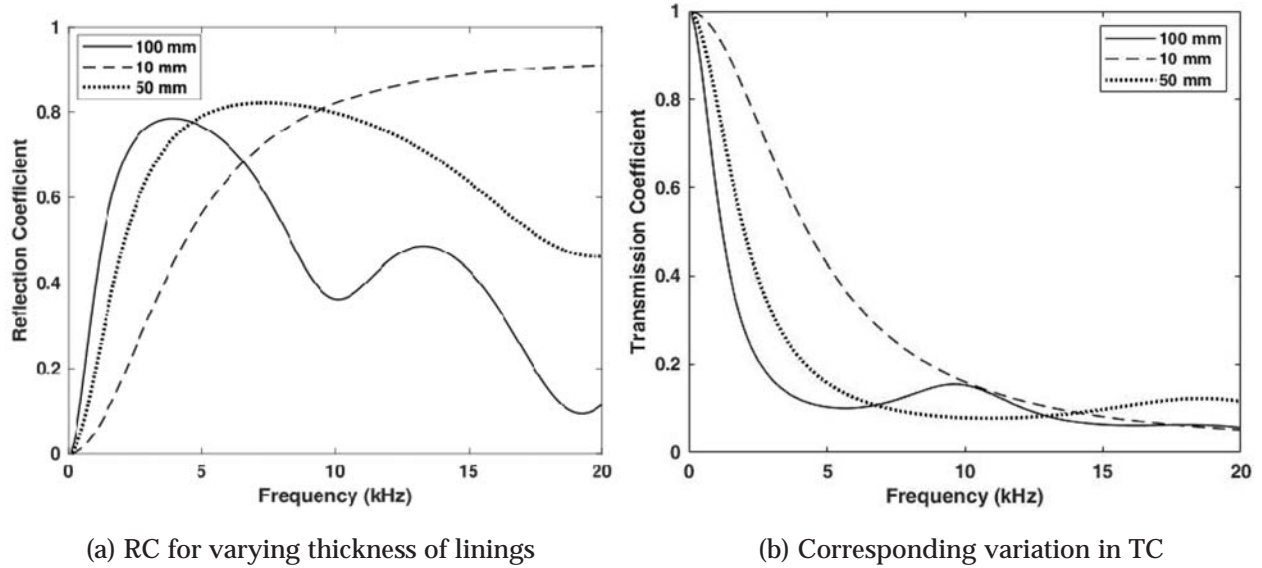
**Fig. 24.** Variation in the acoustic characteristics with the variation in thickness of the lining.

10mm. Similarly, the acoustic performance deteriorates even for $h$=50 mm. Therefore, the thickness which can offer a good performance is 100 mm.

It has already been mentioned that the layer beyond the linings can either be considered to be that of water or air. Therefore, to study the effect of the presence of air on the acoustic lining, an analysis has been carried out and presented in Fig. 25. As can be observed the *RC* starts from 1 and falls suddenly to below 40% at about 8 kHz. *TC*, on the other hand, becomes almost zero. This is because of the interface of the lining and air layer, at which air provides a drastic impedance mismatch. However, unlike the case with steel plates, there will be no phase shift in the incident wave. The major part of the energy which is getting reflected is being absorbed by the lining, as can be seen in Fig. 26 and therefore the performance remains somewhat unaffected in the frequency range of interest.
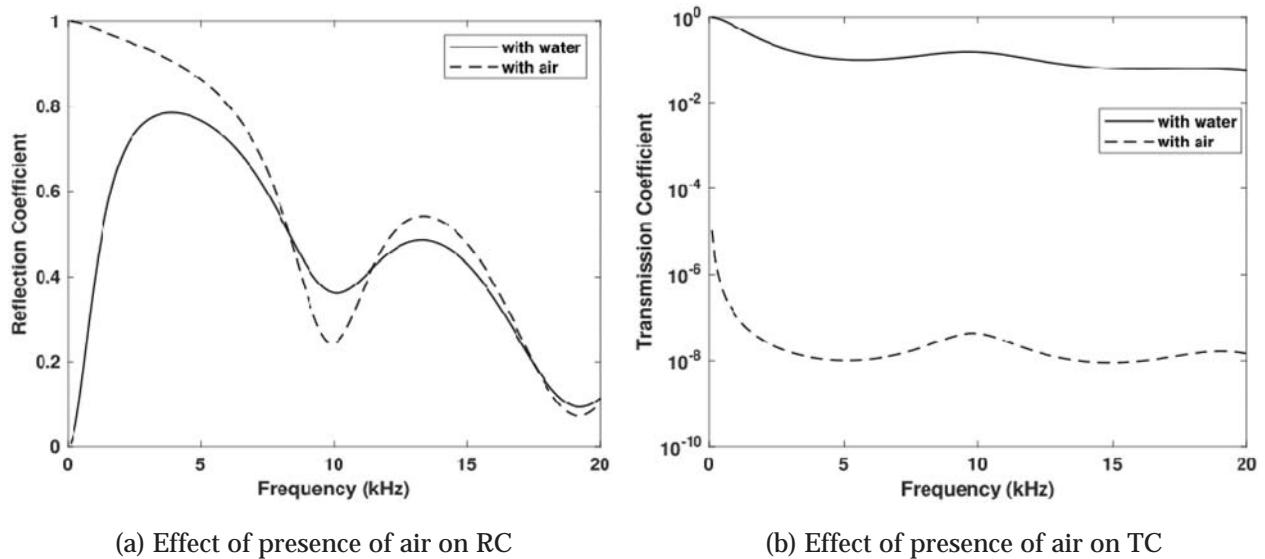


(a) Effect of presence of air on RC     (b) Effect of presence of air on TC

**Fig. 25.** Variation in the acoustic characteristics with air at the back interface
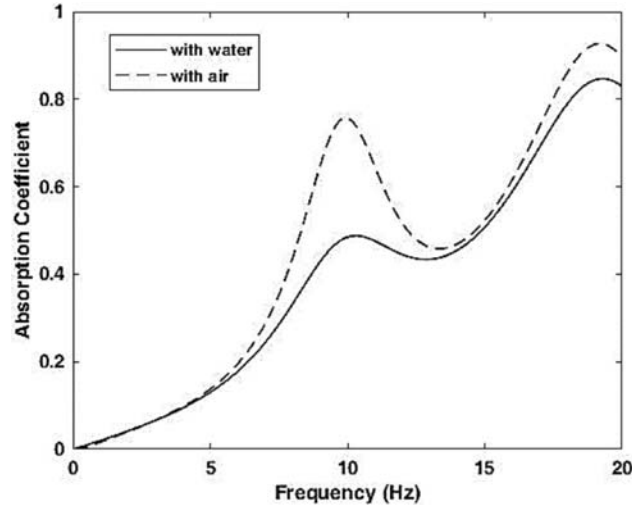
**Fig. 26.** Absorption Coefficient of the proposed linings in presence of air at the back interface.

## 6.  CONCLUSION

The present work has resulted in outlining the advantage of using FGVMs for designing underwater linings for various applications. In order to obtain a superior performance under the conflicting requirements of achieving desired *TC* and *RC* over a broad range of frequencies, both the geometrical and material parameters of P-FGVMs were suitably varied. An optimization algorithm coupled with *GA* and an objective function has been developed. Initially, the applicability and effectiveness of the said objective function has been demonstrated by applying it on some synthetic functions which share similar statistical characteristics with the *TC, RC* and *AC* curves generally encountered in present times. The process of optimization along with the chosen weight functions, when applied on acoustic linings generated encouraging results. It has also been presented by means of an optimized configuration, that the *RC* below 40% can be obtained for a frequency range of 12 kHz to 20 kHz. The study has further shown that the optimal selection of penalty parameter can yield results suitable for intended applications. All the results have been validated against computational methods using commercially available software.

## 7.  REFERENCES

[1]    G. Zhang and R. C. Batra, 2007. Wave propagation in functionally graded materials by modified smoothed particle hydrodynamics (msph) method, *Journal of Computational Physics,* **222**(1), 374-390.

[2]    S. Suresh, 2001. Graded materials for resistance to contact deformation and damage, *Science,* **292**(5526), 2447-2451.

[3]    S. Suresh and A. Mortensen, 1998. Fundamentals of functionally graded materials, *The Institute of Materials.*

[4]    Berezovski, J. Engelbrecht and G. A. Maugin, 2003. Numerical simulation of two-dimensional wave propagation in functionally graded materials, *European Journal of Mechanics-A/Solids,* **22**(2), 257-265.

[5]    S. Suresh, A. Giannakopoulos and J. Alcala, 1997. Spherical indentation of compositionally graded materials: theory and experiments, *Acta materialia,* **45**(4), 1307-1321.

[6]    D. Pender, N. Padture, A. Giannakopoulos and S. Suresh, 2001. Gradients inelastic modulus for improved contact-damage resistance. part i: The silicon nitride-oxynitride glass system, *Acta Materialia,* **49**(16), 3255-3262.

[7]    T. C. Chiu and F. Erdogan, 1999. One-dimensional wave propagation in a functionally graded elastic medium, *Journal of Sound and Vibration,* **222**(3), 453-487.

[8]     M. Moghaddam, M. T. Ahmadian and A. Kheradpisheh, 2013. Acoustic wave propagation through a functionally graded material plate with arbitrary material properties, *Proc. Inst. Mech. Eng. Part L J. Mater. Des. Appl.,* **227**(2), 100-110.

[9]     N. Chandra, S. Raja and K. V. Nagendra Gopal, 2014. Vibro-acoustic response and sound transmission loss analysis of functionally graded plates, *J. Sound Vib.,* **22**, 5786-5802.

[10]    M. Bednarik, M. Cervenka, J. P. Groby and P. Lotton, 2018. One-dimensional propagation of longitudinal elastic waves through functionally graded materials, *Int. J. Solids Struct.* **146**, 43-54.

[11]    C. Huang and S. Nutt, 2011. An analytical study of sound transmission through unbounded panels of functionally graded materials, *Journal of Sound and Vibration,* **330**(6), 1153-1165.

[12]    S. T. Christensen, S. Sorokin and N. Olhoff, 1998. On analysis and optimization in structural acoustics-part i: problem formulation and solution techniques, *Structural optimization,* **16**(2-3), 83-95.

[13]    J. Bos, 2006. Numerical optimization of the thickness distribution of three dimensional structures with respect to their structural acoustic properties, *Structural and Multidisciplinary Optimization,* **32**(1), 12-30.

[14]    J. Luo and H. C. Gea, 2003. Optimal stiffener design for interior sound reduction using a topology optimization based approach, *J. Vib. Acoust.,* **125**(3), 267-273.

[15]    J. Du and N. Olhoff, 2007. Minimization of sound radiation from vibrating bimaterial structures using topology optimization, *Structural and Multidisciplinary Optimization,* **33**(4-5), 305-321.

[16]    H. B. Yang, Y. Li, H. G. Zhao, J. H. Wen and X. S. Wen, Acoustic anechoic layers with singly periodic array of scatterers: Computational methods, absorption mechanisms, and optimal design, *Chinese Physics B* **23**(10).

[17]    T. Wang, S. Li and S. R. Nutt, 2009. Optimal design of acoustical sandwich panels with a genetic algorithm, *Applied Acoustics,* **70**(3), 416-425.

[18]    X. Zhang and Z. Kang, 2013. Topology optimization of damping layers for minimizing sound radiation of shell structures, *Journal of Sound and Vibration,* **332**(10), 2500-2519.

[19]    J. Li and S. Li, 2018. Topology optimization of anechoic coating for maximizing sound absorption, *Journal of Vibration and Control,* **24**(11), 2369-2385.

[20]    M. L. Munjal, 2014. Acoustics of ducts and mufflers, *John Wiley & Sons, Inc.,*

[21]    C. Ye, X. Liu, F. Xin and T. J. Lu, 2018. Influence of hole shape on sound absorption of underwater anechoic layers, *Journal of Sound and Vibration,* **426**, 54 - 74.

[22]    H. Meng, J. Wen, H. Zhao, L. Lv and X. Wen, 2012. Analysis of absorption performances of anechoic layers with steel plate backing, *J. Acoust. Soc. Am.,* **132**(1), 69-75.

# INFORMATION FOR AUTHORS

## ARTICLES
The Journal of Acoustical Society of India (JASI) is a refereed publication published quarterly by the Acoustical Society of India (ASI). JASI includes refereed articles, technical notes, letters-to-the-editor, book review and announcements of general interest to readers.

Articles may be theoretical or experimental in nature. But those which combine theoretical and experimental approaches to solve acoustics problems are particularly welcome. Technical notes, letters-to-the-editor and announcements may also be submitted. Articles must not have been published previously in other engineering or scientific journals. Articles in the following are particularly encouraged: applied acoustics, acoustical materials, active noise & vibration control, bioacoustics, communication acoustics including speech, computational acoustics, electro-acoustics and audio engineering, environmental acoustics, musical acoustics, non-linear acoustics, noise, physical acoustics, physiological and psychological acoustics, quieter technologies, room and building acoustics, structural acoustics and vibration, ultrasonics, underwater acoustics.

Authors whose articles are accepted for publication must transfer copyright of their articles to the ASI. This transfer involves publication only and does not in any way alter the author's traditional right regarding his/her articles.

## PREPARATION OF MANUSCRIPTS
All manuscripts are refereed by at least two referees and are reviewed by the Publication Committee (all editors) before acceptance. Manuscripts of articles and technical notes should be submitted for review electronically to the Chief Editor by e-mail or by express mail on a disc. JASI maintains a high standard in the reviewing process and only accept papers of high quality. On acceptance, revised articles of all authors should be submitted to the Chief Editor by e-mail or by express mail.

Text of the manuscript should be double-spaced on A4 size paper, subdivided by main headings-typed in upper and lower case flush centre, with one line of space above and below and sub-headings within a section-typed in upper and lower case understood, flush left, followed by a period. Sub-sub headings should be italic. Articles should be written so that readers in different fields of acoustics can understand them easily. Manuscripts are only published if not normally exceeding twenty double-spaced text pages. If figures and illustrations are included then normally they should be restricted to no more than twelve-fifteen.

The first page of manuscripts should include on separate lines, the title of article, the names, of authors, affiliations and mailing addresses of authors in upper and lowers case. Do not include the author's title, position or degrees. Give an adequate post office address including pin or other postal code and the name of the city. An abstract of not more than 200 words should be included with each article. References should be numbered consecutively throughout the article with the number appearing as a superscript at the end of the sentence unless such placement causes ambiguity. The references should be grouped together, double spaced at the end of the article on a separate page. Footnotes are discouraged. Abbreviations and special terms must be defined if used.

## EQUATIONS
Mathematical expressions should be typewritten as completely as possible. Equation should be numbered consecutively throughout the body of the article at the right hand margin in parentheses. Use letters and numbers for any equations in an appendix: Appendix A: (A1, (A2), etc. Equation numbers in the running text should be enclosed in parentheses, i.e., Eq. (1), Eqs. (1a) and (2a). Figures should be referred to as Fig. 1, Fig. 2, etc. Reference to table is in full: Table 1, Table 2, etc. Metric units should be used: the preferred from of metric unit is the System International (SI).

## REFERENCES
The order and style of information differs slightly between periodical and book references and between published and unpublished references, depending on the available publication entries. A few examples are shown below.

*Periodicals:*
[1]  S.R. Pride and M.W. Haartsen, 1996. Electroseismic wave properties, *J. Acoust. Soc. Am.*, **100** (3), 1301-1315.
[2]  S.-H. Kim and I. Lee, 1996. Aeroelastic analysis of a flexible airfoil with free play non-linearity, *J. Sound Vib.*, **193** (4), 823-846.

*Books:*
[1]  E.S. Skudzryk, 1968. *Simple and Comlex Vibratory Systems*, the Pennsylvania State University Press, London.
[2]  E.H. Dowell, 1975. *Aeroelasticity of plates and shells*, Nordhoff, Leyden.

*Others:*
[1]  J.N. Yang and A. Akbarpour, 1987. Technical Report NCEER-87-0007, Instantaneous Optimal Control Law For Tall Buildings Under Seismic Excitations.

## SUMISSIONS
All materials from authors should be submitted in electronic form to the JASI Chief Editor: B. Chakraborty, CSIR - National Institute of Oceanography, Dona Paula, Goa-403 004, Tel: +91.832.2450.318, Fax: +91.832.2450.602,(e-mail: bishwajit@nio.org) For the item to be published in a given issue of a journal, the manuscript must reach the Chief Editor at least twelve week before the publication date.

## SUMISSION OF ACCEPTED MANUSCRIPT
On acceptance, revised articles should be submitted in electronic form to the JASI Chief Editor (bishwajit@nio.org)